Dipl.-Ing. Nils Nöther

Distributed Fiber Sensors in River Embankments: Advancing and Implementing the Brillouin Optical Frequency Domain Analysis

BAM-Dissertationsreihe • Band 64
Berlin 2010

Die vorliegende Arbeit entstand an der BAM Bundesanstalt für Materialforschung und -prüfung.

Impressum

Distributed Fiber Sensors in River Embankments:
Advancing and Implementing the
Brillouin Optical Frequency Domain Analysis

2010

Herausgeber:
BAM Bundesanstalt für Materialforschung und -prüfung
Unter den Eichen 87
12205 Berlin
Telefon: +49 30 8104-0
Telefax: +49 30 8112029
E-Mail: info@bam.de
Internet: www.bam.de

Layout: BAM-Arbeitsgruppe Z.64

ISSN 1613-4249
ISBN 978-3-9813550-7-9

Distributed Fiber Sensors in River Embankments: Advancing and Implementing the Brillouin Optical Frequency Domain Analysis

vorgelegt von

Dipl.-Ing. Nils Nöther

aus Berlin

von der Fakultät IV – Elektrotechnik und Informatik
der Technischen Universität Berlin
zur Erlangung des akademischen Grades

Doktor der Ingenieurwissenschaften
– Dr.-Ing. –

genehmigte Dissertation

Promotionsausschuss:

Vorsitzender:	Prof. Dr. Roland Thewes
Gutachter:	Prof. Dr. Klaus Petermann
	Prof. Dr. Luc Thévenaz

Tag der wissenschaftlichen Aussprache: 30. April 2010

Berlin 2010

D 83

Wie eine Wilde Jagd trieben die Wolken am Himmel; unten lag die weite Marsch wie eine unerkennbare, von unruhigen Schatten erfüllte Wüste; von dem Wasser hinter dem Deiche, immer ungeheurer, kam ein dumpfes Tosen, als müsse es alles andere verschlingen. „Vorwärts, Schimmel!“ rief Hauke; „wir reiten unseren schlimmsten Ritt!“

– ***Theodor Storm***, *Der Schimmelreiter, 1888*

Digital ist besser.

– ***Tocotronic***, *1995*

Abstract

This thesis reports on the development of a system for distributed strain measurement in silica optical fibers. The system was developed to provide a solution for monitoring the structural health of river embankments with a measurement length > 5 km and a spatial resolution < 5 m. It is based on stimulated Brillouin scattering (SBS), a nonlinear optical effect which converts the mechanical strain of an optical fiber into a frequency shift of the backscattered light of an optical signal. The measurement technique that is employed and significantly advanced within this work is the Brillouin optical frequency domain analysis (BOFDA). Prior to this work, this technique had been presented as a laboratory setup providing its proof of concept; however, at this development stage, the technique had been limited in performance, theoretical foundation, integrability and robustness for real-life applications when compared to the state-of-the-art Brillouin optical time domain analysis (BOTDA).

The thesis comprises the theoretical background of the measurement system, advancements regarding its implementation into a practically applicable device – including the proposal of techniques for performance enhancements in signal processing – as well as the evaluation of the system performance in experimental studies.

First, the physical nature of SBS in optical fibers is analyzed. Here, special focus is set on the frequency domain properties of the interaction between the optical signals, which provides a deep understanding of the system behavior in the special case of distributed measurements in the frequency domain. The BOFDA technique is then presented with a thorough analysis from a system point of view and considerations on its implementation in a practical setup.

The laboratory setup is presented with all components and different aspects of advancement in accuracy and efficiency over the state of development prior to this work, along with representative measurement results. As the major advancement regarding the system implementation, a digital approach to frequency domain measurements is presented, with a system description, a demonstrator setup and measurement results.

A detailed analysis of the physical occurrences within the system that lead to a limitation of its spatial resolution is given, founding on the description of SBS earlier in the thesis. It comprises a novel point of view on the measurement artifacts that degrade frequency domain measurements of SBS; a connection to corresponding studies that apply to the BOTDA technique is made. From here, a novel approach to overcome the limitations by means of signal correction in post-processing is presented.

Finally, the application of the measurement system in dike monitoring is presented. A method for integrating optical fibers into geotextiles is introduced, together with considerations on the coating material and handling on construction sites. By presenting several experimental tests in the laboratory and the field, the feasibility of the system for monitoring of the structural health of river embankments is confirmed.

With the advancements achieved within this work, the BOFDA technique meets the specifications in accuracy and resolution of state-of-the-art BOTDA devices, while offering new perspectives in terms of dynamic range, robustness and cost efficiency.

Zusammenfassung

Diese Arbeit beschreibt die Entwicklung eines Systems zur verteilten Dehnungsmessung in optischen Glasfasern. Das System wurde zur Überwachung der strukturellen Integrität von Flussdeichen bei einer Messlänge von mindestens 5 km und einer Ortsauflösung von höchstens 5 m entwickelt. Grundlage des Messsystems ist der nichtlineare optische Effekt der stimulierten Brillouinstreuung (SBS), der die Dehnung einer optischen Glasfaser in eine messbare Frequenzverschiebung des Rückstreulichts eines optischen Signals überträgt. Die in dieser Arbeit angewendete und grundlegend weiterentwickelte Messtechnik ist die optische Brillouin-Frequenzbereichsanalyse (BOFDA). Die grundsätzliche Funktionalität dieser Technik war bereits vor Beginn der Untersuchungen zu dieser Arbeit gezeigt worden. Allerdings war ihre Entwicklung der Brillouin-Zeitbereichsanalyse (BOTDA), die den Stand der Technik darstellt, in Bezug auf ihre Sensoreigenschaften, ihre theoretischen Grundlagen, ihre Integrierbarkeit und ihre Robustheit für praktische Anwendungen weit unterlegen.

Die Arbeit umfasst den theoretischen Hintergrund des Messsystems, verschiedene Weiterentwicklungen der Implementierung in ein anwendungsorientiertes Messgerät (u.a. neue Konzepte für Signalkorrekturverfahren zur Verbesserung der Sensoreigenschaften) und die Evaluierung des Systems in experimentellen Untersuchungen.

Zu Beginn werden die physikalischen Eigenschaften der SBS in optischen Fasern untersucht und die Differentialgleichungen, mit denen der Effekt beschrieben werden kann, hergeleitet. Die Analyse konzentriert sich auf die spektralen Eigenschaften der Brillouin-Wechselwirkung, um die Messung der SBS im Frequenzbereich genau beschreiben zu können. Die BOFDA-Methode wird mit einer Systembeschreibung und Betrachtungen zur praktischen Umsetzung im Labor vorgestellt.

Der Laboraufbau wird im Detail beschrieben; die Beschreibung umfasst die Komponenten, verschiedene Aspekte der Weiterentwicklung gegenüber dem Entwicklungsstand vor Beginn der Arbeiten sowie repräsentative Messergebnisse. Als wichtigster Fortschritt auf dem Weg zur kompletten Implementierung des Systems wird ein digitales Verfahren zur Frequenzbereichsanalyse (mit einer Systembeschreibung, einem Demonstratoraufbau und Messergebnissen) vorgestellt.

Auf Grundlage der erarbeiteten Analyse der SBS wird die physikalisch bedingte Begrenzung der Ortsauflösung des Systems untersucht. Das Ergebnis ist eine neue Interpretation von Artefakten in hochauflösenden Messungen, von der aus eine Parallele zu ähnlichen Untersuchungen bezüglich der BOTDA-Methode aufgezeigt wird.

Schließlich wird die Anwendung des Messsystems im Deichmonitoring vorgestellt. Hierzu wurde eine Technik zur Integration faseroptischer Kabel in Geotextilien sowie ein optisches Sensorkabel entwickelt. In Labor- und Feldversuchen wird die Eignung des Systems für das Deichmonitoring bestätigt.

Durch die Weiterentwicklung des BOFDA-Verfahrens hat das Verfahren nicht nur in Genauigkeit und Auflösung zum BOTDA-Verfahren aufgeschlossen, sondern eröffnet neue Perspektiven in Dynamik, Robustheit und Kosteneffizienz.

Acknowledgments

What relevance might have fiber optics to the safety of river dikes? Well, it has taken four years to scrutinize this remarkable interrelation. Here is the result: This thesis – and the insight, that its mixture of fiber optics, digital and RF electronics and the ever-present real-life application has initiated some passion in me. And then there's this physical effect that (even after completing chapter 2.1) I would call insane to a certain extent: A 13 GHz acoustic wave, optically excited and thus responsible for the backscattering of light? Still amazing enough to continue research…

How did it all start? Research was initiated in 2005 by BAM and TU Berlin. For this framework as well as for providing me with excellent supervision throughout my work, first of all I would like to thank Dr. Katerina Krebber – she herself being one of the pioneers of the BOFDA system – and Prof. Dr. Klaus Petermann, my supervisor at TU Berlin. For the great working conditions at BAM, I owe my thanks to Dr. Werner Daum, head of the division „Measurement and Testing Technologies; Sensors“ and Dr. Wolfgang Habel, head of the working group „Fibre Optic Sensors“.

For valuable feedback throughout the final investigations and for kindly examining my work and being part of the committee at my defense, I would like to thank Prof. Dr. Luc Thevenaz from EPFL Lausanne.

All in all, I could not imagine a more pleasant and productive environment for research than the working group „Polymer and Distributed Optical Fibre Sensors“. I would like to thank Aleksander Wosniok for the cooperation throughout our research. For the most valuable discussions on nonlinear optics and signal processing, I owe a big part of my thanks to Philipp Lenke; I can't possibly imagine this thesis without his ever-present advice. Together with Sascha Liehr, Mario Wendt, Marcus Schukar and Dr. Jens Witt, they form a great team, and each of them has contributed to this work in some way or the other, therefore I would like to thank them all.

Another example of outstanding team play: Our research project. I'd like to thank our partners: Rainer Glötzl from Glötzl GmbH for his encouraging mixture of experience and visions, Elke Thiele for great collaboration with no fear of interdisciplinarity – and all team members from BBG, Franzius Institute and Fiberware.

In November 2007, the COST 299 programme allowed me to spend a week at the Second University of Naples with Prof. Dr. Luigi Zeni, Dr. Aldo Minardo and Dr. Romeo Bernini. I would like to thank the three of them for this great opportunity of co-operation and exchange of experiences; this week had indeed some valuable impact on my understanding regarding the theoretical aspects of Brillouin sensing.

Even before Brillouin sensing started to impact their very own future, Marko Krcmar and Dr. Stefan von der Mark provided indispensable support for me and my work. In 2008, the idea of taking the exploitation of the technology into our own hands came upon. For their dedication and enthusiasm with which they joined me to bring the idea towards realization, I owe them my very special thanks.

And for all patience, for all sympathy I'd like to thank Katharina. No thesis was ever written without messing about private and social life, mine being no exception. There was some challenge within the last months, and I'm glad I was not alone.

Contents

CHAPTER 1

Introduction

Dikes – man-made systems of flood defense – stretch over hundreds and thousands of kilometers along riversides and shorelines, designed with expertise gathered over centuries of construction. Most people – whether they are experts in flood defense or not (and the second group explicitly includes the author of this thesis) – consider these embankments as the essential protection from the forces of water, from storm surges and river floods, as respectable structures that were built to keep the vulnerability of human settlements within manageable limits, and even as an indispensable element of the natural scenery along rivers and coasts.

Although monitoring the structural integrity of river dikes is but one of many applications for fiber optic sensing, it was the task by which the author of this thesis became aware of the relevance of fiber optics to geotechnical and civil engineering.

Now, after three years of research, a sensing system for distributed monitoring of the structural integrity of river dikes, based on optical fibers integrated into geosynthetics, is presented. The achievement of the results that are summarized in this thesis go back to the initiation of a dialog between experts from the fields of geotechnics and hydrology, fiber optic sensing and structural health monitoring, and development and application of technical textiles. The Federal Institute for Materials Research and Testing (BAM) with its working groups „Fiber-optic sensors“ and „Distributed and polymer-optical fiber sensors“ contributed to this synergy by providing three years of research within its in-house doctoral program, the framework in which this thesis was written. The investigations were carried out within the program „Risk Management of Extreme Flood Events (RIMAX)“ of the Federal Ministry of Education and Research. Cooperating partners in the project were the Saxon Textile Research Institute (STFI), Glötzl Gesellschaft für Baumesstechnik mbH, Franzius-Institut für

Wasserbau und Küsteningenieurwesen of the University of Hannover and Bauberatung Geokunststoffe GmbH.

With the jointly formulated goal of the project, tasks were shared, accounting for the distributed competences of the partners. Consequently, this thesis is focused on the author's tasks within the larger framework, being the investigations assigned to BAM: the theoretical background and the technical aspects of a measurement unit for distributed sensing of strain in optical fibers. However, it was the resonance from the experts in dike construction and flood defense which provided the motivation to bring the concept of the Brillouin frequency domain analysis from the laboratory test bench out into the world of structural health monitoring. The requirements on a system that would perform a reliable monitoring of the integrity of a dike – although they were expressed in terms quite different from those of fiber optics and electronics – provided exact goals and guidelines during research and development. Moreover, by bringing the laboratory setup to real-life construction sites in order to perform measurements on sensors buried into the soil, constant feed-back about the feasibility of the whole concept was available.

In a sense, contact to the real-world application of the concept was never lost. The following sections will deal with the matter of monitoring river dikes, giving the original motivation for the initiation of the project and illustrating the value of a distributed fiber optic sensor system.

1.1 Distributed sensing in flood protection

As a consequence of the recent floods in Central Europe in 1997 and 2002, a large part of the existing defense systems – among them being earth structures such as dikes and dams – had to be rebuilt or reinforced, using state-of-the-art knowledge. Modern river dikes are a well-considered composition of materials with different geotechnical and hydraulic properties, forming three zones inside the soil body. Figure 1.1 shows the basic structure of such a modern river dike [1]. The placement of a sealing layer at the water side dike slope and a drainage mass of high permeability at the land side dike foot force the seepage line to decrease its level towards the land side of the dike.

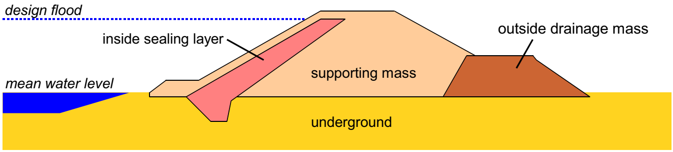

Figure 1.1: Cross-section of a modern river dike showing the three zones of the soil body.

In these state-of-the-art construction techniques, several forms of geosynthetics play an important role. Mostly geotextiles (such as woven or non-woven fleece mats) and grid structures are integrated into the soil as reinforcement materials, protection from erosion and settlement, drainage elements to control the seepage line or filters for separation of the different soil layers.

However, in the case of an extreme flood, even modern dikes might lose their integrity due to various geophysical mechanisms, as illustrated in figure 1.2. While for coastal dikes, erosion on the seaside due to wave impact is the most common cause of dike failure, river dikes are primarily endangered by erosion of the land side slope as well as piping and gliding of the whole soil body due to long-lasting high water level [2].

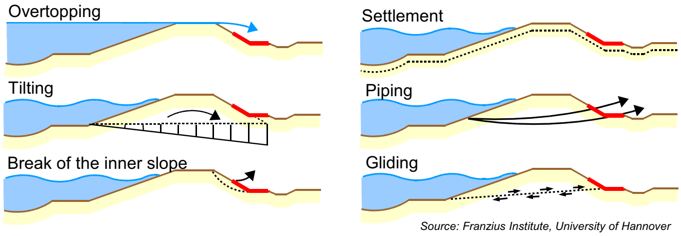

Source: Franzius Institute, University of Hannover

Figure 1.2: A selection of typical failure mechanisms for river dikes. Sensors for early detection of these mechanisms should be placed in an area at the land side dike foot (indicated by the red line).

In case of an extreme flood event, it has proven to be very difficult to perform an analysis of the condition of the dike body and to predict the time and location of an imminent failure. Historically, the only feasible analysis of the integrity of a dike has been an inspection of the surface, performed by dike-runners that walk along the endangered dike sections, often at a considerable personal risk. A section where overflooding occurs might lead to erosion of the land side slope within half an hour and is therefore barely discovered in time. Structural damages inside the dike body, caused by piping, settlement or animal activities, will only become visible when the consequences of integrity loss occur and dike failure is inevitable.

More analytical approaches, such as numerical simulations of geotechnical and hydraulic mechanisms, have given more reliable information about failure mechanisms during extreme flood events [3]. Still, such techniques will always lack accuracy due to insufficient data input. In spite of the well-defined structure of modern dikes, in reality the composition of the materials is hardly homogeneous and strongly depends on the local availability of the materials. Also, the long-term development, including settlement, influences of the climate and animal activities can not be included into numerical models. In order to gain more hydraulic information, a method for point-wise measurement of the seepage line has been proposed [4]. This technique uses vertically orientated electrical pulse reflectometry and can only be performed in-situ at a very limited number of test points and does not allow real-time monitoring of large dike sections.

In order to see into that highly vulnerable black box which is the soil body of the dike, techniques of monitoring and sensing for structural health monitoring are needed. The necessity of a wide-range alarm system to detect displacement of the soil that might weaken the dike and lead to streams of water, settlement, cracks and finally to breaches, becomes evident. With a sensing system that is able to detect the exact place of critical geotechnical incidents and then delivers the information to a central control station, valuable time could be gained to take actions like reinforcing the dike using sand bags or initiating evacuation. Such a system would have to perform reliable long-term measurements of the geotechnical activities over a length of several kilometers, being able not only to localize critical displacement, but also to estimate the dimension and damage potential of such a weak spot.

1.2 Fiber optic sensing techniques

Among the numerous established sensing techniques that are based on optical fibers, distributed Brillouin sensing has been found to best suit the needs of dike monitoring and is therefore the central focus of this work. In order to explain this decision, this section gives a brief overview over the various fiber optic sensing techniques that are involved in structural health monitoring, which are then examined with respect to the application's demand of detecting critical soil displacement in large geotechnical structures. In the following section, distributed Brillouin sensing is introduced as the best suited solution for the application lined out in section 1.1.

Apart from their large usage in telecommunications, optical fibers have found many applications in structural health monitoring, where they provide a number of optical phenomena that can be exploited for sensing purposes. In fiber optic sensing, at some point in the system the quantity that is to be measured is transferred into an optical signal. There are numerous quantities that have a measurable impact on the propagation of light, among them being chemical quantities (e.g. pH of liquids and gas concentration within a free-space transmission), mechanical quantities (e.g. strain, acceleration and pore pressure impacting on a waveguide transmission) and other physical quantities such as temperature and even nuclear radiation.

For many of these measurands, sensing techniques have been available long before the establishment of fiber optic sensors. For instance, mechanical deformation is classically measured by means of resistance strain gauges, and there are various methods for bringing temperature probes into a monitoring structure. However, apart from the individual advantages that the different fiber optic sensing techniques offer, there are some features that are common to most of them. Their insensitivity to electromagnetic fields makes them robust to lightning puncture and allows applications in high-voltage facilities and medical environments. Their chemical and mechanical ruggedness opens many applications in harsh environment; their small size (the diameter of the coated fibers lies in the range of 1 mm) allows easy integration into the structures even at places difficult to access.

In order to categorize the existing concepts of fiber optic sensing, several approaches are feasible:

- By the sensor's material: **Silica optical fibers** as well as **polymer optical fibers** can be used for sensing purposes. The optical, mechanical and chemical properties of these different materials determine the physical quantities that can be measured and the application fields.
- By arrangement: Many techniques of transferring the measurands into an optical signal are performed within a discrete device, allowing **point-wise measurements** of the quantity. Such punctual sensors can be fed into the structure as a probe, providing a sample of information that has to be extrapolated in order to gain information over a larger spatial range. Some point-wise sensors can be arranged in chains or arrays, allowing a **quasi-distributed measurement** of the structure. In contrast, **distributed sensors** provide a (practically) continuous signal in at least one spatial dimension. In fiber optic sensing, this means that all along the fiber length an interaction between the measurand and the optical signal must occur. The output signal of the sensor must contain the spatial information to allow reassignment of the measured quantity to the location of the occurrence.
- By optical parameter: Depending on the nature of the interaction between the measurand and the optical signal, different properties of the light will be affected and will contain the information about the measurand. In **interferometric sensors**, the phase of the optical signal is altered, leading to characteristic interference patterns after superposition with a reference signal; in systems using **pulse reflectometry**, the time of flight (time elapsing between the launching of an optical pulse into the fiber and the arrival of the light at a detector that has been reflected or backscattered at a certain point along the measuring length) is used; in **spectrometric sensors** as well as sensors using **non-linear optical effects**, the characteristic wavelength spectrum of the optical signal is recorded and analyzed. Since distributed Brillouin sensing bases on a non-linear optical effect and uses pulse reflectometry in order to acquire the desired information, these two concepts will be illuminated much deeper in the following sections.

Among the large number of fiber optic sensing techniques, a few that have become most relevant for applications in structural health monitoring are listed below.

- For point-wise dynamic deformation monitoring, fiber optic **extrinsic Fabry-Perot interferometers (EFPI)** have been integrated into concrete piles [5]. In this technique, two silica optical fibers are placed into a capillary in such a way that their end faces form a cavity of a few micrometers. Injected light is partially reflected at the two surfaces and superposed inside the fibers. The characteristic interference pattern depends on the phase difference of the two superposed optical signals and thereby contains information about the deformation of the capillary.

- **Fiber Bragg gratings (FBG)** are interference filters that are inscribed into silica (and, recently, polymer) optical fibers. An optical signal is injected into the fiber and fed through the grating. According to the Bragg relation, characteristic parts of the optical spectrum will be reflected at the grating. Since this spectral response depends on the grating period, it will change with temperature and strain applied to the optical fiber in longitudinal direction at the position of the grating. FBGs play an increasing role in structural health monitoring, for example in wind turbine blades [6], bridges and dams. By aligning several gratings along one optical fiber, a quasi-distributed deformation or temperature sensor over a length of several hundred meters can be realized.

- **Distributed Raman sensing** in silica optical fibers uses a non-linear optical effect known as stimulated Raman backscattering for distributed measurement of temperature. While being entirely insensitive to mechanical stress, distributed Raman sensors allow temperature monitoring over lengths of several kilometers and are used for fire detection in tunnels [7] or leakage detection along pipelines.

- In recent years, **polymer optical fibers (POF)** have become very important in short-range communication applications. Their main advantages over silica fibers are their robustness to mechanical stress and an easy handling during the installation process, which makes them highly attractive for sensing applications. While the commercial availability of FBGs inscribed into POF is still delayed due to significant technical difficulties, a new approach of distributed strain sensing has proven to be very promising. Since in polymer fibers applied strain leads to a roughly linear increase of the intensity of Rayleigh backscattering, pulse reflectometry can be used to perform a distributed measurement of the strain profile of the fibers [8]. The feasibility of this method for monitoring of geotechnical and masonry structures has been shown [9]. Due to the high optical losses of polymer fibers, the measurement range of such a distributed sensor is limited to a few hundred meters.

Now, in order to solve the task of monitoring the structural integrity of river embankments, the existing sensing methods have to be examined with respect to the requirements of the application. It has been outlined in section 1.1, that the physical quantity to be measured in dike monitoring is deformation and displacement of soil. Naturally, this has to be done indirectly: The fiber optic senors for mechanical quantities that have been described above are sensitive to stress in one dimension, e.g. the physical measurand of such a sensor is the longitudinal strain of the fiber. Integration techniques of the optical fibers into the soil that provide a reliable transfer of the soil displacement into fiber strain will be discussed in later sections.

Quasi-distributed strain measurements, allowing conclusions about geomechanical activities in the soil body of dams, have been performed using FBGs [10]. Since the measurement range of this technique is limited to a few hundred meters, it is not feasible for monitoring tasks at larger sections of river dikes, where lengths of several kilometers are a stated requirement. Moreover, such a distributed array of point-wise sensors can not be uniquely related to a continuous strain profile [11].

Distributed POF sensing overcomes the problem of discrete measurement points; in this technique, an absolute relation of the measurement trace to the monitored structure is even facilitated by the insertion of defined fault locations in the sensing fiber. Still, the limitation of the measurement range even when using novel low-loss POF constrains the field of applications of this method in flood protection.

1.3 Distributed Brillouin sensing

Among all the techniques that were introduced in the preceding section, there is none that exactly fits the requirements of dike monitoring. The solution comes with distributed Brillouin sensing: Here, a continuous profile of the longitudinal strain as well as the temperature along a silica optical fiber over a length of several ten kilometers can be recorded. This forms a truly distributed sensor (each infinitesimal spatial point along the fiber provides information on the local quantity of strain and temperature) over a long distance and thereby fills the gap that has become apparent from the above comprehension. A detailed examination of the physical backgrounds and an extensive description of several approaches of implementation will be given throughout this thesis; at this point, only the most relevant characteristics of distributed Brillouin sensing are introduced. Apart from the system cost (which strongly depends on circumstances that are not necessarily connected to technical issues) there are four basic parameters that characterize the performance of state-of-the-art Brillouin sensors and thereby define the feasibility for the respective application:

1. The measurement length of modern Brillouin sensing systems lies in the range of up to 100 km for fibers under laboratory conditions. In real-life applications, this length decreases due to optical losses induced in the fiber during integration into the structure. Still, a range of 10 to 20 km can be achieved [12].

2. A spatial resolution of less than one meter is achieved by commercially available Brillouin sensing systems. A physical explanation for this restraint in spatial resolution as well as several approaches to overcome this limitation will be given in later sections.

3. The temperature resolution lies in the range of 1 K. Strain resolutions of less than 50 $\mu\varepsilon$ have been reported. For many applications, the separation of these two measurands is a critical issue, since both quantities have a largely identical impact on the optical measurement signal. Different approaches to deal with this basic problem will be discussed [12], [13].

4. Minimum time for data acquisition may vary between a few minutes and about an hour, depending on the method used to obtain the spatially resolved measurement trace. A measurement time of approximately 30 minutes is a reasonable benchmark for common sensing units [12].

Each of the parameters listed above represent the technical standard within their category. It is not provided that all four parameters are available with their optimum value at the same time. As will be shown later, each parameter can be improved at the expense of the others. For instance, a higher spatial resolution will decrease the resolution of the measurands; a larger measurement length will need more time for data acquisition.

Several systems using SBS for distributed measurement of strain and temperature are commercially available. Common fields of application are monitoring of composite tubes [14], bridges [15], landfills [16], pipelines [17] and similar wide-stretching structures; even in flood protection, first pilot projects have been reported [18], [19].

The following comprehension of the advancement and implementation of distributed Brillouin sensing starts with a theoretical view at the physical basics beneath the phenomenon of stimulated Brillouin scattering in chapter 2. Two techniques of acquiring the spatially resolved information from the measurement signal will be presented in chapter 3: The classical Brillouin optical time domain analysis (BOTDA), and the Brillouin optical frequency domain analysis (BOFDA), the investigation and advancement of which is the main subject of this work. The laboratory setup along with characteristic measurement results will be laid out in chapter 4. The concept of a novel method for data acquisition using digital hardware and signal processing will be presented in chapter 5. Chapter 6 discusses the effect limiting the spatial resolution of Brillouin sensing for the techniques that have been discussed so far; an analytical approach to overcome this limitation will be presented. Chapter 7 finally comes back to the original task of dike monitoring: The development of the methods for integration of silica optical fibers into the soil body of dikes will be discussed. Several tests performed in the laboratory and under field-like circumstances will be presented. The thesis will conclude with a summary and an overview over possible aspects of further investigations on the subject in chapter 8.

CHAPTER 2

Stimulated Brillouin scattering in optical fibers

In its most comprehensive definition, Brillouin scattering describes the scattering of electromagnetic waves by propagating acoustic phonons. The existence of such a scattering process was first predicted in 1922 [20], but could not be experimentally verified before 1964, when coherent laser sources became available.

This chapter will give a more descriptive presentation of this physical phenomenon, dealing specifically with the case of Brillouin scattering within silica optical fibers. After outlining the very basic principle of Brillouin scattering, a more detailed investigation will lead to the concept – and the limitations, the most challenging aspects of this work – of Brillouin sensing for distributed strain measurements.

2.1 Theoretical background

2.1.1 Basic introduction to stimulated Brillouin scattering

Figure 2.1 provides a very rough overview of the physical process: Brillouin scattering can be seen as the interaction of two counterpropagating light waves with an acoustic wave within the optical fiber. The reciprocal nature of the phenomenon is evident from the cyclic structure of cause and consequence. The challenge of coming up with a comprehensive and understandable explanation for the effect lies in the choice of the starting point: the two main issues – on the one hand, the alteration of the density of the medium by an electromagnetic field, on the other hand, light being scattered by periodic density fluctuations – mutually depend on each other, and the question of what is responsible for the excitation of the process comes close to the problem of the chicken and the egg.

Looking at the propagation of a light wave through an optical fiber under ordinary conditions – such as an optical signal traveling along a silica fiber for data transmission – a number of scattering phenomena can be observed. Apart from the ever-present Rayleigh scattering due to irregularities in the molecular structure of any optical fiber, scattering will also occur at density fluctuations within the fiber caused by thermal noise. The conceptional distinction between spontaneous and stimulated scattering has been formulated in [21].

For Brillouin scattering, this distinction is defined as follows: As long as the amount of light that is scattered by thermal fluctuations is too small to excite further fluctuations in the density of the medium, the process remains linear and is known as spontaneous Brillouin scattering.

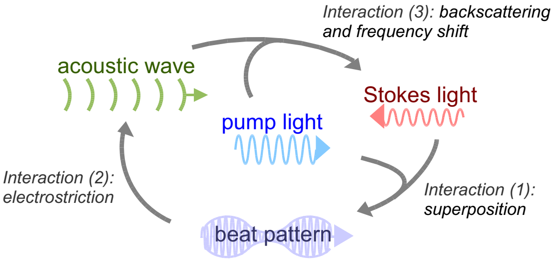

Figure 2.1: Basically, stimulated Brillouin scattering can be expressed as the mutual interaction of two light waves and an acoustic wave. The three stages of interaction are explained in the following.

In contrast, a number of scattered photons $N_s \gg 1$ leads to the effect known as stimulated Brillouin scattering (SBS). In the following, this process will be analyzed for light waves that propagate through an optical fiber, where the geometry simplifies to a single dimension. The incident light wave will be called the pump wave, traveling in positive z direction; it interferes with a light wave (denominated as the Stokes wave) that travels through the fiber in negative z direction[1]. This counterpropagating light wave may have arisen from scattering at thermal fluctuations, but may also have been injected from the opposite fiber end by a light source. In both cases, its presence fulfills the definition of stimulated scattering from [21].

The electromagnetic fields of the two waves will superpose in a way such that the corresponding optical intensities form a beat pattern (interaction stage (1) in figure 2.1). The resulting electromagnetic field of this beat pattern will apply an electrostrictive force to the molecular structure of the medium, resulting in periodic fluctuations in its density (interaction stage (2) in figure 2.1). If the induced den-

---

[1] In some references, the terms *probe wave* instead of Stokes wave and *signal wave* instead of pump wave are found.

sity fluctuations add up constructively, they will form an acoustic wave, which will propagate along the fiber at the medium's acoustic velocity v_a.

The condition for constructive creation of the acoustic wave can directly be derived from the conservation of energy and momentum. Energy conservation determines the acoustic wave's frequency ω_a with

$$\omega_a = \omega_p - \omega_s \tag{2.1}$$

where ω_p and ω_s are the frequencies of the pump and the Stokes wave. Momentum conservation results in the acoustic wave's wave vector $\vec{k}_a$ with

$$\vec{k}_a = \vec{k}_p - \vec{k}_s \tag{2.2}$$

where $\vec{k}_p$ and $\vec{k}_s$ are the wave vectors of the pump and the Stokes wave. With the geometrical limitation of an optical fiber, the relation of the wave numbers becomes

$$k_a = k_p + k_s \tag{2.3}$$

with $|\vec{k}_p| = k_p$, $|\vec{k}_s| = k_s$, $|\vec{k}_a| = k_a$ (see figure 2.2).

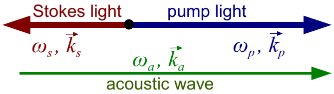

Figure 2.2: Orientation of the wave vectors involved in stimulated Brillouin scattering in an optical fiber.

Due to the very small frequency difference between the two light waves compared to their optical frequencies, the approximations of equal wave lengths for pump and Stokes light $\lambda_p \approx \lambda_s$ and the wave length of the acoustic wave $\lambda_a \approx \lambda_p/2$ will be used in the following.

Even if no counterpropagating Stokes light is injected into the fiber, a strong incident pump wave can initiate the scattering. In this case, equations (2.1) and (2.2) imply the following: Of all photons scattered by thermal fluctuations, only those will contribute to a viable acoustic wave that – superposing with the pump photons – form a beat pattern which would match the acoustic velocity v_a. This condition is fulfilled for all photons of a frequency that is lower than that of the pump wave by the frequency difference f_B, called the Brillouin frequency shift [22]:

$$f_B = \frac{v_a 2n}{\lambda_p} = \frac{\omega_a}{2\pi} \tag{2.4}$$

with n being the refractive index of the fiber.

The propagating fluctuations in the medium's density – being the acoustic wave – are seen now as a periodic grating by the pump light, at which backscattering occurs.

Due to the propagation of the grating at acoustic velocity, the pump light is shifted downwards in frequency by the Doppler shift. Energy conservation is fulfilled, and the backscattered and downshifted pump light matches the Stokes light in frequency and phase (interaction stage (3) in figure 2.1). Thus, the stimulated process creates a Stokes light wave of a determined frequency, which depends on the incident wavelength λ_p, the acoustic velocity v_a and the refractive index n.

However, despite the phase-match condition for the excitation of the acoustic wave by the exciting beat pattern, even scattered photons with frequencies slightly off the requested exact f_B will contribute to the stimulated process: Any medium provides a finite acoustic damping rate Γ (corresponding to the lifetime of the acoustic phonons $\tau_B = 1/\Gamma$). Thus, the Stokes light emerging from stimulated Brillouin scattering will be of an optical linewidth δf_B. The damping rate determines the linewidth of stimulated Brillouin scattering for each specific medium.

As a consequence of the above, the case of an injected counterpropagating Stokes light wave can be considered. The Stokes light has the frequency ω_s; with the pump frequency ω_p, it forms an intensity beat pattern, the envelope of which has the frequency ω_0. The frequency offset between pump and Stokes light is denominated as Δf with

$$\Delta f = \frac{\omega_p - \omega_s}{2\pi} = \frac{\omega_0}{2\pi} \tag{2.5}$$

The beat pattern is only able to initiate a viable acoustic wave, if the frequency offset between pump and Stokes light matches the Brillouin frequency shift f_B. In this case, interaction is straightforward: The envelope of the beat pattern applies an electrostrictive force to the medium, inducing density fluctuations that propagate at acoustic velocity. The backscattered pump light will match the Stokes light's frequency and phase, so that a power transfer from the pump and Stokes light will occur whenever the resonant condition $\Delta f = f_B$ is fulfilled.

A slight detuning of the frequency offset Δf from this condition will still enable the beat pattern to excite a viable acoustic wave, again due to the finite acoustic damping rate of any medium. The Brillouin linewidth δf_B determines the allowed bandwidth for Δf to achieve a power transfer from the pump to the Stokes wave.

With this amplification process, the cycle from figure 2.1 is complete. It becomes clear that the effect of stimulated Brillouin scattering may arise from the presence of a single pump wave: spontaneous Brillouin scattering will provide the Stokes field for the stimulated process, since the light scattered at thermal fluctuations (which, being acoustic phonons, feature all the characteristics of the acoustic wave) will have the matching frequency shift required by the resonance condition. The transition from spontaneous to stimulated Brillouin scattering presumes a certain quantity of optical power for the pump wave, which strongly depends on the interaction length. This relation will be experimentally explored and quantified in section 2.2.2.

In contrast, the excitation of stimulated scattering by injecting two counterpropagating waves into the fiber requires a precise tuning of the frequency offset between the two light sources to the required frequency match. If this tuning succeeds, a power transfer from the pump wave to the Stokes wave can be generated at power levels much lower than those required for self-induced scattering.

2.1.2 Deeper analysis of three-wave interaction

In order to grasp the principle of Brillouin sensing for distributed strain measurement – whether the measurement is performed in the time domain or the frequency domain – the explanations given in section 2.1.1 will suffice to understand most aspects of state-of-the-art measurement devices. However, these techniques meet some limitations when driven to ever-higher performance in terms of spatial resolution and accuracy of the measurand. Both the causes of these limitations and potential approaches to overcome them require a deeper understanding of the physical background of stimulated Brillouin scattering.

This section is based on the theoretical views on stimulated Brillouin scattering as they have been laid out by Kaiser and Maier [21] and Guang and Song [23], to provide a detailed analysis of the interaction between the three waves involved in the process. The focus of the investigations lies on the spectral characterization of the acoustic wave, which requires a thorough analysis of its excitation by the beat pattern of the optical intensities.

While chapters 3, 4 and 5 deal with the theory and implementation of spatially resolved strain measurements, chapter 6 will scrutinize the impact of modulated optical intensities on stimulated Brillouin scattering and will therefore intensely come back to the following analysis.

Excitation of the acoustic wave

The following analysis, just as the overview from the preceding section, follows the cyclic structure of the physical processes involved in stimulated Brillouin scattering (figure 2.1). It maintains the chosen starting point, which is the excitation of the acoustic wave by the presence of an intensity beat pattern of two counterpropagating waves. The subsequent paragraph will then describe the impact of the acoustic wave on the present light fields, to complete the cycle.

In [23], a moving mass element in a medium is described by the following dynamical equation:

$$\nabla P + \Gamma \rho_0 \vec{V} + \rho_0 \frac{\partial \vec{V}}{\partial t} = \frac{\varepsilon_0 \gamma^e}{2} \nabla \left(\vec{E}^2 \right) \tag{2.6}$$

This basic relation of continuum mechanics is the Navier-Stokes equation [21], reduced by the impact of temperature fluctuations [24].

The first term (the gradient of pressure P) represents the force upon the unit volume of the medium. The second term is the damping force of a moving particle with velocity $\vec{V}$, damping factor Γ and the medium's average density ρ_0. The third term represents the force proportional to mass and acceleration [23]. On the right side of equation 2.6, the force on the medium applied by an intense optical field is represented: Under the action of an optical field $\vec{E}$, the elementary particles of a medium will encounter an electrostrictive force that is proportional to the gradient of the square of the field: $\nabla(\vec{E}^2)$ [23]. The coupling coefficient between the medium's permittivity ε and small density fluctuations $\hat{\rho}$ is called the electrostrictive coefficient γ^e:

$$\gamma^e = \rho_0 \frac{\partial \varepsilon}{\partial \hat{\rho}} \tag{2.7}$$

Equation (2.6) is completed by the conservation of mass, formulated in the equation of continuity

$$\frac{\partial \hat{\rho}}{\partial t} + \rho_0 \nabla \cdot \vec{V} = 0 \tag{2.8}$$

in which the elastic motion of the medium is represented by the density fluctuations $\hat{\rho}$. Equations (2.6) and (2.8) are combined, then a divergence operation is performed on both sides:

$$\nabla^2 P - \Gamma \frac{\partial \hat{\rho}}{\partial t} - \frac{\partial^2 \hat{\rho}}{\partial t^2} = \frac{\varepsilon_0 \gamma^e}{2} \nabla^2 \left(\vec{E}^2 \right) \tag{2.9}$$

With the adiabatic modulus of elasticity

$$\beta = \rho_0 \frac{\partial P}{\partial \rho} \tag{2.10}$$

which, in turn, is connected to the acoustic velocity v_a by

$$v_a^2 = \frac{\beta}{\rho_0} \tag{2.11}$$

equation (2.9) becomes

$$v_a^2 \nabla^2 \hat{\rho} - \Gamma \frac{\partial \hat{\rho}}{\partial t} - \frac{\partial^2 \hat{\rho}}{\partial t^2} = \frac{\varepsilon_0 \gamma^e}{2} \nabla^2 \left(\vec{E}^2 \right) \tag{2.12}$$

Equation (2.12) represents the excitation of density fluctuations in the medium by an intense optical field and is the desired description of an acoustic wave, excited by a light wave.

The analysis now presumes the presence of the two counterpropagating optical fields involved in stimulated Brillouin scattering (the pump field $\vec{E}_p$ and the Stokes field $\vec{E}_s$), for which a plane wave approximation with slowly varying amplitudes E_p and E_s in an optical fiber (with z being the only spatial dimension) is used.

$$\begin{aligned} \vec{E}_p &= \frac{1}{2} \left(E_p e^{j(\omega_p t - k_p z)} + E_p^* e^{-j(\omega_p t - k_p z)} \right) && (2.13) \\ \vec{E}_s &= \frac{1}{2} \left(E_s e^{j(\omega_s t + k_s z)} + E_s^* e^{-j(\omega_s t + k_s z)} \right) && (2.14) \end{aligned}$$

Equations (2.13) and (2.14) are introduced into (2.12). At this point, deviating from the descriptions found in literature [21], [23], a more detailed analysis of the right side of (2.12) is needed: The optical field $\vec{E}$ is now composed of the superposition of two signals; in the following, an analysis for the case of signals of a single optical frequency (ω_p and ω_s, respectively) will be given. Based on this analysis, chapter 6 will investigate the presence of optical signals that are modulated in their amplitudes.

The excitation according to (2.12) is determined by the second spatial derivative of the squared superposition of the pump field $\vec{E_p}$ and the Stokes field $\vec{E_s}$:

$$\nabla^2\left(\vec{E}^2\right) = \frac{\partial^2}{\partial z^2}\left(\left(\vec{E_p}+\vec{E_s}\right)^2\right) \tag{2.15}$$

Here, the quadrature of the two fields is the exact description of the beat pattern of the optical intensities, which had already been considered as the acoustic wave's excitation in section 2.1.1.

Introducing the harmonic ansatz, the excitation becomes

$$\nabla^2\left(\vec{E}^2\right) = \frac{\partial^2}{\partial z^2}\left(\frac{1}{2}\left(E_p e^{j(\omega_p t - k_p z)} + \text{c.c.} + E_s e^{j(\omega_s t + k_s z)} + \text{c.c.}\right)\right)^2 \tag{2.16}$$

The full expansion and spatial derivation of (2.16) is performed in appendix B.1. As a result, it is stated that – among the numerous spectral components of the intensity of the beat pattern – only the component

$$-k_0^2 E_p E_s^* e^{j((\omega_p-\omega_s)t-(k_p+k_s)z)} = -k_0^2 E_p E_s^* e^{j(\omega_0 t - k_0 z)} \tag{2.17}$$

and its complex conjugate are located in the spectral range that is relevant for the excitation of an acoustic wave. This is the spectral component of the beat signal which represents the envelope.

Finally, an amplitude function ρ is introduced for the acoustic wave with

$$\hat{\rho} = \frac{1}{2}\left(\rho e^{j(\omega_a t - k_a z)} + \rho^* e^{-j(\omega_a t - k_a z)}\right) \tag{2.18}$$

that is inserted into the left side of (2.12) (the right side of which is simplified according to (2.16)). Second derivatives are neglected, resulting in the final equation for the acoustic wave:

$$j\omega_a v_a \frac{\partial \rho}{\partial z} + (\Gamma + 2j\omega_a)\frac{\partial \rho}{\partial t} + \left(\omega_a^2 + j\omega_a\Gamma\right)\rho = \frac{\varepsilon_0\gamma^e k_0^2}{2} E_p E_s^* e^{j((\omega_0-\omega_a)t-((k_0-k_a)z)} \tag{2.19}$$

Equation (2.19) is the first of three coupled differential equations that fully describe stimulated Brillouin scattering and are commonly used as an equation set in literature.

In (2.17), the envelope frequency $\omega_0 = \omega_p - \omega_s = 2\pi\Delta f$ is introduced. When the resonant condition from section 2.1.1, being $\Delta f = f_B$, is matched, the envelope frequency coincides with the frequency of the acoustic wave ($\omega_0 = \omega_a$ and $k_0 = k_a$); in this case, the relations (2.1) and (2.3) are fulfilled. The exponential term on the right side of equation (2.19) vanishes, and the acoustic wave enables maximum power transfer from the pump to the Stokes wave.

For the case of a detuning between the acoustic wave and the exciting envelope frequency, Brillouin interaction decreases towards zero. Here, the spectral width of the excitation of the density fluctuations – the Brillouin linewidth – is defined, which determines the dependence between the SBS power transfer and the frequency detuning $(f_B - \Delta f)$. This gain curve, called the Brillouin gain spectrum (BGS), has the shape of a Lorentz function [22]:

$$g_B(\Delta f - f_B) = g_{Bmax} \frac{(\Gamma/2)^2}{(2\pi\,(\Delta f - f_B))^2 + (\Gamma/2)^2} \tag{2.20}$$

The parameter g_{Bmax} denotes the maximum value of the gain spectrum; a calculation for its value can be found in literature [22], but since it depends on parameters which are difficult to get hold of accurately (e.g. the electrostriction coefficient γ^e, spatially dependent polarization issues etc.), it will not be given here. Furthermore, it plays a minor role in the analysis of the measurement signals in Brillouin sensing. Much more relevant is the width of the spectrum, which is indicated by the value FWHM (full width at half maximum); it is denoted with δf_B, corresponding to $\Gamma/(2\pi)$.

Equation (2.19) fully describes the excitation of the acoustic wave by a propagating field of alternating intensity. For the beat pattern on the right side of the equation, a steady-state ansatz with a single frequency component in each field in equation (2.16) was used. With less spectrally pure conditions – such as pulsed or modulated light waves – (2.16) will not that easily expand to (2.17) giving the beat pattern with an envelope of one single component. Such cases will be further investigated in chapter 6. For now, the spectral bandwidths of the involved light waves are demanded to be much smaller than the Brillouin linewidth, which shall suffice to keep the considerations of this section valid.

Interaction of light fields with a scattering medium

Nonlinear scattering processes such as Raman and Brillouin scattering can be explained by introducing a nonlinear electrical polarization term into the field equations. This nonlinearity describes the behavior of a field-dependent susceptibility χ of a dielectric medium: The field of an electromagnetic wave leads to a shift of electric dipole moments within the structure of the medium. For small fields, the susceptibility is a proportionality constant coupling the electrical field $\vec{E}$ to the electrical polarization $\vec{P}$ with $\vec{P} = \varepsilon_0 \chi \vec{E}$. At high field intensities, the electrical polarization can not follow the field amplitude and loses its proportional dependence on the electric field [25]. $\vec{P}$ then splits into a linear electrical polarization $\vec{P}_L$ and a nonlinear electrical polarization $\vec{P}_{NL}$. For such behavior, a power series

$$\vec{P} = \underbrace{\varepsilon_0 \chi^{(1)} \vec{E}}_{\vec{P}_L} + \underbrace{\varepsilon_0 \chi^{(2)} \vec{E}^2 + \varepsilon_0 \chi^{(3)} \vec{E}^3 + \dots}_{\vec{P}_{NL}} \tag{2.21}$$

can be written. In this, the second term is connected to frequency doubling and mixing of two light fields. For this work, the third term is relevant, as it describes – among other physical effects – stimulated scattering processes [21].

In Maxwell's equations for the electric field $\vec{E}$ and the magnetic field $\vec{H}$ in a dielectric, non-magnetic medium

$$\nabla \times \vec{E} = -\frac{\partial \vec{B}}{\partial t} \tag{2.22}$$

$$\nabla \times \vec{H} = \frac{\partial \vec{D}}{\partial t} \tag{2.23}$$

the nonlinear electrical polarization is introduced via the displacement field $\vec{D}$ [21]:

$$\begin{aligned} \vec{D} &= \varepsilon_0 \vec{E} + \vec{P} \\ &= \varepsilon_0 \vec{E} + \varepsilon_0 \chi^{(1)} \vec{E} + \vec{P}_{NL} \\ &= \bar{\varepsilon} \vec{E} + \vec{P}_{NL} \end{aligned} \tag{2.24}$$

introducing the medium's average permittivity $\bar{\varepsilon} = \varepsilon_0 \bar{\varepsilon}_r = \varepsilon_0(1 + \chi^{(1)})$. With the further relations

$$\vec{B} = \mu_0 \vec{H},\ \mu_r = 1 \tag{2.25}$$

and

$$\mu \bar{\varepsilon} = \mu_0 \varepsilon_0 \bar{\varepsilon}_r = \frac{\bar{\varepsilon}_r}{c_0^2} \tag{2.26}$$

with the vacuum light speed c_0, equations (2.22) and (2.23) are combined to the wave equation:

$$\nabla \times \vec{B} = \frac{\bar{\varepsilon}_r}{c_0^2} \frac{\partial \vec{E}}{\partial t} + \mu_0 \frac{\partial \vec{P}_{NL}}{\partial t} \tag{2.27}$$

$$\nabla \times \nabla \times \vec{E} = -\nabla^2 \vec{E} \tag{2.28}$$

$$\nabla^2 \vec{E} - \frac{\bar{\varepsilon}_r}{c_0^2} \frac{\partial^2 \vec{E}}{\partial t^2} = \mu_0 \frac{\partial^2 \vec{P}_{NL}}{\partial t^2} \tag{2.29}$$

Charge free space is assumed; propagation losses along the medium (i.e. optical attenuation of the fiber) are neglected for the conceptional considerations in this section. The nonlinear electrical polarization is now expressed by a permittivity deviation $\Delta\varepsilon$ from the medium's average (the total permittivity being $\varepsilon = \bar{\varepsilon} + \Delta\varepsilon$) [26]:

$$\vec{P}_{NL} = \Delta\varepsilon \vec{E} \tag{2.30}$$

The wave equation (2.29) becomes (with $\Delta\varepsilon = \varepsilon_0 \Delta\varepsilon_r$):

$$\nabla^2 \vec{E} - \frac{\bar{\varepsilon}_r}{c_0^2} \frac{\partial^2 \vec{E}}{\partial t^2} = \frac{1}{c_0^2} \frac{\partial^2 \vec{E} \Delta\varepsilon_r}{\partial t^2} \tag{2.31}$$

With the electrostriction coefficient γ^e from equation (2.7), a change in permittivity is connected to density deviations $\hat{\rho}$ from the average density ρ_0 [23]:

$$\Delta\varepsilon_r = \frac{\gamma^e}{\rho_0} \hat{\rho} \tag{2.32}$$

Finally, this dependence provides the relation between density fluctuations in a medium and the propagation of an optical wave:

$$\nabla^2 \vec{E} - \frac{\bar{\varepsilon}_r}{c_0^2} \frac{\partial^2 \vec{E}}{\partial t^2} = \frac{\gamma^e}{\rho_0} \frac{1}{c_0^2} \frac{\partial^2 \vec{E}\hat{\rho}}{\partial t^2} \tag{2.33}$$

Consequently, euqation (2.33) can describe the impact of an acoustic wave on each of the propagating optical signals $\vec{E}_p$ and $\vec{E}_s$.

Thus, nonlinear electrical polarization has been expressed by the multiplication of an electrical field and an acoustic wave $\vec{E}\hat{\rho}$. If this multiplication is performed for each of the participating light waves, using the harmonic expressions from equations (2.13), (2.14) and (2.18), the products

$$\begin{aligned} \vec{E}_p\hat{\rho} = \frac{1}{4} \Big(& E_p \rho e^{j((\omega_p+\omega_a)t+(-k_p-k_a)z)} + E_p \rho^* e^{j((\omega_p-\omega_a)t+(-k_p+k_a)z)} \\ & + E_p^* \rho e^{-j((\omega_p-\omega_a)t+(-k_p+k_a)z)} + E_p^* \rho^* e^{-j((\omega_p+\omega_a)t+(-k_p-k_a)z)} \Big) \end{aligned} \tag{2.34}$$

and

$$\begin{aligned} \vec{E}_s\hat{\rho} = \frac{1}{4} \Big(& E_s \rho e^{j((\omega_s+\omega_a)t-(-k_s+k_a)z)} + E_s \rho^* e^{j((\omega_s-\omega_a)t-(-k_s-k_a)z)} \\ & + E_s^* \rho e^{-j((\omega_s-\omega_a)t-(-k_s-k_a)z)} + E_s^* \rho^* e^{-j((\omega_s+\omega_a)t-(-k_s+k_a)z)} \Big) \end{aligned} \tag{2.35}$$

are obtained. In (2.34), the exponent of the second term (and its conjugate in the third term) fulfills the relations (2.1) and (2.3). Consequently, from the interaction of the pump light with the acoustic wave, a term with the amplitude $E_p\rho^*$ results that matches the frequency, the wave vector and the propagation direction of the Stokes wave, being responsible for the Brillouin gain. In contrast, in (2.35) it is the first term (and its complex conjugate in the fourth term) matching theses conditions; in consequence, the term with $E_s\rho$ matches the frequency, the wave vector and the propagation direction of the pump wave. The remaining summands in both equations correspond to no physically relevant frequency components and will be neglected.

The amplitudes can be used to obtain the final differential equations for both Stokes and pump field from (2.33):

$$\frac{\partial E_p}{\partial z} + \frac{n}{c_0} \frac{\partial E_p}{\partial t} = \frac{j\omega_p}{4c_0 n} \frac{\gamma^e}{\rho_0} E_s \rho \tag{2.36}$$

$$-\frac{\partial E_s}{\partial z} + \frac{n}{c_0} \frac{\partial E_s}{\partial t} = \frac{j\omega_s}{4c_0 n} \frac{\gamma^e}{\rho_0} E_p \rho^* \tag{2.37}$$

Again, second derivatives are neglected; the refractive index $n = \sqrt{\bar{\varepsilon}_r}$ is introduced. Equations (2.19), (2.36) and (2.37) form the set of differential equations that is commonly found in literature.

Outlook: Nonlinear characteristics of the three-wave equations

While in most discussions, the three equations are normalized in order to obtain a form as homogeneous as possible (as it is done in [27]), such a forced homogeneity might conceal a significant difference between (2.36) and (2.37) on the one hand and (2.19) on the other. This difference has its origin in equation (2.12), where the square of the electric field is responsible for the excitation of an acoustic wave. This nonlinear operation is applied to the superposition of two light waves of different frequencies, resulting in a number of new lines in the frequency spectrum, of which in this section only the line forming the envelope of the beat signal has been accounted for. In contrast to this nonlinearity, the multiplication from (2.33), that results in (2.36) and (2.37), can be seen as a linear depletion of the pump wave and a linear amplification of the Stokes wave. The acoustic wave ρ has a limited spectrum; no frequency mixing will occur. All three equations are represented in the spectral scheme of Brillouin interaction which is given in figure 2.3.

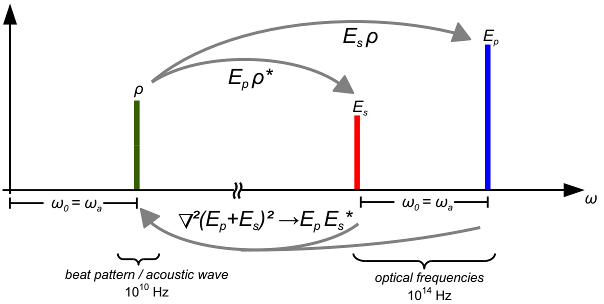

Figure 2.3: Spectral representation of SBS interaction with the excitation mechanisms from equations (2.19), (2.36) and (2.37).

For the description of an intense light wave of a single frequency injected into a fiber and its scattering at the acoustic wave emerging from spontaneous Brillouin scattering, such frequency mixing has no relevance; similar considerations hold true for the excitation of SBS by injecting two counterpropagating light waves with a defined frequency offset. However, the acquisition of spatially resolved Brillouin gain spectra requires the use of modulated light, as it will be explained in chapter 3. Here, several frequency components (or, in the case of pulse modulation, a continuous spectrum) are involved in the nonlinear interaction; at this point, the quadrature term of equation (2.12) becomes highly relevant. Phenomena that are caused by the problem of frequency mixing – and that lead to a degradation of the sensing performance – will be discussed in chapter 6.

2.1.3 Impact of the optical polarization

In the above sections, stimulated Brillouin scattering has been described as the interaction between two counterpropagating light waves; the intensity of the interaction is reflected in the maximum gain of the Stokes beam at cost of the pump power, to be measured at an frequency offset Δf corresponding to the Brillouin frequency shift f_B. This maximum Brillouin gain is largely determined by material parameters of the fiber and the optical wavelength (equation (2.4)). In addition, the relative position of the states of polarization (SOP) of the two light waves has a significant impact on the intensity of the interaction: Since Brillouin interaction is governed by the emergence of an acoustic wave from the electric field of a beat pattern (formulated in equation (2.12)), it is evident that in case of perfectly orthogonal polarization states of the two light waves, no Brillouin gain will be measured, since the intensities will not form any beat (in analogy to the penalty for polarization mismatch in a coherent receiver). In turn, maximum interaction will occur in case of two identical states of polarization.

Due to the birefringence of standard silica fibers, the state of polarization of a light wave injected into the fiber will change while propagating along. It will adopt all possible states within the beat length L_B with

$$k_x L_B - k_y L_B = 2\pi \tag{2.38}$$

where k_x and k_y are the wave numbers of the fast and slow polarization axes. Thus, L_B is the measure that quantifies the fiber's birefringence.

As a consequence, a spatially resolved measurement trace of the Brillouin gain will show strong fluctuations, with some sections of maximum gain and others of almost no interaction. The most comprehensive description of these relations has been provided by Deventer *et al.* [28], which shall be briefly summarized in the following.

Under the premise that in any linear optical medium orthogonality as well as coincidence („identicality“) of polarization are preserved along the entire path of two counterpropagating light waves (the vaildity of which had been demonstrated earlier [29]), the fluctuations can be interpreted as illustrated in figure 2.4.

In a low-birefringent fiber, all polarizations occur with equal probability. Interaction becomes optimal when the orientation, the ellipticity and the sense of rotation of the states of polarization for pump and Stokes are identical when seen from one direction. However, when the sense of rotation is identical, the orientation is inverse; this leads to the mixing efficiencies of $\gamma_P = 2/3$ for coinciding polarizations and $\gamma_P = 1/3$ for orthogonal polarizations. This factor enters the calculation of the maximum Brillouin gain; it can be verified by measuring the overall Brillouin gain of a fiber that is longer than the beat length.

In spatially resolved measurements, periodic fluctuations of Brillouin gain are observed; the exact location of minima and maxima of the interaction can be influenced by altering the polarization state of one of the two beams when entering the fiber. Also the total quantity of sections with disappearing Brillouin gain can be minimized by setting the two lasers to orthogonal polarization states. Still, in order to obtain

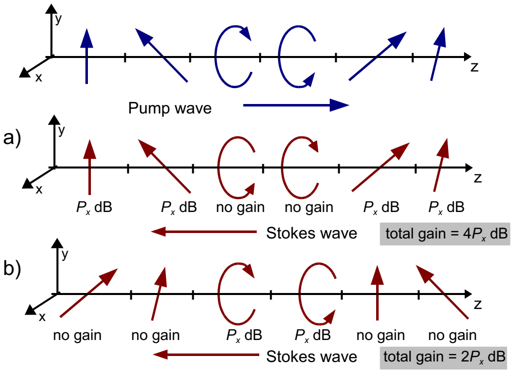

Figure 2.4: Polarization dependence of Brillouin gain in standard (low-birefringence) optical fibers. (a) Identical and (b) orthogonal polarization of pump and Stokes wave [28].

a homogeneous gain signal over the entire fiber length, more effort has to be made; approaches to overcome the problem will be discussed in section 4.3.

Since the gain fluctuations in spatially resolved Brillouin measurements are periodical with L_B, the actual beat length of the fiber can be derived from such measurements [30]. By means of this method, the beat length has been estimated to be $L_B \approx 50$ m in standard single-mode optical fibers.

2.1.4 Light sources and scattering media

When stimulated Brillouin sensing was first investigated in the 1960s, its primary application was expected to emerge from the field of spectroscopy. Therefore, detailed analyses [21] kept their focus on SBS occurring in solid bulk media as well as liquids and gases, into which large amounts of optical power were sent by means of laser sources that were available in those days.

With silica fibers being used as waveguides for optical signals, optical communication systems have soon found their irreplaceable part in modern technology. Within such waveguides, high densities of optical power are easily achieved,and stimulated Brillouin scattering soon emerged as an unwanted side-effect occurring in optical communication links. In such cases, SBS limits the maximum power which can be transferred by an optical pulse.

When first distributed fiber optic sensing systems were presented in the 1980s, the spectroscopic capabilities of SBS were rediscovered, now employing silica optical fibers as scattering media; naturally, laser technology had advanced dramatically in the meantime, providing new light sources for precise excitation of the phenomenon. Leaving all technology needed for the scanning of the Brillouin gain spectra and data acquisition for the next chapters, this section will provide a brief collection of the characteristics of the physical requisites of SBS, being the optical fibers themselves as well as the light waves, injected into the fibers from laser sources.

Silica optical fibers

The sensing system presented in this thesis bases on the usage of standard telecommunication single-mode silica optical fibers. This might appear as a straight-forward choice in favor of easily-available material which will form the sensors in the lab as well as in the field. Here, more motivation than easy availability for this choice shall be given with respect to the numerous varieties of dielectric waveguides that play a role in today's optical communication technology.

Thus, the questions that arise concerning the motivation for the fibers of choice – namely, CORNING's SMF-28e [31] – are the following:

- Why **silica fibers**? – While silica optical fibers have governed the field of fiber-optic technology for several decades, polymer optical fibers (POF) have emerged in the last years, offering several advantages: They are cheap; they are easily manageable concerning assembly of cables and, especially, connectors (which is due to the large core diameters and the resulting high numerical aperture); they are mechanically robust, which makes them attractive for applications in rough conditions (like construction sites); and, finally, they can handle strain which elongates the fiber for more than 40 %, which forms an enormous advance over silica fibers with their maximum strain of 1-2 %.

  Especially the last two aspects would make an attempt to employ POF for distributed Brillouin sensing very attractive. On the other hand, the disadvantages are quite critical: Their high attenuation (150 dB/km compared to 0.3 dB/km at $\lambda = 1320$ nm in silica) would require high optical power in order to excite stimulated Brillouin interaction. The estimated power values needed for excitation of SBS are even increased by the problem of strong modal dispersion which has been observed to split up the propagation paths of the light within a few centimeters of POF.

  Efforts have been made in order to examine the potential of POF for Brillouin sensing [32]; by the time of writing, no evidence of SBS in POF could be given.

- Why **single-mode fibers**? – The main advantage of multi-mode optical fibers in sensing applications is their insensitivity to small bending radii. While standard single-mode fibers are specified to endure a full loop with a radius as small as 16 mm without significant increase of attenuation (≤ 0.05 dB, [31]), and showed an attenuation of 1 dB at a bending radius of 9 mm; multi-mode fibers have been observed to withstand radii as small as 2 mm with extra attenuation < 1 dB [32].

  The problem with these figures is that they demand the light waves to propagate only in the fundamental mode of the fiber – a prerequisite that also has to be made for the measurement of Brillouin gain spectra, because the conversion of the injected light to higher modes dramatically decreases the signal-to-noise ratio in such measurements [32]. Such an excitation is complicated to achieve and not very robust over the length of a mechanically stressed fiber; still, multi-mode fibers remain attractive candidates for Brillouin sensing and should encourage further research in order to overcome the difficulties.

- Why **standard telecommunication fibers**? – Numerous variants of silica optical fibers for all kinds of special applications have entered the market, differing in the diameters of core and cladding, material parameters (such as dopants), coating material etc. Two parameters that are relevant for the performance of a Brillouin sensing system are affected by such variations: First, the problem of small bending radii might be overcome by more complex coating technologies. With such special fibers, the demand on the cabling technology, which is to protect the fiber from mechanical stress while maintaining its sensitivity to longitudinal strain (see section 7.2.2) – might be fulfilled more efficiently. Still, the cost of any specialty fiber will be higher by at least one order of magnitude than of standard telecommunication fibers. Since the aim of this research is a cost-efficient system with sensing lengths of tens of kilometers, the focus on standard fibers with minimum material costs is the only reasonable choice.

  Second, dopants within the fiber material – generally introduced in order to tune material dispersion or to produce active optical materials – affect the value of the Brillouin frequency shift f_B. Since there are some variants of fibers with dopants differing from standard fibers which are employed in telecommunications in a large scale (and, therefore, just as cheap), their characteristics concerning Brillouin scattering have been investigated (such as non-zero dispersion shifted fibers (NZDSF) [33]). Since the focus of this work is the development of a strain sensor to be applied in practice – which is efficiently achieved with standard fibers – such investigations are not further accounted for.

A further parameter (apart from those that have been mentioned within the argument above) plays a part when a choice for an optical fiber for a communication link is to be made: D_{PMD}, the coefficient of polarization mode dispersion (PMD). For light traveling along a birefringent fiber, PMD describes the difference in group velocity between the propagation along the fast and the slow axes of polarization. This difference leads to a differential group delay

$$\Delta\tau = D_{PMD}\sqrt{L} \tag{2.39}$$

with the fiber length L. It results in pulse broadening, limiting the transmission rate of an optical link [25]. As stated in section 1.3, a sensing length of 10 to 20 km is aimed at in the development of the sensing system. With $D_{PMD} = 0.2\ \text{ps}/\sqrt{\text{km}}$ specified as a maximum for individual Corning SMF-28e fibers [31], $\Delta\tau = 0.9$ ps for $L = 20$ km is calculated. In section 3.2, it will be shown that the measurement technique presented in this work bases on the detection of a sinusoidally modulated optical signal with modulation frequencies < 100 MHz, which corresponds to a minimum periodic length within the signal of $T = 10$ ns. With $\Delta\tau = 0.9$ ps after 20 km of fiber length, the cumulated phase error φ_{PMD} for the detection of the modulated signal becomes

$$\varphi_{PMD} = \frac{\Delta\tau \cdot 2\pi}{T} = 5.7 \cdot 10^{-4} \text{ rad} \tag{2.40}$$

Degradations in the phase detection, inherent to the measurement instrumentation, will be considered in sections 3.2.4 and 5.2.3. Their comparison to the estimation from (2.40) shows that the phenomenon of PMD can be fully neglected in the Brillouin frequency domain analysis.

Finally, it can be said that chromatic dispersion will not have any impact on the investigations presented here, since the laser sources operate very closely to the zero-dispersion wavelength of $\lambda_0 = 1313$ nm of the CORNING SMF-28e [31].

Laser characteristics relevant for SBS

Among the countless varieties of available laser sources – some of which have found their main applications in optical communications, others in material processing, metrology, medicine or innumerable other fields – the search for suitable sources for measurements on stimulated Brillouin scattering starts with examination of the following basic laser characteristics:

- **Wavelength:** In standard silica optical fibers, telecommunication systems usually employ two narrow bands in the near infrared spectrum: The bands at $\lambda = 1310$ nm, where chromatic dispersion is zero, and at $\lambda = 1550$ nm, where optical attenuation has its minimum (and erbium-doped fiber-optic amplifiers are available). For these bands, components such as photodetectors, modulators, couplers etc. are most commonly available.

- **Optical output power:** As the following sections will show, the power requirement for the excitation of stimulated Brillouin scattering primarily depends on the length of the optical fiber. When the two counterpropagating lasers are injected into the fiber ends, the aim is an interaction over the fiber length as steady as possible; with initial optical powers chosen too high, the pump beam will be depleted, and no scattering will occur towards the end of the fiber opposite to the pump injection. A pump power of 5 mW and a Stokes power of $50 \ldots 500$ μW have been found to be reliable initial conditions for measurements on fibers from around 100 m to 5 km [34].

- **Spectral linewidth $\Delta\lambda$:** With the Brillouin gain spectra being scanned by performing a sweep of the laser frequency offset Δf – and thereby shifting the frequency of the envelope of the beat pattern – the resolution of the measured gain spectra along the axis of Δf is limited by the spectral width of the laser sources. In standard fibers, the Brillouin linewidth is about 35 MHz. Therefore, a high spectral purity with $\Delta\lambda$ as small as possible is mandatory for adequate characterization of the gain spectra[2].

- **Tunable optical frequency:** The first task to be achieved when Brillouin gain spectra are to be measured is the adjustment of the frequency offset Δf between the pump and the Stokes laser. Obviously, this task requires at least one of the laser sources to be tunable in frequency by means of an electrical signal.

The laser sources that have been found suitable for the laboratory setup are two independent solid-state lasers with Nd:YAG as the gain medium (i.e., yttrium aluminum garnet being the host material for light-emitting Neodymium atoms as dopants). This medium is configured as a crystal ring oscillator, being pumped by a temperature-controlled semiconductor diode at 808.5 nm and emitting at $\lambda = 1319$ nm. The lasers provide high optical output power with an extremely high spectral purity; these characteristics, in comparison to those of semiconductor lasers, are summarized in table 2.1.

	P_{out}	$\Delta\lambda$	P_{diss}
DFB laser (standard telecom)	< 10 mW	> 1 MHz	500 mW
DFB laser (high performance)	< 100 mW	> 100 kHz	1.5 W
external cavity laser	< 10 mW	> 5 kHz	200 mW
Nd:YAG laser	150 mW	5 kHz	30 W

Table 2.1: Comparison of the characteristics of a typical telecommunication DFB laser and the Nd:YAG lasers that have been used for the SBS measurements: output power, linewidth and electrical power consumption.

Frequency tuning is achieved by altering the emission wavelength of the crystal resonator. This is done in two ways simultaneously: First, a peltier element acting as a thermo-electric cooler (TEC) is attached to the crystal; applying a voltage to this element allows tuning in a range of 30 GHz at a scanning rate of 1 GHz/s. Second, a piezoelectric element bonded onto the crystal can squeeze the resonator, which leads to fast frequency tuning (limited by the piezo's capacitance of about 10 nF) in a range of 30 MHz [35].

In order to perform sweeps of Δf, it is necessary to use both the thermal and the piezo tuning option. Details on the implementation of a stable laser control loop, designed to adjust and sweep Δf, are given in section 4.1.1.

The considerations above have been made with the premise of two independent laser sources to be employed in the measurement setup. This approach was followed throughout the experiments described in the thesis. The use of one single laser source

---

[2] The coherency length of the light sources is directly derived from their spectral width. This figure plays a role when considering passive polarization scrambling. In general, distributed measurements of SBS have been reported with lasers of comparably large linewidths, resulting in coherency lengths of a few meters; no constraints to intensity, linearity or resolvability of Brillouin interaction due to short coherency lengths have been found in literature.

(typically a DFB laser) from which the two required optical frequencies are drawn by means of amplitude modulation is a well-known method [36] and is employed in several commercially available devices for Brillouin sensing; it will be handled in section 4.1.2. This configuration is currently being implemented on the laboratory test bench at BAM. However, since the research was focused on signal acquisition and processing for spatially distributed measurements rather than on generation of the SBS excitation, the two Nd:YAG lasers, even if not the most efficient choice, served well for the purposes.

2.2 Measurement of SBS in silica optical fibers

2.2.1 Measurement of the Brillouin pump threshold

In telecommunication systems, stimulated Brillouin scattering puts a limit to the maximum power that can be transferred over a fiber optic link. It is observed that when light travels along the fiber, there is a certain power value, depending on the fiber length, from which backscattering increases drastically: This is the point where spontaneous scattering evolves into stimulated scattering; it is denoted as the Brillouin pump threshold P_{th}.

Brillouin pump threshold for a single laser

The determination of P_{th} for a single optical signal in a fiber is of minor importance for distributed measurements, in which counterpropagating light waves cause the excitation of SBS. However, since the measurement of P_{th} was the first experimental verification of the existence of stimulated Brillouin scattering performed in the lab at BAM, it is employed as a starting point to all successive experiments. The numerical estimations given in this section are adapted from literature [22], [34], starting with maximum Brillouin gain [22]

$$g_{Bmax} = \frac{2\pi n^7 p_{12}^2 \gamma_P}{c_0 \lambda_p^2 \rho_0 v_a \delta f_B} \tag{2.41}$$

with the following parameters:

n	1.4677	refractive index (Corning SMF-28e, $\lambda = 1310$ nm) [31]
p_{12}	0.2678	longitudinal elastooptic coefficient of silica [34]
γ_P	$^2/_3$	polarization factor [28]
λ_p	1319 nm	pump wave length
ρ_0	2201 kg/m^3	density of silica [22]
v_a	5960 m/s	sonic velocity in silica [22]
δf_B	35 MHz	FWHM of the Brillouin gain spectra [34]

The resulting g_{Bmax} has the dimension m/W and enters the estimation of the pump threshold [22]:

$$P_{th} \approx 21 \frac{A_{\text{eff}}}{g_{Bmax} L_{\text{eff}}} \tag{2.42}$$

with the effective core area $A_{\text{eff}} = \pi W^2$ (core diameter for Corning SMF-28e, $\lambda = 1310$ nm: $2W = 9.2\ \mu$m [31]) and the effective fiber length L_{eff}:

$$L_{\text{eff}} = \frac{1}{\alpha} \left(1 - e^{-\alpha L}\right) \tag{2.43}$$

Here, α is the damping coefficient of the fiber (for Corning SMF-28e, $\lambda = 1310$ nm: $\alpha = 0.03$ dB/km [31]).

In order to verify these estimations experimentally, light from an Nd:YAG laser is coupled into several fibers of different lengths; using a variable optical attenuator, the optical power injected into the fiber can be varied. Both the power transmitted through the fiber and the backscattered power are measured, the latter by means of a fused coupler inserted into the optical path (see figure 2.5).

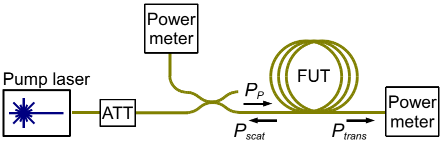

Figure 2.5: Setup for measurement of the Brillouin pump threshold with one laser source. FUT: fiber under test. ATT: variable precision attenuator.

Table 2.3 summarizes the results from the measurements on five standard single-mode fibers of different lengths; especially the longer fibers show excellent correspondence with the theoretically estimated values.

L [m]	α [dB/km]	L_{eff} [m]	$P_{th,est}$ [mW]	$P_{th,meas}$ [mW]
2250	0.328	2069.2	42.9	36
2260	0.322	2080.8	42.6	40
4460	0.342	3761.0	23.6	22
6430	0.336	5065.9	17.5	15
10540	0.334	7221.8	12.3	12

Table 2.3: Fiber parameters and theoretically estimated values ($P_{th,est}$) compared to measured values ($P_{th,meas}$) for the Brillouin pump threshold.

This first measurement of stimulated Brillouin scattering comprises the impressive result that virtually no increase of transmitted power through a fiber can be achieved by increasing the injected power. In figure 2.6, the measurement traces for the 2250 m long fiber and the 6430 m long fiber are plotted; it can be seen that for input power values higher than P_{th}, the output power goes into saturation.

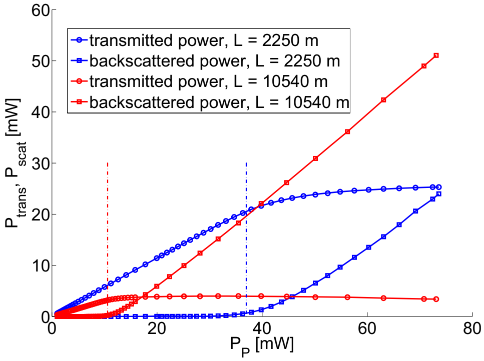

Figure 2.6: Transmitted and backscattered power measured at two fibers of different lengths. The vertical dashed lines indicate the theoretically estimated values for the Brillouin pump threshold.

Brillouin pump threshold: Two counterpropagating lasers

The characteristic dependence between injected optical power and Brillouin scattering – power being transmitted while remaining below P_{th}, then rapidly saturating – changes dramatically when a counterpropagating Stokes laser is injected from the opposite fiber end. This will not come as a surprise when taking the first considerations from section 2.1.1 into account: No threshold has to be reached by the pump beam, because right from the start of a power sweep a stimulated scattering process will occur.

This is of some importance for the following steps towards a distributed sensing system. Knowing that low power values are sufficient for stimulated scattering, the optical power can be adjusted on both sides to fulfill the following requirements: On the one hand, the injected power values must be strong enough to ensure measurable interaction, which strongly depends on the interaction lengths (in case of fibers of homogeneous strain and temperature, this is the entire fiber length). On the other hand, the effect of pump depletion must be avoided. This means that interaction has to be kept modest and as linear as possible; when the interaction enters the nonlinear region, pump power will be lost within a short section of the beginning of the fiber, so that the remaining fiber length will not contribute to the measurement.

Now there are five degrees of freedom that determine the intensity of Brillouin interaction to be measured: the fiber length, the power values of pump and Stokes laser, the frequency detuning Δf between the two lasers and their relative states of polarization. The latter two parameters are adjusted in order to maximize Brillouin gain, using the setup that is shown in figure 2.7. The polarization is empirically tuned to maximum interaction (achievable through coinciding polarizations, see section 2.1.3) by means of a four-axes-polarization controller.

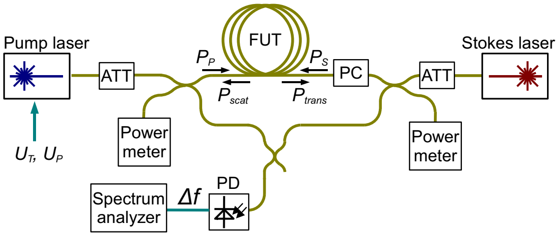

Figure 2.7: Setup for measurement of the Brillouin pump threshold with two counterpropagating lasers. PC: polarization controller; PD: photodetector.

For the tuning of Δf, both laser signals are superposed on a photodetector (25 GHz bandwidth); the resulting beat signal is monitored on a spectrum analyzer. By applying voltages to both the TEC element and the piezo actuator on the pump laser's crystal[3], Δf can be tuned manually. Since the lasers show quite a strong jitter and frequency drift, alert manual control is necessary in order to keep the deviation from the desired Δf value within the range of 1 MHz while reading out the power meters. At this point, the need for an automatic control of the frequency offset becomes evident (the implementation of which will be described in section 4.1.1).

The laser offset frequency at which maximum Brillouin gain is measured ($\Delta f = f_B$) is found to be at 12.79 GHz for the fiber material available in the lab (CORNING SMF-28e). This value, being the fiber's characteristic Brillouin frequency shift at room temperature and zero strain (if strain applied by storing the fiber on the coil is neglected), will remain an important number throughout all further research.

Results from the measurements on two fibers of different lengths are shown in figure 2.8. While the single-laser characteristic showed a sharp bend at P_{th}, for counterpropagating lasers no such threshold can be determined; the backscattered power shows a rather smooth increase towards higher input powers. With higher Stokes power P_s, the increase becomes steeper; the dependence on the fiber length remains valid.

These measurement data are not analytically evaluated; while setting up the system for distributed Brillouin measurements, it has shown that the optimum power values on both sides are to be figured out empirically. The absolute values for the maximum Brillouin gain are of minor importance in order to characterize the gain spectra. Adjusting the power levels only serves to avoid pump depletion and to retrieve a Stokes signal well above the noise floor. From these measurements, the starting

---

[3] The reason why the pump laser is chosen for application of the tuning voltages will be given in section 4.1.1

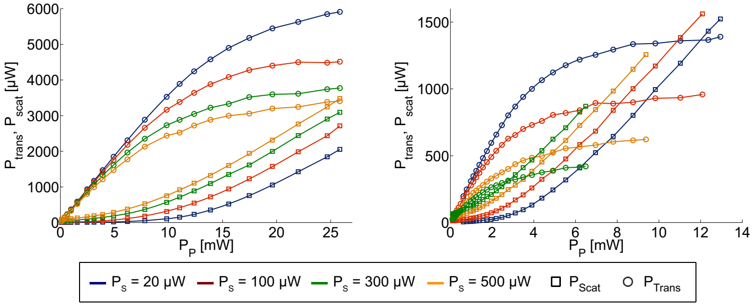

Figure 2.8: Transmitted and backscattered optical power with two counterpropagating lasers at different power values (polarization adjusted to maximum gain, $\Delta f = 12.79$ GHz). P_P and P_S denote the injected pump and Stokes power; P_{trans} is the transmitted pump power at the fiber end, while P_{scat} is the received Stokes light, amplified by stimulated Brillouin scattering, at the beginning of the fiber. *Left:* $L = 2250$ m. *Right:* $L = 10540$ m.

point $P_p = 5$ mW and $P_s = 100 \ldots 300$ μW are derived; for fibers with $L \leq 4500$ m, interaction occurs in a fairly linear region. These values provides good performance in distributed measurements for a large variety of fibers under test ($L = 100 \ldots 4000$ m).

2.2.2 Measurement of the Brillouin gain spectra

From the setup for measurement of the Brillouin interaction with two counterpropagating lasers (figure 2.7), it is a small step to the characterization of the Brillouin gain spectra, which show the dependence between the Stokes signal amplified by Brillouin gain and the frequency offset Δf. Thorough analyses of such measurements on Brillouin gain spectra can be found in literature [36]. In this section, gain spectrum measurements – being the last preliminary stage on the way to distributed Brillouin sensing – are briefly presented, because they provide a way for exact determination of the impact of strain and temperature on the Brillouin frequency shift f_B. From these data, the coefficients can be drawn that serve for calibration of all distributed measurements.

The laboratory setup is shown in figure 2.9: The manual tuning procedure for Δf remains unchanged[4], and so does the configuration for defining power levels and polarization states: Both the power and polarizations are adjusted for optimum interaction and remain fixed during the measurements. Linear sweeps are performed for Δf, temperature and strain.

---

[4] Actually, for the larger measurement series, automated control and sweep of Δf was employed. Nevertheless, since this control is one of the central parts of the setup for distributed measurements, it will be introduced in section 4.1.1.

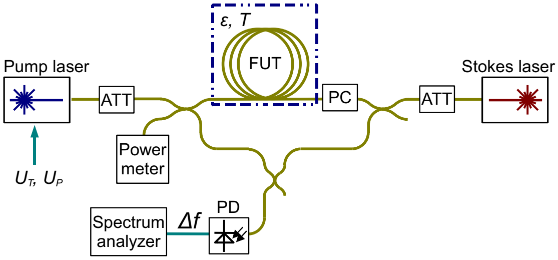

Figure 2.9: Laboratory setup for characterization of the Brillouin gain spectra

Brillouin gain spectra: Varying the temperature

Characteristic Brillouin gain spectra of a single-mode fiber ($L = 2250$ m) at different temperatures are shown in 2.10.

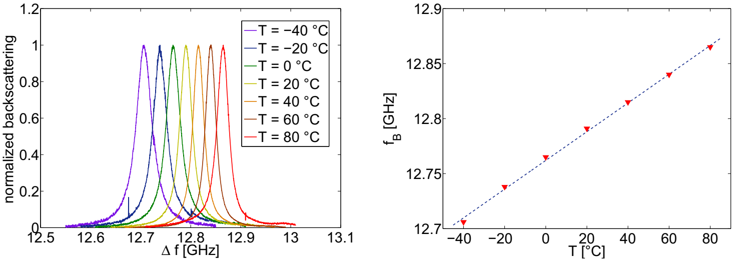

Figure 2.10: Dependence between the Brillouin frequency shift and the temperature. *Left:* Brillouin gain spectra. *Right:* Frequency of maximum Brillouin interaction versus temperature.

The measurement series were performed by placing the fiber under test inside a temperature chamber with a sweep range from -70 °C to 150 °C. For seven different temperature values, a sweep of Δf was performed and the Stokes power after interaction with the pump beam was recorded. The left-hand graph shows the Brillouin gain spectra, normalized to their maximum at $\Delta f = f_B$, thus polarization and temperature-specific attenuation are not accounted for. In the right-hand graph, the values of f_B for each temperature are given, showing a linear behavior with a slope of 1.3 MHz/°C.

Brillouin gain spectra: Applying strain

In contrast to the variation of temperature – which is easily achieved with a temperature chamber for an entire fiber coil – application of defined longitudinal strain requires more technical effort. When the design of an apparatus to elongate a fiber to the desired strain value was initiated, the evaluation of distributed measurements was already the main objective. Therefore, a profile of various sections of different strain values was to be applied to one fiber, each of the sections being firmly fixed for long-term measurements.

Starting the design from scratch, two feasible ways to stretch a fiber can be easily thought of: Either the fiber is fixed at two points and the distance is increased mechanically, or a section of fiber is loaded with a defined weight. The first approach shows several disadvantages at a closer look: Inaccuracies impacting the actually applied strain are induced at the fixation points due to frictional losses in case of gluing or clamping; increased optical attenuation at these points is impossible to avoid. Furthermore, the length of the strained section is limited by the geometry of the setup. Longer sections of strained fiber can be achieved by using fiber coils that are pulled apart [34], accepting strong inhomogeneities of strain along the section under test.

The second approach – loading the fiber by a weight – led to the design of the apparatus that was finally realized in the division's scientific workshop at BAM. A drawing as well as a photograph are shown in figure 2.11.

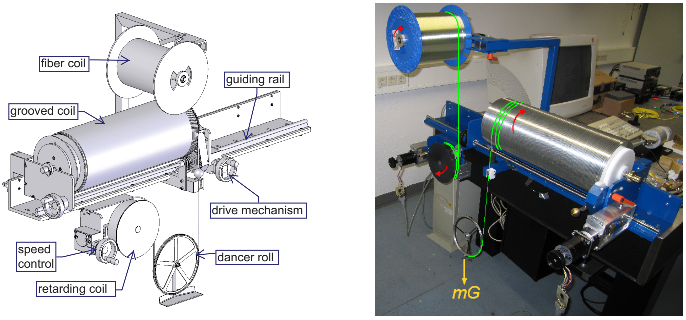

Figure 2.11: The apparatus that was developed to apply defined strain values to optical fibers.

Its central element is a dancer roll floating in mid-air, which applies strain to a fiber that is drawn from the manufacturer's coil. The pre-strained fiber is rolled up on a coil with a helical groove covering its entire surface: The groove provides maximum friction, thereby preserving the strain of the fiber.

The dancer roll can be loaded with a wide range of weights, thereby defining the actual strain value (being the relative elongation ε) applied to the fiber:

$$\varepsilon = \frac{\Delta l}{l} = \frac{m \cdot g}{2A \cdot \beta} \tag{2.44}$$

Here, A is the cross-sectional area of the fiber, β is Young's modulus of elasticity, m is the mass of the load on the dancer roll, and g is the gravitational constant. The fiber is pulled from the coil of origin via an additional spool to retard the unwinding and controlling its speed, so that the fiber section that is pre-strained by the dancer roll is relieved from the forces that are needed to move the original coil. Both the retarding coil and the grooved coil are rotated by independently controlled step motors. The speed of the motors is adjusted to keep the dancer roll floating at a constant height (otherwise, (2.44) loses validity).

The apparatus distinguishes itself from previous approaches to apply defined strain values to optical fibers by the following characteristics:

- Reliable calibration is achievable because the only material parameter entering the calculation of strain from the applied force is the elastic modulus. Since the dancer roll is designed to minimize frictional forces and friction on the aluminum coil is maximized by the grooved surface, inaccuracies are minimized. In preliminary mechanical tests, the fiber's characteristic $d\varepsilon/dm$ was determined to be 9.759 $\mu\varepsilon$/g.

- By changing the mechanical load on the dancer roll, various sections of different strain values can be stringed together; the minimum possible strain value is given by the mass of the dancer roll (aside from zero strain, which can be reliably achieved by manually feeding the grooved coil).

- The total length of the groove for uncoated fiber is about 250 m, allowing the generation of complex and extended strain profiles. A second grooved coil for larger diameters – accepting coated fibers up to 3 mm of diameter – was produced, allowing a total length of 80 m.

For measurement of the Brillouin gain spectra, one constant load was applied to the dancer roll for each sweep of Δf, providing a fiber with $L = 70$ m of constant strain over its entire length. (The full potential of the apparatus – the generation of a defined profile with various sections of different strain values – is employed and demonstrated in section 4.4.)

Four different strain values were applied to the fiber; the measurement results are shown in figure 2.12, showing the normalized Brillouin gain spectra of an unstrained fiber together with the strained fibers as well as the linear dependence between strain and f_B with a slope of 61.4 MHz/1000 $\mu\varepsilon$.

Summarizing the results of the measurements on Brillouin gain spectra, there are four figures to be drawn from the data that will play a significant part in the following chapters: The natural Brillouin frequency shift and the corresponding spectral

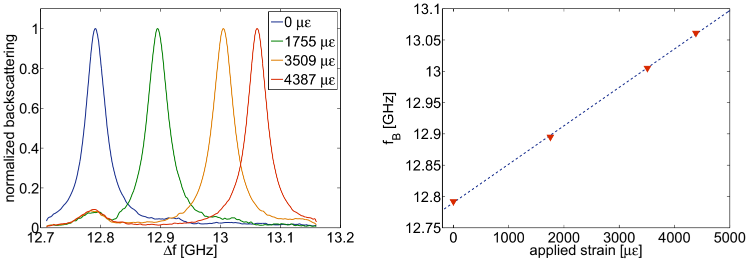

Figure 2.12: Dependence between Brillouin frequency shift and longitudinal strain, measured in homogeneously strained fibers. *Left:* Brillouin gain spectra. *Right:* Frequency of maximum Brillouin interaction versus strain.

linewidth (both for Corning SMF-28e standard single-mode fibers, $\lambda = 1319$ nm)

$$\left.\begin{aligned} f_B = &\quad 12.79 \text{ GHz} \\ \delta f_B = &\quad 33 \text{ MHz} \end{aligned}\right\} \qquad \text{for } T = 20\ ^\circ\text{C and } \varepsilon = 0$$

and the coefficients of the change of the Brillouin shift with temperature and longitudinal strain:

$$\begin{aligned} \frac{df_B}{dT} &= 1.3 \text{ MHz/K} \\ \frac{df_B}{d\varepsilon} &= 61.4 \text{ MHz}/1000\ \mu\varepsilon \end{aligned}$$

In literature, several reports of measurements on the temperature and strain coefficients for f_B can be found. The comparison allows to conclude a good agreement between the above coefficients and previously reported values: For df_B/dT at $\lambda = 1320$ nm, 1.33 MHz/K [37] and 1.18 MHz/K [34]; for $df_B/d\varepsilon$, 56.3 MHz/$\mu\varepsilon$ [38] and 50.1 MHz/$\mu\varepsilon$ [34] (due to the strong dependence of the coefficients on the composition of the fiber material, no perfect match between measurements on standard optical fibers with almost 20 years between the investigations can be expected).

An important insight gained these data is the domination of the strain impact on f_B over the temperature impact. Considering quantities that can be expected in real-life applications such as geotechnical monitoring, a change of f_B that corresponds to the impact of 100 $\mu\varepsilon$ in the sensing fiber can be considered as the minimum value to be detected in such a system (see chapter 7); this change in f_B corresponds to a temperature shift of 4.3 °C. Especially in a large-scale monitoring system buried into the soil, such strong local temperature gradients are not to be expected; when slow global temperature changes (such as periodic day-time influences) can be deducted, it is a valid assumption that the sensing fiber can be operated as a strain sensor, while temperature as a disturbance variable can be neglected.

CHAPTER 3

Distributed measurement of optical backscattering

The characterization of the Brillouin gain spectra in section 2.2.2 shows the potential of stimulated Brillouin scattering to serve for measurement purposes: The linear dependence between f_B – the frequency offset between two counterpropagating lasers where maximum interaction occurs – and both strain and temperature of a fiber under test, make the phenomenon a straight-forward candidate to become the core of a measurement device. Still, on the way to a sensing system suitable for applications in structural health monitoring, there is one crucial information missing: For monitoring of a dike, it is not sufficient to know when and how strong a local change in strain is occurring – the question is, where exactly the fiber section affected by the change is located along a sensing length of several kilometers.

Several approaches have been investigated in order to retrieve a spatially resolved profile of Brillouin interaction along an optical fiber, two of which will be presented here: The oldest and most common technique is the pulse reflectometry or Brillouin optical time domain analysis (BOTDA), that will be presented first, because its understanding provides the basis for the second technique, which is the one that was employed and significantly advanced within the work on this thesis: the Brillouin optical frequency domain analysis (BOFDA).

Both techniques base on a sweep of the laser frequency offset Δf in order to scan the Brillouin gain spectrum $g_B(\Delta f)$ of a fiber, and both techniques yield a spatially resolved profile of Brillouin interaction along the fiber for each value of Δf as their result. A complete distributed measurement of stimulated Brillouin scattering is then constructed by aligning all spatially resolved traces from the sweep of Δf along the spatial dimension z. Obviously, such a measurement will result in three-dimensional data, with the sweep of Δf, the fiber length $z = 0 \ldots L$ and the intensity of SBS (or the Brillouin gain experienced by the Stokes beam) forming the axes.

Therefore, the retrieving of the spatially resolved information will be investigated independently from the physical nature of stimulated Brillouin scattering: The system description of a single spatially resolved measurement for a fixed Δf is (almost) sufficient to understand the overall system, with the presumption that all analyses from chapter 2 hold true when the described techniques are applied. As a matter of fact, this is not entirely the case, resulting in some undesired phenomena which the complete chapter 6 is dedicated to.

3.1 Measurement in the time domain

Pulse reflectometry measurements are not exclusively linked to Brillouin sensing; they are standard procedure in fault location and distributed attenuation measurement in optical fibers (to be precise, the technique is far older than all fiber optics and has numerous classical applications, among them being radar devices and fault location on electrical lines). The principle of time domain measurements in optical fibers is shown in figure 3.1; this scheme might be found in OTDR devices for attenuation measurements[1] as well as distributed Raman or Brillouin sensing systems.

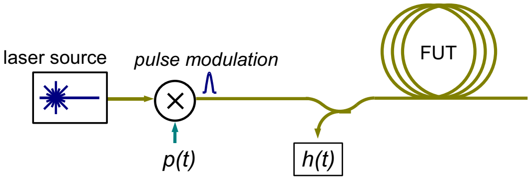

Figure 3.1: Basic principle of the optical time domain analysis.

An optical pulse is generated (in this depiction, by external modulation of a laser source with a pulse signal $p(t)$) and injected into the fiber under test. While traveling along the fiber, it will encounter spots of partial or total reflection (faults or cracks in the fiber or its end face); thus, portions of the injected light will be sent back from these spots to the origin, where they can be coupled out to be monitored. By plotting the intensity of the received light over its time of arrival, the temporal pulse response of the system $h(t)$ is recorded. Thus, a distributed profile of the reflections $h(z)$ can be generated, since reallocation of the time of arrival to the location where reflection

---

[1] OTDR – optical time domain reflectometer – is the common denomination for measurement devices that use pulse reflectometry for fault location and attenuation measurements in optical fibers. Although the technique itself is basis to many more concepts of optical measurement, in the following, the term OTDR will refer to only these special measurement devices.

occurred follows the simple relation

$$z_s = \frac{1}{2}\frac{c_0}{n}t \tag{3.1}$$

with vacuum light speed c_0 and the fiber's refractive index n. At $t = 0$, the pulse is launched. It is then traveling with the velocity c_0/n. The distance covered by the received signal is twice the distance between the origin at $z = 0$ and the location of the reflective event at $z = z_s$, hence the division by 2 [25].

In addition to the local events that cause the pulse to be reflected from discrete spots, portions of its power will be continuously sent back to its origin while traveling along due to the various linear and nonlinear backscattering mechanisms. In OTDR devices, it is Rayleigh scattering which produces the spatially distributed trace of optical losses along a fiber.

To adapt this method to the measurement of stimulated Brillouin scattering, the pulse is launched while a counterpropagating (continuous-wave) Stokes beam is present in the fiber under test. If the frequency offset Δf between the pulse (now being the pump signal) and the Stokes beam lies within the Brillouin linewidth δf_B around f_B, the traveling pulse will be involved in stimulated Brillouin interaction: a portion of the pulse power will be transferred to the Stokes beam, which again can be monitored over time, yielding the spatially resolved profile of Brillouin gain at the given frequency offset Δf. If now Δf is tuned, a three-dimensional measurement trace over z and Δf is recorded that represents the local distribution of the Brillouin gain spectra along the fiber. This technique for spatially resolved measurements of Brillouin gain is known as Brillouin optical time domain analysis (BOTDA).

All commercially available systems for distributed Brillouin sensing base on this principle of pulse measurements. Several variations on the basic concept from figure 3.1 have been reported and implemented:

- Instead of pulse modulation of the pump laser, the Stokes laser can be pulsed, then interacting with a continuous-wave pump beam. In this configuration, it is the Brillouin loss (the diminution of the CW pump power) that is recorded over time and the sweep of Δf [39].

- When both the pump and the Stokes signal are generated from a single laser source (this technique will be described in section 4.1.2), it is possible to inject both signals as subsequent pulses into the fiber: The first pulse might have the optical frequency of the pump light; the output frequency of the laser source is altered (see section 4.1.2) to the Stokes frequency and the second pulse is launched. In such a setup, the opposite fiber end has a highly reflective end face; the two pulses will then meet and interact only at a short fiber section the location of which is determined by the delay between the injection of the pump and the Stokes pulse. This configuration yields the advantage that access to only one fiber end is required [40]; on the downside, degradation of the dynamic range has to be accepted.

- Even with no counterpropagating beam present in the fiber, Brillouin gain spectra can be measured. The light that can be received from the self-induced stimulated backscattering process[2] is spectrally analyzed and f_B for each position along the fiber is extracted; this approach is known as Brillouin optical time domain reflectometry (BOTDR). In such a setup, even separation of temperature and strain by means of analysis of the shape of the gain spectra has been reported [41]. The acquisition of a spatially resolved trace of reasonable dynamic range from the relatively weak self-induced scattering process requires a far more complex recording procedure than the data acquisition from counterpropagating signals.

In section 1.3, the four parameters that define the performance of a distributed sensing system were introduced: Measurement length z_{max}, spatial resolution δz, resolution of the measurand (precision of f_B, to be transferred into strain or temperature) and time for data acquisition (measurement speed). The latter strongly depends on the technological implementation and can be adjusted at the cost of dynamic range, which in turn will affect the measurand resolution. This parameter is governed by the accuracy of the determination of the Brillouin gain spectra (the measurement along the Δf axis) and is therefore not inherent to the system description of pulse reflectometry (which accounts for the trace along the z axis).

The remaining two parameters, z_{max} and δz, can be drawn directly and analytically from the system description of pulse reflectometry. The spatial resolution is determined by the width of the optical pulse which is launched into the fiber: The shape of any measured event will be constructed from a convolution of the actual shape of the event with the pulse form, introducing a spatial blur into the measurement. Presuming a rectangular pulse of a width Δt_p, spatial resolution becomes

$$\delta z = \frac{1}{2}\frac{c_0}{n}\Delta t_p \tag{3.2}$$

if Δt_p remains constant over the fiber length[3]. For gaussian-shaped pulses, Δt_p is the full width at half maximum (FWHM) of the pulse; δz then denotes the FWHM of the response of a discrete event with no spatial dimension (e.g. a Fresnel reflection). With this, a pulse width $\Delta t_p = 10$ ns gives a spatial resolution of 1 m [39], which is provided by commercially available Brillouin sensing systems by the time of writing [12].

The maximum measurement length is theoretically determined by the repetition rate of the pulses, since from the launching of a pulse, twice the time the pulse needs for the whole fiber length has to elapse before the next pulse might be launched. In praxis, z_{max} is limited by the attenuation of the fiber; depending on methods used for averaging and signal restoration, an accumulated attenuation of 20 dB along the

---

[2] In literature, the process behind this technique is often referred to as spontaneous Brillouin scattering. The denomination of this process as stimulated Brillouin scattering is in accordance to the definition of stimulated and spontaneous backscattering in section 2.1.1.

[3] In section 2.1.4, it was shown that modal, chromatic and polarization mode dispersion are no issues for silica optical fiber sensors. Yet, pulse broadening due to these effects becomes critical in POF sensing [42].

fiber represents a maximum in optical budget for commercially available systems [12]. On bare fiber coils in the lab, this corresponds to a measurement length of more than 50 km. In field applications, this number usually decreases dramatically, since fibers can hardly be applied to any structure without accepting additional losses.

3.2 Measurement in the frequency domain

3.2.1 Theoretical basics

From a system point of view, the measurement result obtained from an ideal pulse reflectometry measurement (using dirac pulses with $\Delta t_p = 0$) is the optical fiber's temporal pulse response $h(t)$, which is then transferred into the spatial domain by equation (3.1). A system's pulse response can be transferred into the system's transfer function $H(j\omega)$ and vice versa by a Fourier transform, with the prerequisite on the system to be linear and time invariant:

$$H\left(j\omega\right) = \int\limits_{-\infty}^{+\infty} h(t) e^{-j\omega t} dt \tag{3.3}$$

The system in question is the optical fiber with its characteristic Brillouin gain, varying with the variables Δf and z. Its input is the pump signal, the output is the received Stokes light, amplified by stimulated Brillouin scattering.

With the presumption that the measured Brillouin interaction between the two injected light waves is linear and time invariant (which will be discussed in section 3.2.4), a spatially resolved measurement of Brillouin gain along the fiber can be performed as follows: The system is excited at a variable frequency f_m. This is achieved by an amplitude modulation of either the pump or the Stokes light with f_m as the modulation frequency, the other light beam enters the opposite fiber end as a continuous wave, the two signals being spaced by the defined frequency offset Δf.

For the complete measurement, both Δf and f_m are varied, with a sweep of f_m for each value of Δf. The system's response to the excitation is measured and compared to the original modulation signal in amplitude and phase, giving the transfer function $H\left(j\omega, \Delta f\right)$, which is then transferred into the time domain by means of an inverse Fourier transform, yielding the pulse response $h(t, \Delta f)$. The pulse response is finally converted into the desired spatially resolved gain profile $h(z, \Delta f)$ by applying equation (3.1):

$$H\left(j\omega, \Delta f\right) \quad \bullet\!\!-\!\!\circ \quad h(t, \Delta f) \quad \xrightarrow{z=\frac{1}{2}\frac{c}{n}t} \quad h(z, \Delta f)$$

Again, this method was introduced long before Brillouin sensing and has been used in radar applications [43]; its application in optical measurements was proposed with the optical frequency domain reflectometry (OFDR) for fault location [44]. Consequently, the technique described here is called Brillouin optical frequency domain analysis (BOFDA).

Figure 3.2 shows the general principle of such a frequency domain measurement: The sinusoidal modulation of the injected light replaces the pulse modulation in time domain measurements. Due to reflective events or backscattering, the received signal will also be modulated. This modulation of the received signal is compared in amplitude and phase to the original modulation signal; by sweeping f_m, the complex transfer function $H(j\omega)$ is obtained.

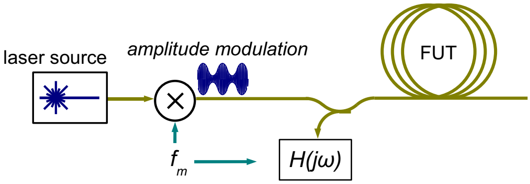

Figure 3.2: Basic principle of the optical frequency domain analysis.

In the case of Brillouin sensing, the system's response is represented either by the gain of the Stokes light or the loss within the pump light. The first applies to a configuration with the pump signal being modulated, the second corresponds to the modulation of the Stokes wave. In both configurations, the originally continuous wave, that is injected at the fiber end opposite to the entering point of the modulated signal, will adopt the amplitude modulation at the same frequency f_m as the excitation, bearing the information on the system behavior in the relative magnitude and phase.

Within this work, only the configuration with a modulated pump light is investigated, because it comprises optical signals far easier detectable (i.e., the gain of the comparably weak Stokes signal) than those in the configuration of a modulated Stokes light (the periodical diminishing of the intense pump light).

The following system analysis of optical frequency domain measurements is not restricted to the special case of Brillouin sensing; therefore, the sweep parameter Δf will not appear in the considerations. The analysis is valid for discrete reflective events as well as continuous backscattering (for stimulated Brillouin scattering, the analysis applies to a frequency domain measurement at a fixed Δf, and thus, constant Brillouin gain at each spatial location along the fiber). This independent analysis of Δf and f_m is valid for the presumption of $f_m \ll \delta f_B$, a constraint that will be discussed in chapter 6.

Ideally, a system's complex transfer function $H(j\omega)$ is an analytical continuous expression which provides the frequency response of the system over an infinite frequency range. In a practically implemented measurement, two constraints have to be accepted: First, the measurement of $H(j\omega)$ is performed at discrete frequency points $f_m = \omega_m/2\pi$, equally spaced by an increment $df = d\omega/2\pi$. The result is the discretized transfer function

$$H_d\left(j\omega\right) = \sum_{k=-\infty}^{+\infty} H\left(j \cdot k \cdot d\omega\right) \cdot \delta\left(j\left(\omega - k \cdot d\omega\right)\right) \tag{3.4}$$

in which the sifting property of a Dirac delta function δ is used. Since a discrete function in the frequency domain corresponds to a periodic signal in the time domain, the inverse Fourier transform yields

$$h_p(t) = \frac{1}{2\pi} \int_{-\infty}^{+\infty} H_d\left(j\omega\right) e^{j\omega t} d\omega = T \cdot \sum_{m=-\infty}^{+\infty} h(t - m \cdot T) \tag{3.5}$$

in which $h_p(t)$ is periodic with $T = 1/df$ [45]. If aliasing (i.e. the overlapping of the several instances of $h(t)$ within $h_p(t)$) is to be avoided, T must be larger than the temporal duration of $h(t)$. For an optical measurement, this means that the length of the fiber that can be measured is determined by the frequency increment df:

$$z_{max} = \frac{1}{2} \frac{c_0}{n} \frac{1}{df} \tag{3.6}$$

Therefore, df corresponds to the pulse repetition rate in time domain analyses [34].

The second constraint that is owed to the practical implementation is the limitation of f_m to a frequency band of a finite width between the boundaries f_{min} and f_{max}. For a discrete reflective event with no spatial expansion at $z = z_1$, an ideal measurement of infinite bandwidth would record a transfer function

$$H(j\omega) = A_1 e^{-j\omega\tau_1} \tag{3.7}$$

with A_1 being the amplitude degradation due to optical attenuation and $\tau_1 = z_1 n / c_0$ being the delay from $z = 0$ to $z = z_1$. The inverse Fourier transform will give the desired pulse response:

$$h(t) = \frac{A_1}{2\pi} \int_{-\infty}^{+\infty} e^{-j\omega\tau_1} e^{j\omega t} d\omega = A_1 \delta(t - \tau_1) \tag{3.8}$$

The ideal measurement results in a delta pulse shifted along the t axis by τ_1; after transformation into the spatial domain according to (3.1), the infinitely narrow peak will be located at z_1.

The scan of $H\left(j\omega\right)$ shall now be performed with a limited bandwidth of f_m. If $f_{min} = df$, the frequency range can be considered as a low-pass filtering of the transfer function[4]. A real-valued pulse response has a transfer function with a conjugated symmetry:

$$H\left(j\omega\right) = H^*\left(-j\omega\right) \qquad \text{for} \quad \mathrm{Im}(h(t)) = 0 \tag{3.9}$$

---

[4] The problem of the missing value for $f_m = 0$ will be discussed in section 3.2.4.

Thus, the transfer function is known from $-f_{max}$ to $+f_{max}$. In this case, the inverse Fourier transform will give

$$\begin{aligned} h(t) &= \frac{A_1}{2\pi} \int\limits_{-2\pi f_{max}}^{+2\pi f_{max}} e^{-j\omega\tau_1} e^{j\omega t} d\omega \\ &= 2A_1 f_{max} \cdot \mathrm{si}\big(2\pi f_{max}\,(t-\tau_1)\big) \end{aligned} \tag{3.10}$$

in which the si-function $\mathrm{si}(x) = \frac{\sin x}{x}$ determines the shape of the measured response for the event location. After transferring the pulse response into the spatial domain, the width of the si-shaped peak at z_1 represents a spatial uncertainty, which introduces a degradation of spatial resolution compared to the ideal delta response. The spatial resolution thus becomes

$$\delta z = \frac{1}{2} \frac{c_0}{n} \frac{1}{f_{max}} \tag{3.11}$$

which shows, when compared to equation (3.2), that f_{max} in frequency domain measurements is the equivalent to the pulse width Δt_p in pulse reflectometry. The scanning range of the transfer function directly corresponds to the spectral bandwidth of the optical pulses: Higher spatial resolution requires narrow pulses (with a larger bandwidth) in time domain measurements and a larger bandwidth for f_m in frequency domain measurements.

3.2.2 Motivation and history

The frequency domain technique for distributed measurement of optical backscattering was first proposed in 1986 by Ghafoori-Shiraz *et al.* [44] to measure linear scattering and reflections along an optical fiber[5]. The approach was adapted for Brillouin sensing by Krebber, Gogolla, Garus *et al.* [47]. Within their research, a laboratory setup yielding a 1 m spatial resolution [34], a numerical model of the stimulated scattering process, methods for spatial resolution enhancement such as frequency domain and spatial windowing [48] and a technique for beat length measurements in single-mode fibers [30] were developed and presented. The method was further advanced when Bernini *et al.* proposed a novel algorithm to retrieve the spatially resolved Brillouin gain profile from a frequency domain measurement by employing an accurate modeling of the Brillouin scattering process [49], which will be briefly discussed in section 3.2.4.

The main objectives for measurement in the frequency domain (and thereby leaving the well-established and proven path of pulse reflectometry) are the following:

1. A method was demanded that would overcome the need for elaborate high-speed electronics – for generation and transient recording of nanosecond pulses – which

---

[5] Frequency domain measurements of linear scattering have hardly been pursued in the past 20 years. Recently, new approaches to dynamic sensing using the measurements of discrete reflections in the frequency domain have been presented [46].

makes any time domain measurement system delicate, complex and expensive. The idea of a pulse response measurement via the transfer function can be seen as splitting the probe pulse into its spectral components, each of which is to be measured separately. These components are single-frequency harmonic signals within a range that is easy to handle (10 kHz. . . 100 MHz); thus, the perspective of a significantly simplified setup – aiming at competitive measurement results – is provided by the technical implementation of the frequency domain approach.

2. A crucial problem of pulse reflectometry that called for an alternative is the large measurement bandwidth required from the generation and capture of narrow optical pulses. Since the signal-to-noise ratio is inversely proportional to the measurement bandwidth of a system, this requirement on the components induces a limit to dynamic performance in time domain measurements. Again, the potential to approach this problem with frequency domain measurements becomes clear when the recording of the transfer function is seen as a separate recording of the spectral components of the probe pulse. Measurement bandwidth can be minimized by a narrow bandpass filter around the exact modulation frequency f_m, being the only frequency component of the received optical signal which contains information. While time domain measurements have to rely on the averaging over multiple backscattering traces from periodically launched pulses, a single frequency domain measurement can obtain a trace of identical dynamic performance. All parameters of the two systems – dynamic range, resolution and time for data acquisition – will remain equivalent due to the time-frequency duality in system theory, while an implementation advantage of the BOFDA system is achieved by significantly lowering the demands on the components.

3. A measurement of the Brillouin gain that is initiated by a traveling pulse has to rely on a high contrast within the pump signal between the on-state and the off-state of the pulse; if light of the pump frequency is present in the fiber before or after the pulse, Brillouin interaction will occur that can not be reallocated to its origin along the fiber. This leads to non-local effects along the spatially resolved trace [50]. In frequency domain measurements, all information on the spatially resolved gain profile is contained in the spectral band of the modulation frequency f_m of the received signal. Thus, filtering around f_m eliminates all non-local information, and the problem of contrast does not arise.

The theoretical concept of frequency domain measurements has been put into action by measuring the transfer function with a bench top vector network analyzer (VNA), as it was standard procedure in all previous BOFDA setups ([34], [49]). One of the major goals of this research was the development of a tailored hardware for the task of recording $H(j\omega)$; here, special benefit from the perspective of a narrow-band measurement of harmonic signals could be drawn. State-of-the-art digital electronics (especially analog-to-digital converters and digital signal processors) can easily handle the frequency band in question: This opens the way to a transfer of all signal processing electronics into the digital world. A complete demonstrator setup for digital Brillouin frequency domain analysis was developed and is presented in chapter 5.

These advantages of the frequency domain approach were the original motivation for its development. In addition, the separate recording of the spectral components of the pulse response have been found to enable a new approach to the problem of signal degradation at high spatial resolutions (where $f_B \ll \delta f_B$ is no longer valid). This phenomenon and the BOFDA-specific solution proposal are discussed in chapter 6.

3.2.3 Linearity and time invariance of the system

The central idea of the frequency domain analysis is the equivalence of the system's pulse response and transfer function. The main prerequisites for this equivalence are time invariance and linearity of the system; thus, the compliance of these demands in the case of Brillouin sensing are considered in the following.

The measurement of the complex transfer function $H\left(j\omega\right)$ has to be performed under complete steady-state conditions of Brillouin interaction for each sweep value of both f_m and Δf: Unlike in time domain measurements, steady state is provided during the recording of the system's response to the excitation, being a periodically modulated signal (i.e. the pump signal) of practically infinite duration. The condition to reach steady state (and thus, for time invariance of the system of which the transfer function is to be recorded) at the remote fiber ends, a delay of the total time of flight from $z = 0$ to $z = L$ (thus $\Delta t = L \cdot n/c_0$, being 5 μs/km) must be accounted for (from the moment of setting Δf and f_m). Then, the full-length interaction of pump and Stokes will have formed, providing the steady beat pattern to excite the acoustic wave.

For the amplitude ρ of the acoustic wave, the transient change of its excitation at $t = t_0$ forces its step response, being a perturbation in equation (2.19). This transient behavior has been modeled by means of a solution for a simplified formulation of equation (2.19) [51]. In this, the step response of the acoustic wave to follow its excitation by the superposing electric field amplitudes E_p and E_s (see section 2.1.2) is governed by the phonon damping rate Γ:

$$\rho(t) = \rho\left|_{t_0} + \left(\frac{E_p E_s^*}{\Gamma} - \rho\right|_{t_0}\right)\left(1 - e^{-\Gamma t}\right) \tag{3.12}$$

where Γ is $2\pi\delta f_B \approx 0.2 \cdot 10^9\ s^{-1}$ in silica fibers. Commonly, steady state is assumed when the step response reaches 90% of its final amplitude. The maximum delay (for the case of $\rho\left|_{t_0}\right. = 0$) becomes $\ln(0.1)/-\Gamma \approx 10$ ns. Consequently, the delay of the transient acoustic wave to reach steady state is of no consequence when added to the required time of flight with 5 μs/km.

A second requirement for time invariance of the sensing fiber is trivial: Within the time period that is needed for data acquisition, no change of the Brillouin gain distribution is supposed to occur. This requirement puts a hard constraint to considerations regarding strain measurement in dynamic structures with the Brillouin optical frequency domain analysis.

The demand for linearity of the measurement system for Brillouin optical time domain analysis can be formulated as follows: If two independent, subsequent measurements are taken with a pump signal, modulated with a frequency f_m (at an arbitrary, but constant value Δf_0 for the frequency offset Δf) and a counterpropagating cw Stokes signal, the signals that enter the system as an input (being the modulation signal for the pump light) for the two measurements are

$$\begin{aligned} u_{in1}(t) &= \hat{u}_{in1} \cos(2\pi f_m t) \\ u_{in2}(t) &= \hat{u}_{in2} \cos(2\pi f_m t) \end{aligned} \tag{3.13}$$

and the signals that are received at the system's output (being the Stokes light after Brillouin interaction) are

$$\begin{aligned} u_{out1}(t) &= \hat{u}_{out1} \cos(2\pi f_m t + \varphi_1) \\ u_{out2}(t) &= \hat{u}_{out2} \cos(2\pi f_m t + \varphi_2) \end{aligned} \tag{3.14}$$

with amplitudes $\hat{u}_{in1}$, $\hat{u}_{in2}$ of the input signals (input phases set zero) and amplitudes $\hat{u}_{out1}$, $\hat{u}_{out2}$ and phases φ_1, φ_2 of the output signals. A linear system with the transfer function $H(j\omega, \Delta f)$ would fulfill the relations

$$\begin{aligned} u_{out1} &= H(j2\pi f_m, \Delta f_0) \cdot u_{in1} \\ u_{out2} &= H(j2\pi f_m, \Delta f_0) \cdot u_{in2} \\ u_{out1} + u_{out2} &= H(j2\pi f_m, \Delta f_0) \cdot (u_{in1} + u_{in2}) \end{aligned} \tag{3.15}$$

The prerequisite of linearity might appear paradox in a system that is founded on a nonlinear optical effect. The power-dependent behavior of Brillouin interaction in a fiber with two counterpropagating lasers was shown in figure 2.8. It showed that the assumption of linearity is only valid up to power values far below the beginning of spontaneous scattering ($P_p < 5$ mW, $P_s < 300$ μW for $L = 2000$ m).

A method to estimate linearity is the monitoring of harmonics when the system is excited with a single-frequency signal. This was done with the setup from figure 3.2 with Δf set to maximum interaction for a 2250 m fiber. The measurement at two different modulation frequencies with varying pump and Stokes power is shown in figure 3.3. The fundamental as well as the first and second harmonic were measured with a photodetector and an electrical spectrum analyzer.

If strong nonlinearities dominated the system's response to the input signals of this experiment, a steep rise of the second harmonic together with a saturation behavior of the fundamental would be expected. In these measurements, this is not the case; strong nonlinear behavior that would question the frequency domain approach is not observed.

However, entire linearity of the overall system is by no means provided. Apart from Brillouin interaction itself, a number of components with nonlinear behavior –

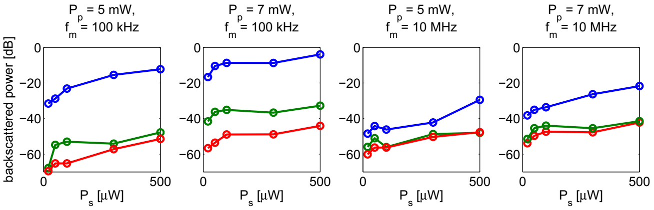

Figure 3.3: Measurement of fundamental (*blue*), second (*green*) and third (*red*) harmonics of Brillouin gain with single-frequency excitation.

such as the electro-optical modulator and photodiodes (the full setup will be presented in chapter 4) – contribute to the measurement of the transfer function $H(j\omega, \Delta f)$. Equations (3.15) can be considered as sufficiently valid for the system to perform measurements of competitive quality (which are presented in chapters 4 and 7), as long as the crucial parameters (optical power of the injected signals, drive voltage of the electro-optic modulators etc.) are kept within the boundaries of linearity. Still, the reconstruction of the pulse response $h(t, \Delta f)$ from $H(j\omega, \Delta f)$ will never be more than a good estimate. Any violation of (3.15) due to nonlinearities must be seen as a degradation of the measurement, adding an error term to the measured $H(j\omega, \Delta f)$. The impact of such a faulty measurement of $H(j\omega, \Delta f)$ on the resulting pulse response $h(t, \Delta f)$ after inverse Fourier transform will be analyzed in the next section (page 48).

3.2.4 Implementation issues

Based on the principal considerations above, this section discusses the main issues that have to be handled on the way to an implementation of the Brillouin frequency domain analysis. The actual laboratory setup will be discussed in chapters 4 and 5. Those two chapters will base on the considerations given here, and, in turn, will contain the measurement results that illustrate this discussion.

Highest frequencies

The bandwidth limitation of the transfer function in (3.10) represents an ideal (i.e., infinitely steep) low-pass filter or a rectangular window function applied to an unlimited bandwidth. The resulting si-function (in the theoretical case of a discrete reflective event) has the disadvantage of strong oscillations close to the desired peak at $t = \tau_1$. In a distributed Brillouin measurement, these oscillations will degrade the measurement of sudden local changes of Brillouin gain along the fiber. A common procedure in signal and image processing is the application of an additional window function, thereby smoothing (or tapering) the edges of the available data. The result is a suppression of the oscillations close to the peak of the reconstructed pulse response, coming at the cost of an increase of the peak width.

In this work, the choice of a feasible window function was directly adopted from literature [48]; among the various available window functions, it has been agreed on a Kaiser window [52] to be the most suitable. The left graph in figure 3.4 shows the simulation of a band-limited transfer function ($f_{max} = 20$ MHz) of a singular discrete reflective event at $\tau = 0.5$ μs.

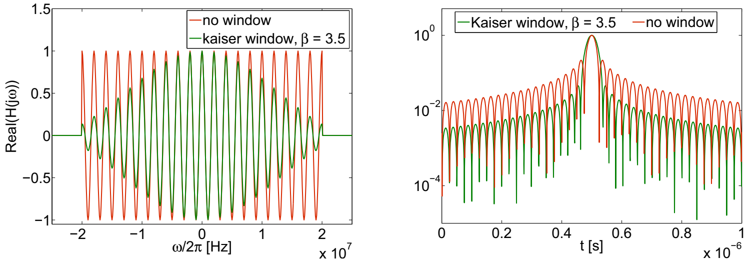

Figure 3.4: Impact of windowing on the shape of the pulse response obtained from a band-limited transfer function [48].

In the right graph, the si-shaped pulse response, resulting from the inverse Fourier transform, is shown. With the Kaiser window function applied (the parameter β affects the side lobe attenuation of the window's Fourier transform), the oscillations are visibly attenuated, while a slight widening of the main lobe has to be accepted.

Lowest frequencies

The measurement of a system's transfer function over a band between f_{min} and f_{max} allows the reconstruction of the pulse response with the constraints given above. It can be easily shown that this reconstruction is independent from the actual position of the measurement band, if the pulse response consists of discrete singular reflective events (objects in radar applications, Fresnel reflections in optical fibers): When $f_{min} = F_0 - \Delta/2$ and $f_{max} = F_0 + \Delta/2$ then the reconstruction solely depends on the bandwidth Δ, regardless of F_0 [45]. The case of low-pass filtering ($f_{min} = df$) was assumed in (3.10). Yet, representations of the desired information (being the location of Dirac pulses with infinite bandwidth) can be found in any frequency band.

In the case of distributed Brillouin sensing, however, not only discrete events of no spatial expansion are to be measured. The spatially resolved profile of Brillouin gain along a fiber contains sections of constant gain for a certain value of Δf. If these sections were to be reconstructed from a transfer function measured at a frequency band around an arbitrarily high center frequency, this would correspond to a band-pass filtering of the signal: With low frequency components missing, the trace would appear as a spatial derivative, highlighting sections of rapid changes in Brillouin gain, while suppressing sections of constant signal intensity. Therefore, the condition $f_{min} = 0$ should be mandatory.

Still, a measurement at $f_m = 0$ yields several problems. Both the generation and the reception of a DC signal are critical with the equipment (VNA, photodetectors) that is designed for RF signal processing in the upper MHz range, due to biasing problems in the active electronics and the strong impact of $1/f$ noise.

The effect of a gap in the transfer function at $f = 0$ in case of a measurement from $f_{min} = df$ to f_{max} is shown in the simulation in figure 3.5: The gap subtracts the DC component (the arithmetic mean) from the trace.

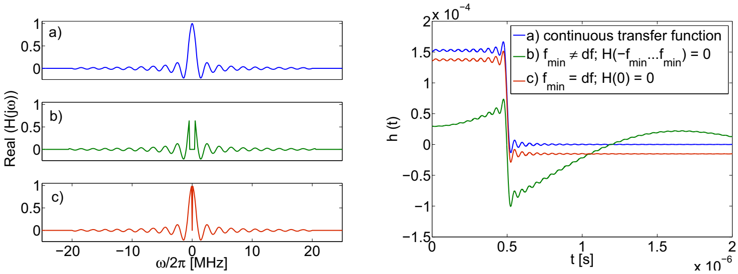

Figure 3.5: Relevance of the low frequencies in $H(j\omega)$: a) Continuous transfer function from $-f_{max}$ to f_{max}. b) Measurement band shifted towards higher frequencies. c) No measured DC value: $H(f_m = 0) = 0$.

The shape of the trace remains unchanged (in contrast to the trace of the shifted measurement band). The reconstruction of the original trace – with its DC offset – is trivial, if the trace $h(t)$ contains at least one point which is known to be zero. In case of a Brillouin gain measurement of a fiber with a known length, a constant term can be added (after reallocation into the spatial domain) such that $h(z) = 0$ for all $z > L$. In a three-dimensional Brillouin gain measurement along z and Δf, this must be done for each value of Δf; measurements using this method will be presented in section 4.4.

Impact of inaccuracies in the measurement of magnitude and phase

A defect in the measurement of the complex transfer function might emerge from various sources within the measurement setup: Both random noise in the electrical and optical signal paths and the occurrence of nonlinearities in the components or within Brillouin interaction along the sensing fiber will introduce errors into the magnitude or phase measurement for each f_m value. In the following, the impact of such a degradation of the transfer function is analyzed with respect to the transformation into the time domain. Any error or noisy value is treated as an undesired addition $\eta\,(j\omega, \Delta f)$ on the transfer function $H\,(j\omega, \Delta f)$. Since the transformation is performed independently from $H(j\omega)$ to $h(t)$ for each sweep value of the laser frequency offset, Δf will not appear in this analysis.

The degraded pulse response $h_\eta(t)$, reconstructed from a faulty transfer function $H_\eta(j\omega)$, becomes:

$$h_\eta(t) = \frac{1}{2\pi} \int\limits_{-\infty}^{+\infty} \underbrace{\big(H(j\omega) + \eta(j\omega)\big)}_{H_\eta(j\omega)} e^{j\omega t} d\omega \tag{3.16}$$

For clarity, the impact of a single defective measuring point in the transfer function is first performed for an error in the magnitude $|H(j\omega)|$ at frequency ω_0 with the correct phase φ. The measured value is

$$H_\eta(j\omega_0) = \big(|H(j\omega_0)| + A_\eta\big) e^{j\varphi} \tag{3.17}$$

which can be expressed, in accordance to (3.16), as an additive term in the measured transfer function. Due to the conjugate symmetry of the transfer function, the additive term consists of a pair of Dirac peaks with magnitude A_η:

$$\eta(j\omega) = A_\eta \big(\delta(\omega - \omega_0) + \delta(\omega + \omega_0)\big) \tag{3.18}$$

The degraded pulse response is then retrieved from the inverse Fourier transform:

$$\begin{aligned} h_\eta(t) &= \frac{1}{2\pi} \left(\int\limits_{-\infty}^{+\infty} H(j\omega) e^{j\omega t} d\omega + \int\limits_{-\infty}^{+\infty} A_\eta \big(\delta(\omega - \omega_0) + \delta(\omega + \omega_0)\big) e^{j\omega t} d\omega \right) \\ &= h(t) + \frac{A_\eta}{\pi} \cos(\omega_0 t) \end{aligned} \tag{3.19}$$

Consquently, a single defect in the magnitude measurement superposes an oscillation of frequency ω_0 on the time-domain trace.

In analogy to the above procedure, a measurement with a defect at $\omega = \omega_0$ in both magnitude and phase is analyzed. The measured phase is the sum of the undegraded phase value is $\varphi = \arg(H(j\omega_0))$ and the error phase φ_η:

$$H_\eta(j\omega_0) = \big(|H(j\omega_0)| + A_\eta\big) e^{j(\varphi + \varphi_\eta)} \tag{3.20}$$

The sum of two signals of different phases is

$$e^{j(\varphi + \varphi_\eta)} = \frac{1}{2\cos(\varphi_\eta)} \left(e^{j\varphi} + e^{j(\varphi + 2\varphi_\eta)} \right) \tag{3.21}$$

so the measured value becomes:

$$\underbrace{H_\eta(j\omega_0)}_{\text{measured value}} = \underbrace{\frac{1}{2\cos(\varphi_\eta)}}_{\text{error term}} \big(\underbrace{|H(j\omega_0)| e^{j\varphi}}_{\text{actual value}} + A_\eta e^{j\varphi} \big) + \underbrace{\frac{|H(j\omega_0)| + A_\eta}{2\cos(\varphi_\eta)} e^{j(\varphi + 2\varphi_\eta)}}_{\text{error term}} \tag{3.22}$$

To obtain the additive noise function $\eta(j\omega)$ and introduce it into (3.16), the actual (undegraded) value is subtracted from equation (3.22) and the resulting error term is again assigned to a pair of Dirac peaks (now with the error term's complex conjugate for negative frequencies):

$$\begin{aligned}\eta\left(j\omega\right) = &\left(\frac{\left|H\left(j\omega_0\right)\right| + A_\eta}{2\cos\left(\varphi_\eta\right)} e^{j\varphi}\left(1 + e^{j2\varphi_\eta}\right) - \left|H\left(j\omega_0\right)\right| e^{j\varphi}\right)\delta\left(\omega - \omega_0\right)\\ &+ \left(\frac{\left|H\left(j\omega_0\right)\right| + A_\eta}{2\cos\left(\varphi_\eta\right)} e^{-j\varphi}\left(1 + e^{-j2\varphi_\eta}\right) - \left|H\left(j\omega_0\right)\right| e^{-j\varphi}\right)\delta\left(\omega + \omega_0\right)\end{aligned} \tag{3.23}$$

The inverse Fourier transform can now be calculated, resulting in an expression for the degraded pulse response, consisting of the undegraded pulse response and a superposed error signal.

$$\begin{aligned}h_\eta(t) = &\frac{1}{2\pi}\left(\int_{-\infty}^{+\infty} H\left(j\omega\right) e^{j\omega t} d\omega\right.\\ &+ \left(\frac{\left|H\left(j\omega_0\right)\right| + A_\eta}{2\cos\left(\varphi_\eta\right)}\left(e^{j\varphi} + e^{j(\varphi + 2\varphi_\eta)}\right) - \left|H\left(j\omega_0\right)\right| e^{j\varphi}\right)\int_{-\infty}^{+\infty}\delta\left(\omega - \omega_0\right) e^{j\omega t} d\omega\\ &+ \left.\left(\frac{\left|H\left(j\omega_0\right)\right| + A_\eta}{2\cos\left(\varphi_\eta\right)}\left(e^{-j\varphi} + e^{-j(\varphi + 2\varphi_\eta)}\right) - \left|H\left(j\omega_0\right)\right| e^{-j\varphi}\right)\int_{-\infty}^{+\infty}\delta\left(\omega + \omega_0\right) e^{j\omega t} d\omega\right)\\ = &\, h(t) + \frac{1}{\pi}\left(\frac{\left|H\left(j\omega_0\right)\right| + A_\eta}{2\cos\left(\varphi_\eta\right)}\left(\cos\left(\omega_0 t + \varphi\right) + \cos\left(\omega_0 t + \varphi + 2\varphi_\eta\right)\right)\right.\\ &\left. - \left|H\left(j\omega_0\right)\right|\cos\left(\omega_0 t + \varphi\right)\right)\end{aligned} \tag{3.24}$$

Again, the resulting error signal is a superposed oscillation with the frequency ω_0, weighted by the magnitude value $(\left|H\left(j\omega_0\right)\right| + A_\eta)$.

The analysis shows that both faulty or noisy magnitude and phase measurements induce a degradation into the signal trace that will not be easily removed in post processing. Equation 3.24 shows that phase inaccuracies (e.g. due to limited accuracy or quantization errors in the phase detector) have an even more severe impact than a defective magnitude measurement. The occurrence of such errors strongly depends on the configuration of the recording system for $H(j\omega)$: If the reference signal for comparison of phase and amplitude is obtained from monitoring the optical pump signal, the system will be much more robust to fluctuations in the components' characteristics (and even to the occurrence of nonlinearities) than in case of a reference directly drawn from the electrical oscillator (in section 4.2, these configurations will be analyzed in more detail).

Measurement of the real part only

Several approaches for an implementation of the frequency domain analysis by means of analog electronics have been presented during the past two decades, both in the field of microwaves and radar reflectometry [43] and in optical metrology [53]. These implementations propose a reduction of complexity and cost of the hardware by measurement of the transfer function's real part only, instead of measuring magnitude and phase, as it is done by a network analyzer. The real part can be obtained from a simple continuous multiplication of the backscattered signal with the reference and a low-pass filter [45], which provides a low-budget and yet elegant way of analog measurement[6]. In this method, each frequency point of the desired signal $\mathrm{Re}\big(H\,(j\omega)\big)$ is recorded by modulating the pump light with a harmonic signal $x(t)$ of frequency f_m, amplitude A_0 and phase φ_0 (again, the analysis is done independently from the sweep of Δf):

$$x(t) = A_0 \cdot \cos\left(2\pi f_m t + \varphi_0\right) \tag{3.25}$$

Brillouin interaction along the fiber transfers the amplitude modulation of the pump light to the Stokes light following the transfer function $H(j\omega)$, with

$$H\,(j f_m) = H_1 e^{j\varphi_1} \tag{3.26}$$

so the signal

$$y(t) = A_0 \cdot H_1 \cdot \cos\left(2\pi f_m t + \varphi_0 + \varphi_1\right) \tag{3.27}$$

will be received at the photodiode. The two signals can now be multiplied:

$$\begin{aligned} x(t) \cdot y(t) &= A_0 \cdot \cos\left(2\pi f_m t + \varphi_0\right) \cdot A_0 \cdot H_1 \cdot \cos\left(2\pi f_m t + \varphi_0 + \varphi_1\right) \\ &= \frac{A_0^2 H_1}{2}\big(\cos\left(\varphi_1\right) + \cos\left(4\pi f_m t + 2\varphi_0 + \varphi_1\right)\big) \end{aligned} \tag{3.28}$$

If the resulting signal is low-pass filtered with a cut-off frequency $f_m < f_{\textit{cut-off}} < 4 f_m$, the resulting signal will be

$$\overline{x(t) \cdot y(t)} = \frac{A_0^2 H_1}{2} \cos\left(\varphi_1\right) = \frac{A_0^2}{2} \cdot \mathrm{Re}\big(H\,(j f_m)\big) \tag{3.29}$$

which is the real part of the transfer function $H(j\omega)$ at $\omega = 2\pi f_m$ (weighted by the constant term $A_0^2/2$).

To reconstruct the pulse response (containing the desired spatially resolved information) without the imaginary part of the transfer function, the real part of the complex transfer function can be written as

$$\mathrm{Re}\big(H\,(j\omega)\big) = \frac{H\,(j\omega) + H^*\,(j\omega)}{2} \tag{3.30}$$

---

[6] The approach was examined within this work before the decision for the development of an all-digital hardware solution was made (whis is described in chapter 5).

With the transformation pairs $H\left(j\omega\right) \bullet\!\!-\!\!\circ\, h\left(t\right)$, $H^{*}\left(j\omega\right) \bullet\!\!-\!\!\circ\, h^{*}\left(-t\right)$ and $h^{*}(-t) = h(-t)$ (for a real $h(t)$), the result of the inverse Fourier transform of $\mathrm{Re}\big(H\left(j\omega\right)\big)$ yields

$$h_{Re}(t) = \frac{h(t) + h(-t)}{2} \tag{3.31}$$

in which $h(-t)$ is a mirrored image of $h(t)$, superposed on the pulse response that would have been the result of a full complex measurement. Consequently, the reconstruction of the spatially resolved backscattering profile of a fiber will still be correct, if $z_{max} > 2L$; in this case, either the desired signal or its image will be zero for each z, and the superposition will not induce any errors. According to (3.6), this condition requires a frequency step width df half as long as in a full complex measurement.

While this approach offers a feasible way to implement the BOFDA method by means of analog electronics, digital circuitry would not require this route; here, the information regarding magnitude and phase can be easily retrieved from the received signal in off-line signal processing. Therefore, the approach of reconstructing $h(t)$ from $\mathrm{Re}\big(H\left(j\omega\right)\big)$ was not followed any further.

Alternative approach using harmonic reconstruction

In contrast to retrieving the spatially resolved Brillouin gain profile from the transfer function via an inverse Fourier transform, Bernini *et al.* have proposed a reconstruction technique that bases on a numerical model of possible distributions of f_B along the sensing fiber, from which a hypothetical transfer function is extracted [49]. This is done by means of a numerical solution for simplifications of the three differential equations that form the complete description of stimulated Brillouin scattering (2.19), (2.36) and (2.37). This transfer function is then iteratively altered in its parameters until its similarity to a measured transfer function converges, thereby yielding the physical distribution of Brillouin gain along the fiber.

The strength of this method is its ability to model undesired physical effects that cause problems in both BOTDA and BOFDA techniques, such as transient effects on the acoustic wave or spectral broadening at high spatial resolution [54] (see chapter 6). On the downside, the algorithm for the reconstruction of the physical transfer function is computationally expensive, since in each iteration, the set of differential equation has to be solved, and convergence is not assured for all arbitrary distributions of f_B.

CHAPTER 4

The laboratory setup for the BOFDA system

The corner pillars of the setup for Brillouin frequency domain measurements are the two variables that span the axes of the desired three-dimensional data trace: the offset between the two laser frequencies Δf and the modulation frequency of the pump beam f_m. The starting point for realization of the corresponding sweeps is the setup known from previous works [34], [48]. This chapter focuses on the advancements of the setup that have been achieved within the work on this thesis: The development of a stable and accurate control for Δf; enhancement of the efficiency for the recording of the transfer function by using one photodiode only; and, finally, elimination of gain fluctuations due to polarization effects. The chapter concludes with a presentation of measurement results that validate the performance of the overall BOFDA system.

Figure 4.1 shows the complete laboratory setup of the Brillouin frequency domain analysis. The optical signal path that provides the beat signal at the 25 GHz photodetector (the output of which is directed to the spectrum analyzer to extract the current value of Δf), remains unchanged from the setup for the pump threshold measurement in section 2.2.1. The control voltages for laser frequency tuning are again applied to the source that operates as the pump laser; the automated control loop is described in the next section. Into the optical signal path that enters the fiber under test, the electro-optical modulator (EOM) for application of f_m to the pump signal is introduced, followed by a 2x2 fiber optic coupler that diverts the reference signal (forward direction) and the backscattered Brillouin signal (backward direction). The two signals are converted into the electrical baseband by two 1 GHz photodetectors; their comparison in amplitude and phase is performed by a vector network analyzer (VNA, frequency range: 1 Hz to 500 MHz), which at the same time provides the electrical modulation signal at the variable frequency f_m.

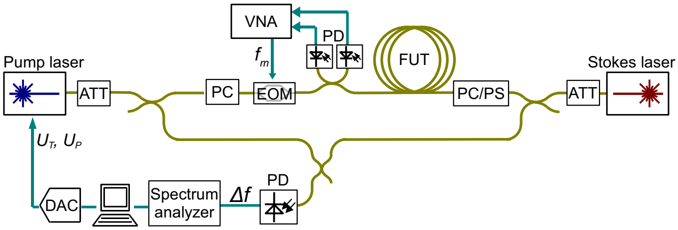

Figure 4.1: The complete BOFDA setup. EOM: electro-optical modulator; VNA: vector network analyzer; DAC: digital-to-analog converter.

The polarization controller in the pump path serves to maximize the extinction ratio of the EOM: The $LiNbO_3$ (lithium niobate) planar waveguides within the device require a beam of perfect linear polarization. The second polarization controller (which will be replaced by a scrambler module (PS) in later configurations) maximizes the average Brillouin gain that the injected Stokes light will experience while it travels along the fiber under test.

4.1 Generation of the optical frequencies

4.1.1 Control of the frequency offset of two Nd:YAG lasers

The tuning mechanisms for the optical frequencies that are provided within the two Nd:YAG laser sources have been described in section 2.1.4 on page 25: Rough tuning can be achieved by cooling down the laser's crystal oscillator via a TEC element that is attached to the crystal [35]. The element is controlled by a voltage U_T within a range from -10 to 10 V with a coefficient $df/dU_T \approx 3.8$ GHz/V. Fine (and fast) tuning is done by a voltage U_P applied to a piezo actuator which squeezes the resonator, accepting a range from 0 to 30 V with $df/dU_P \approx 1$ MHz/V [35].

The basic operating point needs to be set in a way that one of the lasers can be controlled to maintain δf around the fibers' natural f_B around 12.8 GHz. It is defined by the rough tuning via U_P. Therefore, the characteristic dependence on f_B with U_T subsequently applied to both lasers was measured; the resulting traces are shown in the left graph of figure 4.2. The graph confirms the slope of 3.8 GHz/V that was specified in the lasers' manual for the linear regions. Moreover, it shows the location of strong nonlinearities caused by mode hops in the resonator.

Candidates for the operating point are any interception of the data traces with the dashed line depicting $f_B = \pm 12.8$ GHz. An interception furthest away from the next mode hop and with a relatively small required U_T value is chosen. At this operating point, the laser source of higher frequency is the one with the control voltage applied; consequently, it is the one that from here on will be operated as the pump laser.

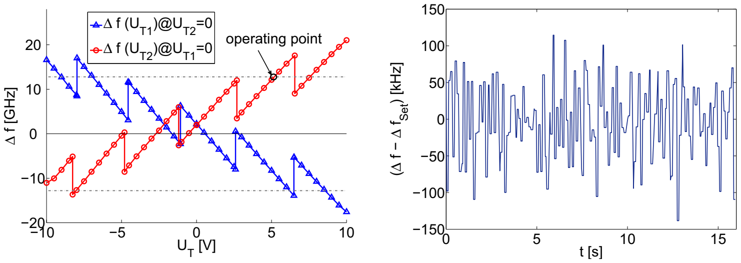

Figure 4.2: Controlling the Nd:YAG lasers. *Left:* The impact of the control voltages (U_{T1}: voltage on TEC of Laser 1; U_{T2}: voltage on TEC of Laser 2) on the optical frequencies. *Right:* Performance of the automatic control loop for stabilization of Δf.

A detailed description of the working principle for the control loop that was designed to provide a stable frequency offset with sweepable Δf values is given in figure 4.3. The algorithm that is depicted in the shaded areas was implemented in NATIONAL INSTRUMENTS' LabVIEW software. Communication with the spectrum analyzer to adjust its settings and to retrieve the current Δf value and with the network analyzer to start the measurement and to get the data is done over a GPIB interface; from comparison of the actual Δf value to the desired value Δf_{set}, the required control voltages U_T and U_P are calculated and sent to a specially developed DAC board of high accuracy over the serial port (RS-232). A microcontroller manages the received data and controls the output of the two digital-to-analog converters; some parameters of the output voltages (offset, reference, gain) can be adjusted manually on the board.

The performance in terms of speed and accuracy of the control loop can be seen in the right graph of figure 4.2. From the software user interface, the coefficients df/dU_T and df/dU_P can be adjusted to assure the stability of the system. The sampling frequency of the loop is governed by the data transmission paths via GPIB and RS-232; a rate of 25 samples per second has been achieved. The resulting accuracy for Δf lies well within ±150 kHz with a standard deviation of 52 kHz.

4.1.2 The sideband technique using a single DFB source

In 1997, Niklès *et al.* proposed a configuration for Brillouin gain spectrum characterization that works on the basis of one single semiconductor (DFB) laser [36]. The central idea of this concept is to modulate the laser's amplitude with an RF signal of a frequency in the range of f_B. Before the modulation, a part of the unmodulated carrier signal is injected into one end of the fiber under test, operating as the pump beam. The remaining optical power is modulated to create sidebands in the optical

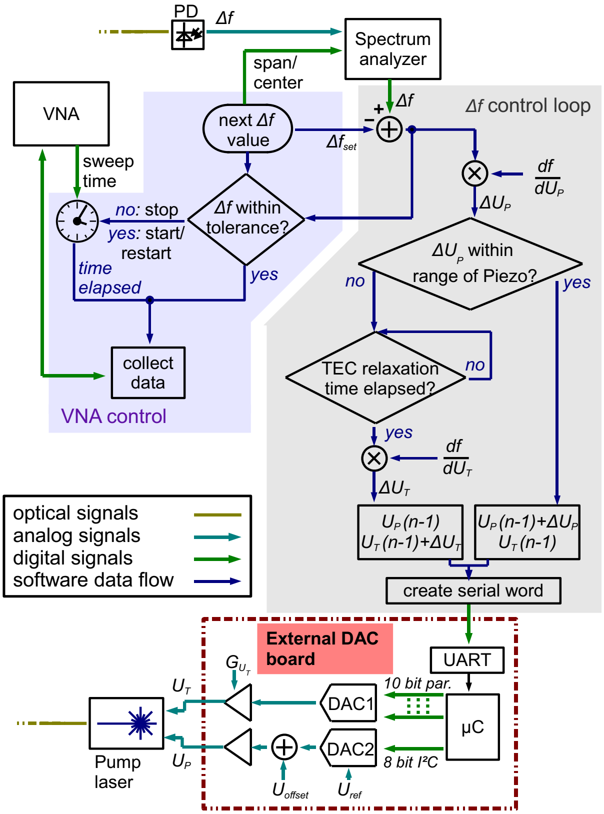

Figure 4.3: Flow chart of the control loop that was designed to provide a stable sweep of Δf.

spectrum, spaced from the original (carrier) frequency by the modulation frequency[1]. The lower sideband will then act as the Stokes signal; the upper sideband will adopt the role of a pump wave in relation to the carrier which is then seen as a Stokes wave. Because in this constellation the pump light is far weaker than the Stokes light, the upper sideband will be depleted [36].

---

[1] A thorough analysis of amplitude modulation can be found in chapter 6.

The two main advantages of this technique are the downsizing of the overall setup from two laser sources to one and the generation of Δf by a direct modulation signal, saving relaxation and settling time of a control loop to drive two separate lasers. On the downside, signal quality is degraded by nonlinear effects that arise from co-propagating optical frequencies and undesired interaction between the carrier and remainders of the upper sideband [55].

The sideband technique has matured throughout recent years, with solutions that have been proposed for several critical issues. Considerations for setting of the operating point of the modulator that creates the sidebands have been presented [36]; the conditions for self-depletion of the upper sideband have been formulated [36]; a two-laser technique that uses the sideband method to lock the optical frequencies by injecting the modulated signal of one laser into the second laser's resonator was presented [56]. Such advancements have made the sideband method the most common technique for frequency-offset generation in commercial Brillouin sensing systems. Although the sideband technique is currently in the state of implementation in the laboratories at BAM – and even has produced first results of distributed measurements by the time of writing – this thesis will not go into more detail on this large field. The technique is known to be efficient and reliable; no innovation or advancement has been approached within this work, since research was clearly focused on the recording and analysis of the spatially resolved Brillouin gain profile, which is (largely) independent from the method used to generate Δf. For this task, the two Nd:YAG lasers with their high spectral purity and high output powers have proven to be an adequate tool for the research.

4.2 Measuring the complex transfer function

On the laboratory test bench, a vector network analyzer is employed for measurement of the complex transfer function: The response of the system to harmonic signals with the frequency f_m, varied from f_{min} to f_{max}. The transfer function is then transferred into the spatial pulse response as described in section 3.2. A vector network analyzer is a common tool in microwave engineering, where its most usual task is the measurement of S parameters of an electric two-port. From this point of view, the transfer function can be seen as the parameter s_{21}, which characterizes the relation between the system's output to the input. The reflection parameters s_{11} and s_{22} are of no relevance in the BOFDA setup.

The transfer function is now measured by simultaneously recording the system's input and output. The system itself is the optical fiber with its potential Brillouin amplification; thus, the input is the excitation by the modulated pump beam, while the output is the Stokes beam with the input's modulation frequency attached to the original CW beam by stimulated Brillouin scattering. The measurement of the Stokes beam must be done via an optical fiber coupler in backward direction, which is fed to a photodetector (see figure 4.1), the output signal of which is the electrical representation of the modulation frequency. Compared to the input signal, this signal will still be of frequency f_m and only be altered in amplitude and phase (if all prerequisites on linearity from section 3.2.3 hold true).

For the measurement of the excitation signal, which is required at the reference input of the VNA, there are several possibilities. The simplest approach is depicted in figure 4.1: A second photodetector is connected to the fiber optic coupler just before the pump light enters the sensing fiber, bringing the exact excitation signal to the VNA. If the frequency responses of the two photodiodes can be assumed to be identical, the amplitude ratio and phase difference measured by the VNA will correspond directly to the transfer function of the sensing fiber[2].

Alternatively, the electrical modulation signal – which is generated by the internal oscillator of the VNA – could be used directly as the reference signal, because it contains the required information (amplitude and phase) of the excitation. The setup for this approach is shown in figure 4.4.

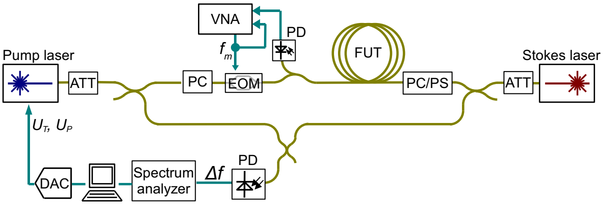

Figure 4.4: BOFDA setup with only one photodetector, using the electrical signal f_m as the reference.

In this configuration, the path of the optical Stokes signals contains a number of elements that are not accounted for in the reference path, but will have an impact on the measured transfer function due to their own frequency response: The electro optical modulator with its imperfect input impedance match, the single remaining photodetector and all other electrical components such as the power splitter and (not depicted in figure 4.4) the power amplifier that was used for full-range operation of the modulator. With this discrepancy between the two paths, the measured transfer function $H'(j\omega)$ is a product of the desired transfer function of the sensing fiber with all the frequency responses of the components in the signal path:

$$H'(j\omega) = H_{VNA}(j\omega) \cdot H_{EOM}(j\omega) \cdot \underbrace{H(j\omega)}_{\text{desired TF}} \cdot H_{PD}(j\omega) \cdot \ldots \tag{4.1}$$

The configuration that is shown in the left hand drawing in figure 4.5 directly routes the excitation signal to the signal input of the VNA, thereby only recording the chain

---

[2] Because such an equilibrium between the two paths can not always be presumed – the photodetectors as well as the input paths of the VNA might differ slightly in their frequency response – a calibration procedure equivalent to the one described in the next paragraph was performed for each measurement.

of undesired frequency responses. This setup provides a calibration function

$$H_{cal}\left(j\omega\right) = H_{VNA}\left(j\omega\right) \cdot H_{EOM}\left(j\omega\right) \cdot H_{PD}\left(j\omega\right) \cdot \ldots \tag{4.2}$$

that serves to restore the originally desired transfer function of the sensing fiber:

$$H\left(j\omega\right) = \frac{H'\left(j\omega\right)}{H_{cal}\left(j\omega\right)} \tag{4.3}$$

Thus, the measurement of the BOFDA trace can be achieved without a second photodiode by only the small additional expense of a single calibration measurement (which serves for all measured traces of the Δf sweep), followed by a simple division of the magnitudes and a subtraction of the phase angles from the measured transfer function.

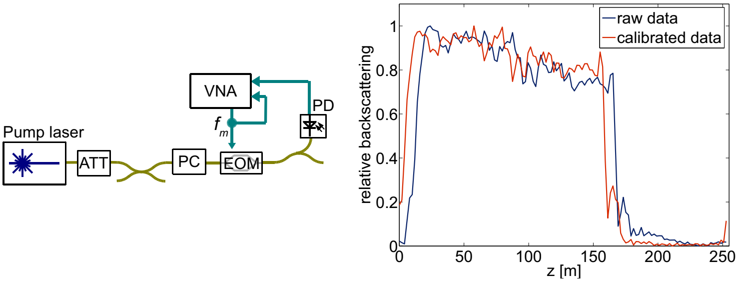

Figure 4.5: *Left:* Configuration for the calibration measurement. *Right:* Impact of the calibration procedure.

To illustrate the impact of calibration in a single-photodiode measurement, the right hand graph in figure 4.4 shows the measured (normalized) Brillouin gain profile of a 170 m long unstrained fiber section at constant temperature with $\Delta f \approx f_B$ (the trace being the result of the Fourier transform $h(z, f_B)$). Three aspects catch the eye in which the calibrated curve differs from the raw data: First, there is a delay in the raw data at the beginning of the trace, shifting the entire section of Brillouin gain to the right; second, the raw data shows a stronger decrease of signal intensity over the fiber length than the calibrated data; third, calibration provides a signal of roughly zero Brillouin gain for $z > L$, which is a condition for a physically relevant measurement result.

4.3 Polarization issues

An analysis of the dependence of the Brillouin gain on the states of polarization (SOP) of the two light beams was presented in section 2.1.3. In short, it was shown that if both the pump and the Stokes beam are linearly polarized, there is maximum gain for parallel states and minimum gain for orthogonal states of polarization. For circular polarization, gain is maximum for identical senses of rotation (when seen from one side) and minimum for opposite senses. For distributed sensing using fibers with low birefringence – such as standard telecommunication fibers – this means, that the Brillouin gain will fluctuate along the fiber, since both beams will change their SOP while propagating along the medium. It has been shown [57] that the averaging of two measurements at orthogonal initial SOP of one of the beams at the beginning of the fiber will not cope entirely for these fluctuations. Averaging over three SOP, being linear, circular and 45° (e.g. the points H, R and P on the Poincaré sphere, see figure 4.6), will cancel out the fluctuations, if the required initial SOPs are adjusted accurately [57].

In practice, it is hardly feasible to adjust the polaraziation to three states equally spaced on the sphere without a polarization analyzer that monitors the current SOP. The approach that is commonly used to cope with this problem is to scramble one of the two polarizations. This was done in the measurements of the defined strain profile that will be presented in the next section on page 61, using a 4-axis polarization controller which has a scrambling option with a frequency of 300 Hz. For later measurements, a scrambling module with a frequency of several MHz became available; it was employed for the measurements in chapters 5 and 6.

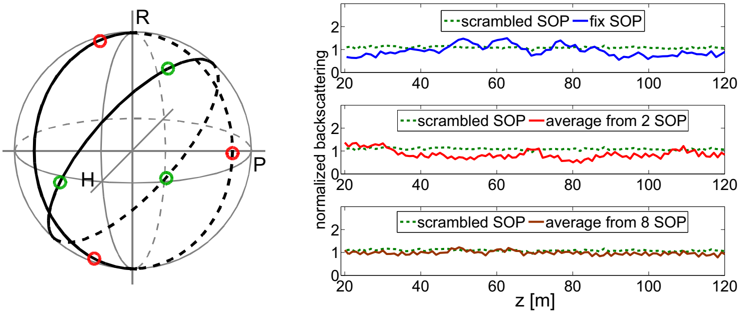

Figure 4.6: *Left:* The Poincaré sphere with circles corresponding to the rotation of the SOP by activating a single channel of a polarization control device. *Right:* Measured $h(z, \Delta f = f_B), L = 100$ m, normalized to average gain of the scrambled measurement) using different numbers of SOP for averaging.

A drawback of simply scrambling one of the two polarizations is the introduction of random fluctuations, that can only be eliminated by an increase of measurement time (either by narrowing the filter bandwidth within the VNA or by averaging over a number of measurements). Therefore, an alternative approach was investigated: If the measurement of $H(j\omega, \Delta f)$ is repeated at a fixed number of states of polarization that are distributed over the Poincaré sphere, an averaging procedure that is much more efficient than stochastical scrambling can be performed; in this case, no change of the initial SOP occurs while recording the response of one single sweep value of f_m. The fixed initial SOPs can be predefined by empirically selecting equally spaced voltages for the channels (piezo actuators) of the polarization controller. No precision is to be expected from the determination of the SOP on the sphere, but using more than one channel (each of the channels will rotate the SOP around a different axis, see figure 4.6) makes it possible to find reasonable settings of the controller for averaging.

As can be seen in figure 4.6, the fluctuations of a Brillouin gain trace, recorded using one single initial SOP, are quite strong. When averaged with a supposedly orthogonal initial SOP applied to the Stokes beam, the fluctuations decrease slightly. Averaging over eight different SOP at each modulation frequency, obtained by setting two points on each of three channels of the polaization controller ($2^3 = 8$), give a good signal. The fourth channel has proven to be redundant, since three axes give a good covering of the sphere. Only slightly more noise is added with respect to the measurement using the scrambler. Such point-wise averaging of the SOP benefits from the separate measurement at each modulation frequency which is inherent to the BOFDA technique and offers the potential of increasing the measurement speed significantly.

4.4 Results of distributed strain measurements

During the three years of research, a large number of measurements was performed with ever changing setup configurations, measurement parameters and fibers under test. Throughout the remaining chapters of this thesis, several distributed measurements of Brillouin gain will be presented; they will reference the subjects of the respective chapters (all-digital measurements in chapter 5, the issue of high resolution in chapter 6, measurements with real-life geotechnical relevance in chapter 7) and thereby trace the overall development of the BOFDA system throughout the research. To maintain a consistent overview over the system evolution, the parameters of all distributed measurements presented in this thesis are summarized in table A.1 in appendix A.1.

The measurement presented in this section was performed in order to provide a well-grounded validation of the performance of the BOFDA system in the configuration from figure 4.1. A fiber section was coiled up using the apparatus for generation of defined strain values that was described in section 2.2.2, thereby generating a coil that contained a strain profile of a total length of 215 m. The sections of varying strain along the profile are drawn in figure 4.7. Prior to the defined strain profile that is fixed on the grooved fiber coil, a coated patch-cord of 200 m length was placed. With a 5 m patch-cord to connect the 200 m cable with the strain profile, the fiber under test for this measurement had a total length of 420 m.

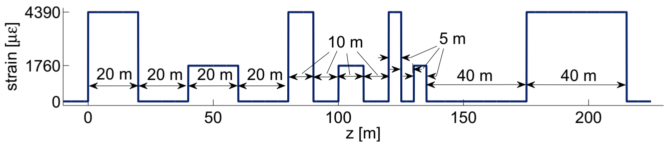

Figure 4.7: Strain sections applied to the grooved fiber coil for distributed measurements on a defined strain profile.

The measurement was performed with a sweep range of f_m from 100 kHz to 30 MHz, yielding a maximum measurement length of 1021 m and a spatial resolution of 3.4 m; Δf was swept from 12.7 GHz to 13.15 GHz with a step width of 2.5 MHz.

The measurement results are shown in figures 4.8, 4.9 and 4.10. The left graph in figure 4.8 shows the magnitude of the transfer function $|H(j\omega, \Delta f)|$ as the result of the frequency domain measurement. After inverse Fourier transform, the pulse response $h(t, \Delta f)$ is reconstructed and can be reallocated to the spatially resolved distribution of Brillouin gain $h(z, \Delta f)$ via equation (3.1), resulting in figure 4.8 (*right*).

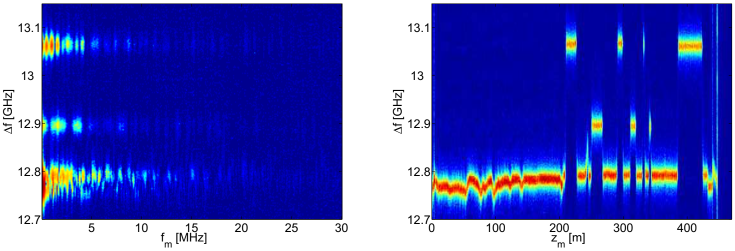

Figure 4.8: *Left:* Magnitude of the measured transfer function $|H(j\omega, \Delta f)|$ of the strain profile. *Right:* Reconstructed pulse response $h(z, \Delta f)$ of the strain profile.

Figure 4.9 shows the same data as the right hand graph in figure 4.8, but in a three-dimensional representation, to depict the clearly resolved Lorentzian shape of the Brillouin gain spectra.

Figure 4.10 shows the result of the final analysis: The signal traces at each spatial position along z are separately fed into a curve-fitting procedure to localize the maximum of the Lorentzian-shaped Brillouin gain spectra along Δf; this is done by means of a cross-correlation between the measured trace and a theoretically expected Lorentz function. The maximum from the correlated (fitted) curve represents f_B for each spatial position. The f_B value is directly transferred into the value of longitudinal strain in the fiber, using the coefficient from page 33. The absence of local temperature gradients along the strain profile is presumed (since the fiber is wound

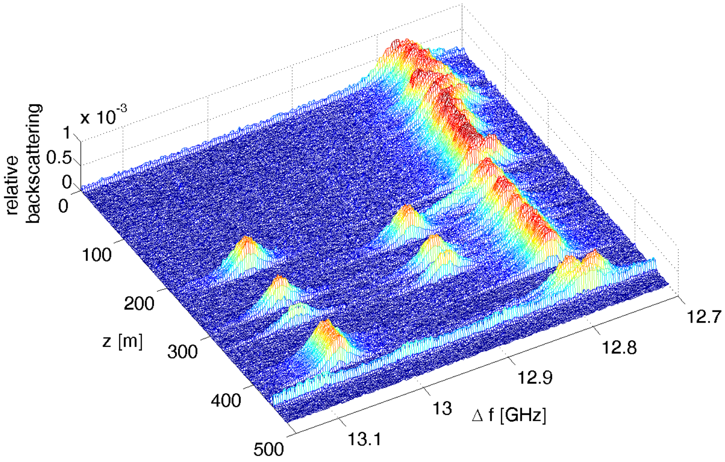

Figure 4.9: Three-dimensional representation of the spatially resolved Brillouin gain spectra (same data as figure 4.8 (*right*)), measured on the defined strain profile.

up on a single coil and maintained in the laboratory at a constant temperature of 20 °C, this is a safe presumption).

Five characteristics of the data traces shall be pointed out in order to further characterize the system and its measurement results:

- The characteristic Lorentzian shape of the Brillouin gain is clearly observable in figure 4.9 at all positions along the fiber. Only at sections of harsh transition of f_B, the gain spectra lose their shape and show a blur along the Δf axis.

- At $z = 5$ m, $z = 440$ m and $z = 447$ m, Fresnel reflections are clearly visible. At these positions, fiber sections are interconnected with FC connectors with an angled physical contact (FC/APC). These Fresnel reflections are independent from Δf and of an indefinitely short spatial dimension (in the measurement trace, broadened to the system's minimum spatial resolution).

- Prior to the defined strain profile that is fixed on the grooved fiber coil, the coated patch-cord of 200 m length was placed; the patch-cord had previously been unrolled from its coil and wound up again, a procedure in which insufficient care had been taken. As a consequence, the coated fiber experienced arbitrary strain when it was wound up, which becomes obvious in figures 4.8 (*right*)

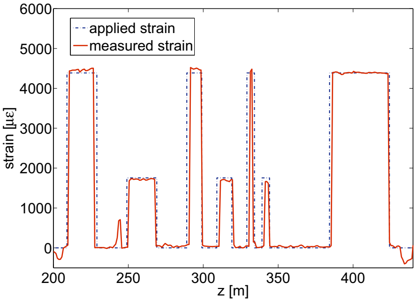

Figure 4.10: Final analysis of the distributed strain measurement.

and 4.9. The capture of this arbitrary strain distribution on the poorly wound-up patch-cord can be considered as an additional demonstration of the system's sensitivity.

- Fluctuations of the maximum Brillouin gain for each spatial position (gain at $\Delta f = f_B$ along the z axis) has been largely eliminated by scrambling the polarization state of the Stokes beam. From the spatially resolved signal, the fluctuations within the unstrained section between $z = 5$ m and $z = 205$ m can be read off to lie within a range of 1 dB.

- In figure 4.10, a narrow peak at $z = 244$ m which is not part of the defined strain profile can be seen. Since the peak has a correspondent in the 3D-representation of the Brillouin gain, where a narrow slice of gain spectra emerges from the region of unstrained fiber towards higher strain regions, the peak is clearly of mechanical nature: It can be interpreted as an irregularity that occurred during the process of winding up the fiber coil, and did not emerge during measurement or post-processing.

In conclusion, it can be said that the laboratory setup shows a reliable performance, meeting the expectations on spatial resolution and resolution of the measurand. With a data acquisition time of approximately 30 minutes, it can be considered to be feasible for many practical applications (one of which is the monitoring of earth structures for flood protection). Doubtless, the laboratory setup that was presented in this chapter – with its large bench top devices such as the spectrum analyzer and the VNA, as well as with the two delicate and expensive Nd:YAG lasers – is far from being a solution for a monitoring system to be applied in the field. While a feasible alternative for the laser sources was presented in section 4.1.2, the next chapter will deal with an efficient way to implement the acquisition of the complex transfer function, thereby substituting the VNA by a specially developed hardware configuration.

CHAPTER 5

Digital determination of the complex transfer function

Despite the proof of concept of the Brillouin frequency domain analysis in the laboratory, which had been achieved several years prior to the work on this thesis [34], the technique has not been implemented into a compact, portable unit – in contrast to the BOTDA technique, which has found its way into a number of commercially available measurement devices. The largest step to take in order to close the gap on the BOTDA state-of-the-art is the implementation of the recording of the complex transfer function, so far conducted by a bench top vector network analyzer. Such a device is high in precision, but clearly overdimensioned for the measurement of the single network parameter s_{21} (which directly corresponds to the transfer function $H(j\omega)$ in the BOFDA setup) with a bandwidth of 100 MHz. The design of an efficient electronic circuitry to replace the large and heavy bench top VNA was therefore mandatory if the BOFDA technique was ever to be brought to its destination of on-site structural health monitoring.

5.1 The concept of a digital BOFDA system

For an efficient implementation of the Brillouin frequency domain analysis into a compact and robust measurement unit, two competing concepts have to be considered: A classical analog approach has already been presented on page 51 in section 3.2.4. It is known from radar applications [45], where the frequency domain analysis has been implemented efficiently by performing an analog multiplication of the received signal and the reference; after low-pass filtering, this yields the real part of the transfer function (equation (3.29)).

The counterpart to this analog technique is the straight-forward transfer of the tasks of the VNA into a digital signal processing hardware, with analog to digital (A/D) converters right after the photodetectors. The most evident limitation of such a digital system is the achievable bandwidth, determined by the sampling rates of available converters. For this criterion, an investigation on A/D converters and their current state of the art shows, that the desired bandwidth of 100 MHz is indeed a challenging benchmark, but definitely achievable with current commercial technologies. With this basic limitation of digital hardware being overcome, the classical argumentation in favor of digital technology points out its major advantages. The main issues are listed in the following:

- The BOFDA technique requires a considerable analog bandwidth, determined by the maximum measurement length (see equation (3.6)) and the spatial resolution (see equation (3.11)). For a measurement length of 10 km and a spatial resolution of 1 m, the transfer function $H(j\omega)$ must be measured from 10 kHz to 100 MHz, a range of four decades. In an analog implementation, analog filtering and the design of structures such as baluns, transformers and bias tees are challenging tasks. In a digital implementation, the problem still arises in front of the A/D converters, but afterwards all signal paths are free from analog concerns. Adaptive filtering is easily implemented over a wide frequency range; if high efficiency is needed, the sampling rate should be designed to be adaptive.

- In the analog implementation that was suggested on page 51 in section 3.2.4, the multiplication of the signal with the reference yields a DC voltage corresponding to the real part of the transfer function (equation (3.29)). Such a DC signal is complicated to handle, since $1/f$ noise and coupling of signals of higher frequencies over the PCB will degrade the dynamic range. A digital design would completely avoid such problems.

- In the analog design (just as in VNA measurements), the settling time of the analog filters, which is inversely proportional to their bandwidth, governs the data acquisition time. By A/D conversion, all data can be processed off-line, which allows pipelining of different tasks and thereby enables fast measurements at a comparable dynamic range.

- The cost of the electronic components and the PCB designs is significantly lower for a digital implementation; all analog multipliers, phase comparators and filters are sophisticated devices for the large bandwidth that is required. Moreover, a delicate design of all signal paths on a circuit board is needed. In contrast, a digital approach offers the possibility of performing these tasks within a digital signal processor (DSP) or a programmable logic device (such as an FPGA or a CPLD). This reduces large parts of the design to software implementation, which decreases the design's error-proneness and the overall number of costly integrated circuits.

The central idea of the digital concept is to capture a time-domain wave form of a defined length of the measurement signal (the Stokes signal that has adopted the pump's amplitude modulation due to Brillouin interaction). The signal is band-pass filtered around the modulation frequency f_m; its phase and amplitude are compared to a reference, thereby recording $H(j\omega)$ with $\omega = 2\pi f_m$. In the following, considerations concerning the realization of filtering and the nature of the reference for phase and amplitude are presented.

5.1.1 Possible configurations for the digital setup

One possible configuration for the measurement of the transfer function of SBS along a fiber is shown in figure 5.1. At a closer look, it is not so different from the laboratory setup from figure 4.4, in which only one photodetector was used. The received signal that comes from the photodetector is limited in bandwidth for anti-aliasing by a low-pass filter (LPF) and then digitized by an A/D converter. The amplitude modulation of the pump signal is carried out by an electro-optical modulator like before; the modulation frequency is generated by a digital synthesizer, which also provides the reference signal at the input of a second A/D converter.

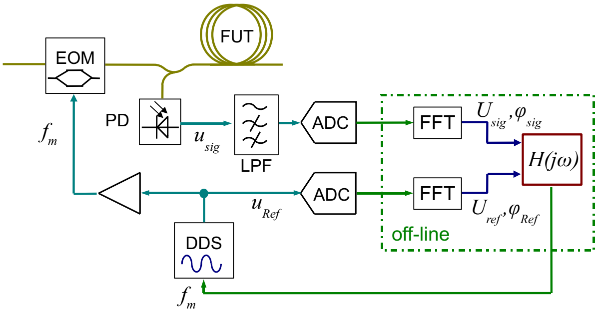

Figure 5.1: Setup for a digital recording of the complex transfer function.

The two interlaced parameter sweeps of f_m and Δf are performed as in the analog setup; for each point in the sweep matrix, the time-domain wave forms of both the signal and the reference are recorded and digitally buffered. From here, all further processing is performed off-line within an external computer. A Fourier transform (performed by an FFT algorithm) provides the frequency spectra of both signals; from this, the gain and phase values can be directly extracted and compared. As a result of the two sweeps, the system yields $H(j\omega, \Delta f)$, which can be transformed into the time domain, and thus, into the spatially resolved Brillouin gain profile.

While the processing of the received signal is straight-forward, the generation of the signal that is used for modulation, and, at the same time, serves as the reference for acquisition of the transfer function, leaves more room for discussion. The most accurate and efficient way to generate a sinusoid of tunable frequencies over a large range is to employ a direct data synthesis (DDS) circuit. As it is introduced in figure 5.1, it will yield accurate results if the calibration procedure from section 4.2 is performed to extract the desired transfer function of Brillouin interaction along the fiber under test from the chain of undesired frequency responses (equation (4.3)).

The DDS creates the sinusoid of frequency f_m from a numerical look-up table and uses its internal digital-to-analog converter to generate a continuous analog signal. This signal is then split in two parts: one to drive the modulator, the other one to be directly converted back into the digital domain where it serves as the reference signal. This signal path appears a little clumsy: Because the only task for the reference signal is to provide the phase of the excitation signal (its frequency is a known sweep parameter, and the amplitude does not change over the f_m sweep) it can be argued that it is little efficient to employ a second ADC channel into which the entire analog wave form of the modulation signal is fed, if the sinusoid with its fixed phase had been generated digitally in the first place. Yet, in a demonstrator setup performing the DDS and the data processing on separately integrated circuits, the digital data is not available to feed it numerically into the data acquisition, in which it could provide the phase reference for the transfer function.

Nevertheless, the possibility of the creation of a single reference signal – such as a rising edge to trigger the data acquisition instead of the entire analog wave form that occupies a second ADC channel – is to be investigated within the demonstrator setup. The generation of such a signal is therefore part of the design of the digital f_m generation and will be accounted for in the following discussion.

5.1.2 Preliminary tests

As a first proof-of-concept for the digital approach to record the complex transfer function, measurements were performed in which the task for the digital setup was performed by an automated oscilloscope. The setup corresponds to the one in figure 4.1, including the VNA being the source of the modulation signal. The only modification is the connection of the two photodiodes' outputs to either of the two oscilloscope channels instead of the VNA. On a standard fiber of $L = 170$ m, a single spatially resolved trace near $\Delta f = f_B$ was measured (since the oscilloscope response and data storage is extremely slow, even the measurement of a single f_m sweep over 50 points took about two hours; a full recording of the spatially resolved gain spectra including a sweep over Δf was not feasible). The amplitude resolution of the oscilloscope was adjusted to the signal level for each sweep point; both the reference and the received signal wave form were stored, and an off-line FFT of both wave forms for each sweep point provided the transfer function in gain and phase. A comparison of the oscilloscope measurement to a VNA measurement with the same sweep parameters is shown in figure 5.2 (the traces show the spatially resolved Brillouin gain profile $h(z, f_B)$ as a result of the inverse Fourier transform of the transfer function).

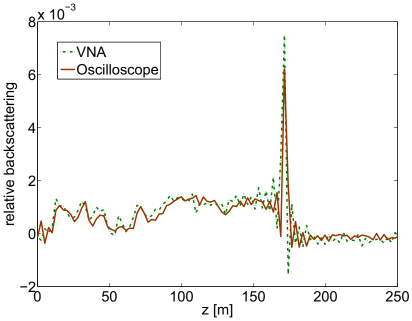

Figure 5.2: Measurement on a 170 m fiber at $\Delta f \approx f_B$; the transfer function $H(j\omega, f_B)$ is measured both with an Oscilloscope and a VNA and transferred into the spatially resolved Brillouin gain profile $h(z, f_B)$.

The remarkable result of this comparison is the congruence of the spatial fluctuations of Brillouin gain (resulting from polarization changes, see section 4.3) in both measurements and the accurate finding of the Fresnel end reflection at $z = 168$ m. Even with the inefficient handling of the remotely controlled oscilloscope, it could be shown that an accurate Brillouin gain profile can be recorded without the bench-top VNA, using significantly less costly equipment.

Two major inaccuracies emerged from the oscilloscope's nature: First, its vertical resolution is 8 bit, which corresponds to a dynamic range of 21 dB and is poor compared to state-of-the-art A/D converters. The amplitude resolution can be adjusted to the signal level by increasing the gain at the input of each channel, which assures an accurate phase measurement; yet, since the gain adjustment is performed in discrete steps and not simultaneously on both channels, it introduces a frequency-dependent discrepancy between the reference and the measurement signal. Second, the limited sampling length of 2400 samples corresponds, when fed into the FFT, to a band-pass filtering with a very wide bandwidth compared to the filtering in the VNA (this correspondence will be discussed in the next section). These two drawbacks, as well as the problem of slow measurements due to the remote control of the oscilloscope, are eliminated in the design of a demonstrator circuitry for a complete digital network analysis to be used for distributed Brillouin measurements.

5.2 Implementation of the demonstrator

5.2.1 Digital generation of the modulation signal

Of all the tasks that the VNA had performed in the analog setup (described in section 4.2), the generation of the modulation signal – the sinusoid that defines the sweep of f_m – was the first to be transferred into a specially designed hardware as a part of the digital demonstrator. The signal generation itself is most accurately performed by a direct data synthesis (DDS) circuit. Driven by a precision crystal clock, a counter reads out a look-up table in which the values of a sine function are stored; depending on the desired output frequency, the counter skips a defined number of table values in each step, thereby putting out a defined number of cycles per time unit to an digital-to-analog converter (DAC). Such a DDS is readily available as an integrated circuit; the demonstrator board has the task to manage the remote control of the frequency output and to provide the supply voltages and the clock signal. Furthermore, the analog output path has to be designed, including impedance-matching of the DAC output to the desired signal connectors and analog filtering to smoothen the wave form of the converted signal.

A labeled photograph of the printed circuit board designed to host and control the DDS is shown in figure 5.3. The board was designed to provide f_m values from 20 kHz to 20 MHz (corresponding to a spatial resolution of 5 m for $z_{max} = 5000$ m). A 125 MHz clock was chosen to sample the table values of the sine function, providing a comfortable head space above the theoretical minimum sampling frequency of $2 f_{max}$. The DDS clock is provided by an on-board crystal oscillator; its signal is split before arriving at the DDS to be buffered and further distributed to a coaxial connector, where it can feed the analog-to-digital converters and thereby become a centralized system clock.

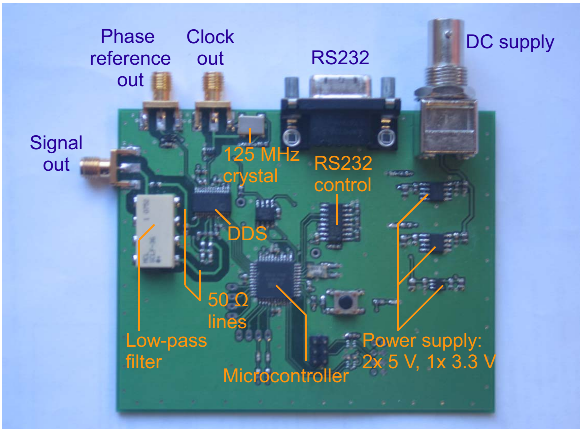

Figure 5.3: Photograph of the demonstrator board containing the direct data synthesis and the generation of a phase reference to acquire the complex transfer function.

An integrated passive low-pass filter with a cut-off frequency of 30 MHz was used to smoothen the analog output. The board layout of the analog output path was designed to provide 50 Ω lines from the DAC output of the DDS to the filter and further to the coaxial connectors in order to minimize reflective losses along the path.

Communication with the external control computer occurs via a serial RS232 connection; the control software on the computer (implemented in MATLAB) sends the current f_m sweep value to the microcontroller, which translates the serial word into the parallel frequency information for the DDS. The amplitude of the analog output can be adjusted on-line as well; here, the microcontroller controls a digital potentiometer which is seen by the DDS as an external resistor defining the output swing of the DAC.

The two graphs in figure 5.4 characterize the performance of the signal generation. They show the power spectra of the analog output after the low-pass filter at 1 MHz and 20 MHz, respectively. From this measurement, the total harmonic distortion (THD) of the signal is found to be -48.8 dB at f_m = 1 MHz and -55.2 dB at f_m = 20 MHz.

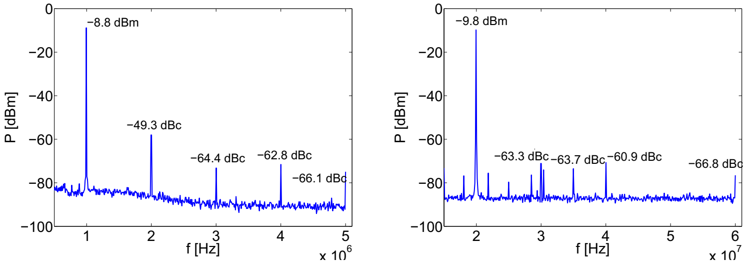

Figure 5.4: Performance of the DDS circuitry. Frequency spectra at signal frequencies of 1 MHz (*left*) and 20 MHz (*right*), showing the power levels of the harmonics relative to the carrier.

In section 5.1.1, the idea of routing a trigger signal for phase reference from the signal generation to the signal processing unit was introduced to avoid the need for a second ADC channel. On the DDS demonstrator board, this task is accomplished by using an internal analog comparator inside the DDS circuit. The generation of the phase reference is illustrated in figure 5.5.

The comparator produces a rectangular signal at the signal frequency, which is fed to the clock input of a D-type flip-flop. The flip-flop can be activated at an arbitrary time instance by the microcontroller; its output signal will then be a rising edge occurring at the next clock edge after activation. Thus, the flip-flop output represents the phase of the analog signal (it will not necessarily occur of at the zero-crossings of the sinusoid due to internal delays, but will have a reproducible phase relation to the analog signal for each signal frequency) and can be used to trigger the acquisition of the ADCs.

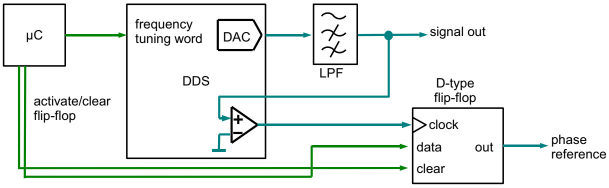

Figure 5.5: Generation of the analog modulation signal and a single edge at a zero-crossing for phase reference, controlled by a microcontroller (μC).

5.2.2 Conversion of the optical signals

The two fundamental characteristics of the analog-to-digital converters are the amplitude (bit) resolution and the sampling rate. With the desired frequency range between 20 kHz and 20 MHz, a sampling rate of 125 MS/s is a straight-forward choice which yields the same ratio between sampling rate and maximum frequency as for the signal generation. The integrated circuit used for conversion is a dual-channel ADC with a 14-bit amplitude resolution, which corresponds to a theoretical dynamic range of the input voltage swing of 84.3 dB; the data sheet claims the spurious-free dynamic range at 2.3 MHz input and a sampling clock of $f_s = 125$ MHz to be -86.5 dBc [58].

The demonstrator system setup comprises two evaluation boards from the manufacturer of the ADCs, hosting the dual-channel ADC together with the two corresponding analog input paths (which had to be modified in order to expand the frequency range down to the desired 20 kHz) as well as all electronics required for data acquisition. The evaluation boards contain an FPGA that acts as a FIFO buffer to gather the serial data from both channels of the ADC and then establishes a connection with the controlling computer to transfer the time-domain data via USB. With this configuration, a wave form of 2^{14} (16384) bits can be sampled; at $f_s = 125$ MHz, this corresponds to a time frame of 131.072 μs.

Figure 5.6 shows temporal sections from wave forms acquired by the setup at $f_m = 100$ kHz and $f_m = 10$ MHz from a fiber of $L = 2250$ m; the offset between the lasers' frequencies is $\Delta f \approx f_B$.

While the reference signal remains constant in amplitude over the frequency sweep, the requirement on the dynamic range of the receiving circuitry for the backscattered Stokes signal becomes obvious from the figure. From this measurement, a ratio between the signals' voltage amplitudes at the two displayed frequencies of about -20 dB can be read. At the poor level of the input signal relative to the ADCs' full input scale, the level of the received 10 MHz signal becomes -60 dBfs (logarithmic level relative to full scale), which still does not challenge the dynamic range of the converters.

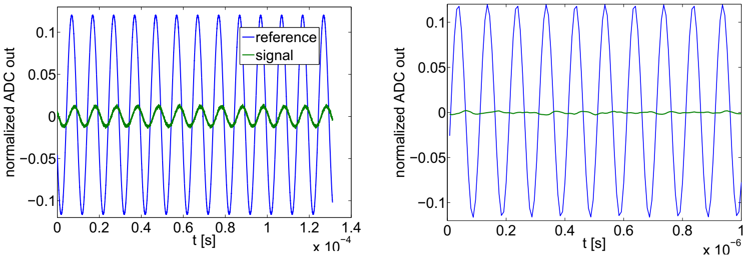

Figure 5.6: Digitally acquired data by means of the setup from figure 5.1 at signal frequencies of 100 kHz (*left*) and 10 MHz (*right*). The amplitudes of the wave forms are normalized to full input scale of the ADC.

5.2.3 Signal processing

For each sweep value of f_m and each laser frequency offset Δf, the two time domain wave forms (signal and reference) are acquired over the fix time frame and transferred to the signal processing unit; in the demonstrator setup using the ANALOG DEVICES evaluation boards, this is done via an USB interface to the laboratory computer, where all further signal processing is performed off-line. In order to compare the amplitudes and phases of each signal pair to construct the transfer function, a Fourier transform is performed on the wave forms. The discrete form of the Fourier transform connects a time domain series $x(n)$ to its discrete frequency spectrum $X(m)$ by

$$X(m) = \sum_{n=0}^{N-1} x(n) e^{-j2\pi nm/N} \tag{5.1}$$

with N being the total number of samples in the time domain. In this transformation, the spectral components of $x(n)$ are represented in N analysis frequencies:

$$f_{\text{analysis}}(m) = \frac{m f_s}{N} \tag{5.2}$$

With $f_s = 125$ MHz and $N = 2^{14}$, the analysis frequencies (also called the DFT bins) are spaced by 7.63 kHz. From this, the problem of DFT leakage becomes obvious: If the signal frequency f_m does not exactly coincide with an analysis frequency, the spectral power of the desired frequency component will be distributed over the adjacent bins, resulting in an error in the magnitude and phase measurement [59]. For measurements with the BOFDA setup as described in chapter 4, this is not a crucial issue, because – with the demand on the system to be linear – this error will equally occur in both the transformation of the reference and the received signal (and, moreover, in the calibration measurement). Nevertheless, the problem is avoidable by adapting the number of samples for each f_m value such that each sampled data frame of length $N\left(f_m\right)/f_s$ comprises an integer number of periods of the sampled wave form. The condition for the number of samples is

$$\left.\begin{array}{rl} N\left(f_m\right) = & k \cdot \dfrac{f_s}{f_m} \\ N\left(f_m\right) \leq & N_{max} \end{array}\right\} \qquad N\left(f_m\right),\ k \in \mathbb{N} \tag{5.3}$$

with N_{max} being the maximum sampling length of 2^{14}. For each f_m value, the first $N\left(f_m\right)$ samples are fed into the FFT[1]. Examples of the results of the Fourier transform (which is performed by MATLAB's FFT algorithm) are given in figure 5.7 for the wave forms from figure 5.6.

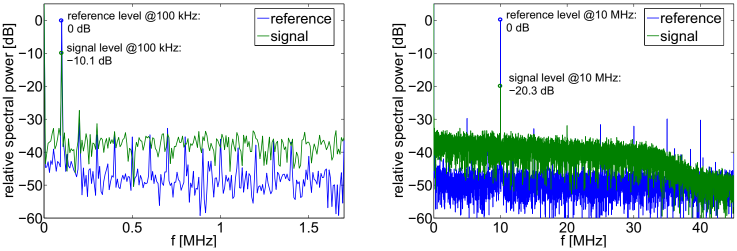

Figure 5.7: Spectral analysis of the digitally acquired data: Signal frequencies are 100 kHz (*left*) and 10 MHz (*right*).

In both the 100 kHz and the 10 MHz measurement, the spectral peak at f_m governs the frequency range. The task is now to cut out the $X(m)$ values for each signal pair that corresponds to the current sweep value f_m. The index m that indicates the DFT bin in question is found by simply allocating $m = f_m N/f_s$. The amplitude and phase values at this index then represent the integral of the whole frequency width of the indexed bin; this corresponds exactly to the IF filter bandwidth in the analog network analyzer. The bandwidth of a DFT bin is given by

$$\mathrm{BW} = \frac{f_s}{N} \tag{5.4}$$

and would be 7.63 kHz for $N = N_{max}$. For the adaptive sample length following condition (5.3), 7.63 kHz $<$ BW $<$ 10 kHz (in the case of modulation frequencies being multiples of 20 kHz) and decreases with longer time frames N/f_s for wave form sampling. As in VNA measurements, the choice of the filter bandwidth requires a trade-off between the signal quality (or noise impact) and data acquisition time.

---

[1] In an embedded implementation, this is not feasible, since the FFT loses its efficiency if not performed on a number of samples 2^M, $M \in \mathbb{N}$. Here, an adaptive sampling rate would be more adequate to avoid leakage.

The procedure is performed for each modulation frequency at each laser frequency offset, yielding $H(j\omega, \Delta f)$. From here on, the data can be fed into the final processing that converts the transfer function into the temporal pulse response and finally into the spatially resolved strain profile (see section 3.2).

If now the alternative configuration for the phase reference signal – using the internally created edge at a reproducible phase value of the signal to trigger data acquisition – is employed, only the wave form of the received backscattered signal is available. The left-hand graph in figure 5.8 shows a time domain wave form at $f_m = 200$ kHz with the trigger signal that is initiated every 1 μs by the microcontroller; the positive edge emerges from the D-type flip-flop at ever the same phase value of the sine wave.

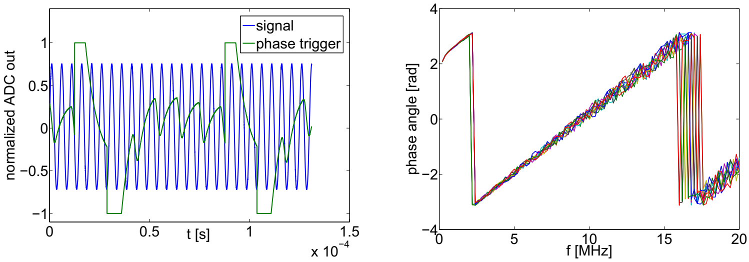

Figure 5.8: Creating the phase reference by a trigger signal. *Left:* A 200 kHz wave form with the trigger signal. *Right:* Ten successive measurements of a phase response over an f_m sweep.

The original concept was to trigger the FIFO buffer by this edge to start the acquisition of the wave form. Since the trigger interface of the FPGA board can not be accessed externally, the constantly acquired wave form was cut off in off-line processing so that only from the instant of the rising edge (detected on the second ADC channel) the time domain samples were used, thus starting at a reproducible phase position within the sine wave. The phase value of the designated DFT bin is then directly used as the phase angle within $H(j\omega, \Delta f)$.

The accuracy of the phase measurement when the electrical signal is used as a reference on the second ADC channel is only degraded by quantization noise (for the reference signal, in ten successive measurements a phase uncertainty of $\Delta\varphi < 0.2°$ was observed). In contrast, the concept of the phase trigger has proven to suffer from a dramatically higher phase uncertainty. From the block diagram in figure 5.5, the problem can be derived: Even though the trigger edge is set by the analog comparator of the DDS and is therefore of absolute accuracy, the triggering of the data acquisition (or cutting-off of the wave form) is forced to occur only within the fixed grid of the system clock at $f_s = 125$ MHz. The uncertainty of the configuration is

$$\Delta\varphi = 2\pi \frac{f_m}{f_s} \tag{5.5}$$

This means, that for $f_s = 125$ MHz and $f_m = 20$ MHz, the phase uncertainty becomes $\Delta\varphi = 57.6°$. The right-hand graph in figure 5.5 shows ten successive measurements of the phase response derived by the above method; a dramatic phase uncertainty increasing with higher f_m values is evident. In these measurements, an uncertainty of 57.0° was observed. As a conclusion, it must be stated that the phase trigger – although it provides a reliable reference – is not feasible in this setup, in which the signal generation and signal processing are performed in separate processing units.

5.3 Performance of the digital demonstrator setup

A distributed measurement on a defined profile of longitudinal strain applied to an optical fiber is shown in figure 5.9. Prior to the 200 m strain profile, an unstrained fiber with a length of 170 m was placed, resulting in a total measurement length of $L = 370$ m. The measurement parameters are chosen for a maximum measurement length of 500 m and a spatial resolution of 5 m, resulting in $f_{min} = 200$ kHz and $f_{max} = 20$ MHz. The measurement was performed with the digital setup from figure 5.1, using the electrical modulation signal as the reference on the second channel of the ADC (no scrambling of the polarization). It is shown in comparison to a conventional measurement performed with the analog VNA setup using the same measurement parameters.

The comparison shows that there is no degradation whatsoever in the digital measurement when it is matched with the conventionally acquired trace. All sections of alternating strain within the profile have been captured by both measurements with equal accuracy; the small section at $z = 225$ m, that has a length in the range of 1 m, was not detected by either measurement, as it had to be expected due to the spatial resolution of 5 m.

The demonstrator board for the digital determination of the transfer function for the Brillouin frequency domain analysis proves the feasibility of the concept. It should be seen as the half-way step towards a complete implementation of the overall system on an embedded hardware, which will contain the f_m generation and its gain block for driving the modulator as well as the receiving amplifiers after the photodiodes and the ADCs with all the signal processing on one single board. Ideally, all digital signal generation and processing will be embedded into a field-programmable gate array (FPGA)[2].

Considering this degree of integration, the question whether the reference signal should be obtained from a second photoreceiver, an electrical path via a second ADC channel or internally from the numerically generated synthetic signal itself, will arise

---

[2] By the time of writing, an FPGA design is in the state of hardware selection and rough conception of algorithms and implementation.

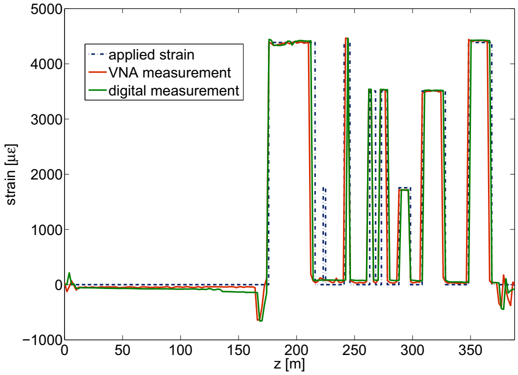

Figure 5.9: Distributed measurement on a defined strain profile, comparing the performance of the analog and the digital setup.

once more: If the DDS is implemented on the FPGA together with the processing of the received signals, the phase error from (5.5) will not occur; as in the considerations above, the second ADC channel could be saved. On the other hand, the calibration procedure will always require a modification of the optical signal paths (the reference signal and the backscattered signal have to be swapped at the input of the photoreceiver). In the laboratory, this requires merely changing the fiber connectors manually; for the implementation of a commercial measurement unit, a opto-mechanical switch would be necessary to perform this task. A decision whether the extra effort of such a delicate component is worth the benefit of saving the detector and converter path for the reference signal is difficult to take and will require further empirical investigations.

For now, the demonstrator represents the optimum setup for the case of separate processing units for signal generation and acquisition; using the direct electrical reference, the overall concept proves the efficiency of replacing the VNA by state-of-the-art digital circuitry.

CHAPTER 6

Limitations of spatial resolution

Even if the special application of dike monitoring – which the investigations of this work were aimed at – does not require a spatial resolution much below a few meters, it is easy to imagine that a large field of new applications would open up if the spatial resolution could be substantially improved, possibly to enter the centimeter range. It has been shown in section 3.2 (with the essential relation from equation (3.11)), that the spatial resolution of the BOFDA system directly corresponds to the sweep range of the modulation frequency ($f_{max} - f_{min}$). Figure 6.1 illustrates the enhancement of the measurement by increasing the sweep range of f_m.

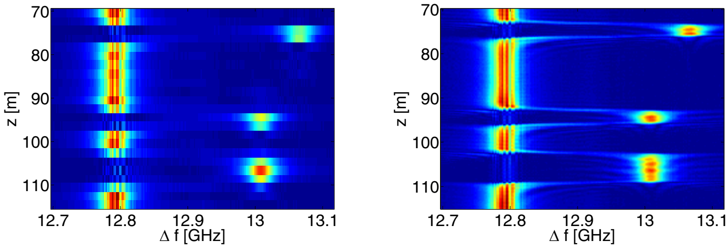

Figure 6.1: Close-up of the spatially resolved Brillouin gain $h(z, \Delta f)$ of a defined strain profile. *Left:* $f_{max} = 20$ MHz (spatial resolution: 5 m). *Right:* $f_{max} = 120$ MHz (spatial resolution: 0.83 m).

At an upper limit for the modulation frequency $f_{max} = 120$ MHz, the spatial resolution already lies below 1 m; the question why we don't simply modulate up to the gigahertz range seems reasonable, just as it would be a straight-forward approach to shorten the pulses in the BOTDA technique (see section 3.1 for this parallelism).

There are several difficulties to be met when the pump beam is modulated with ever higher frequencies in order to achieve higher spatial resolution. The generation and processing of the base-band signal puts high demands on the signal sources, the electro-optic components and all processing electronics. Especially the dynamic range of the photoreceivers is challenged, since the backscattered signal becomes very weak at high frequencies; sophisticated filter techniques are required to distinguish the backscattered signal from the noise floor.

In contrast to these problems that are of a rather technological nature – which implies that they might be solved by means of advanced measurement equipment – there is one phenomenon which apparently introduces a kind of uncertainty relation to the measurements: With increasing spatial resolution, a simultaneous decrease of resolution of the measurand f_B can be observed. This relation appears as a fundamental and unconditional limitation to the attempt to perform distributed measurements of arbitrary precision.

Figure 6.2 shows the occurrence of this phenomenon within the spatially resolved measurement from figure 6.1.

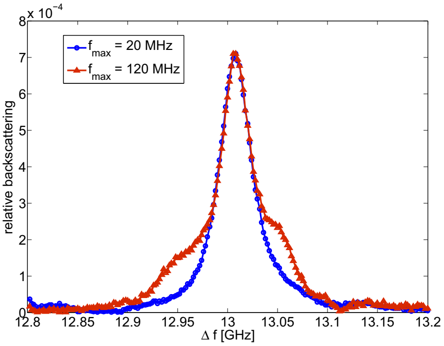

Figure 6.2: Cross-section through the Brillouin gain spectra from figure 6.1: $h(z = 144\text{ m}, \Delta f)$, showing the artifacts that arise at high modulation frequencies.

While the measurement with a sweep range up to 20 MHz shows a clean Lorentzian spectrum, strong artifacts appear on either slopes of the curve obtained from the 120 MHz measurement. Although the peak of the spectrum remains unmodified, these artifacts will degrade the performance of a curve-fitting procedure and thereby add an uncertainty to the determination of the measurand f_B for each spatially resolved measurement point in $h(z, \Delta f)$. It can be shown that the artifacts increase with higher values for f_{max}; their occurrence begins when f_{max} passes the range of the Brillouin linewidth of $\delta f_B \approx 35$ MHz.

The artifacts are no phenomenon solely inherent to measurements in the frequency domain, and the uncertainty relation of spatial and measurand resolution is no specific problem of the BOFDA system: At high spatial resolutions, equivalent artifacts are observed when pulse reflectometry measurements are performed [60], [61]. It was generally agreed for several years that with this broadening of the Brillouin gain spectra, the spatial resolution of the BOTDA system would remain limited to about 1 m, just as well as the BOFDA system.

Step by step, a theoretical approach has been presented that accounts for the broadening of Brillouin gain spectra at short pulses [62], [63], the phenomenon as it occurs in the time domain. From these analyses (they will be briefly summarized in section 6.1.4), the mechanisms in the frequency domain are not directly evident. For the frequency domain analysis, the group of Romeo Bernini, Aldo Minardo and Luigi Zeni has presented a theoretical model of the problem [64], [54]. They numerically solved the three differential equations of stimulated Brillouin scattering, presuming the superposition of CW and AC components for the pump, Stokes and acoustic wave. This model leads to an explanation of phantom gain spectra (the phenomenon that will be derived within this chapter) by means of mutual interaction of the light waves with an intensity-modulated acoustic wave.

In the following sections, a thorough analysis of the problem is given – focusing on a more physical explanation for the occurrences. In contrast to the model of Bernini *et al.*, this approach avoids the presumption that the acoustic wave is modulated in its intensity at modulation frequencies that exceed the Brillouin linewidth ($f_m > \delta f_B$). Since the Lorentzian shape of the Brillouin gain spectra bases on the finite phonon lifetime and thereby introduces an upper cut-off frequency for the excitation of the acoustic wave, the inclusion of AC components for all of the three waves involved in the process brings some difficulties. The central physical presumption of the analysis that will be presented here avoids this dilemma by considering the spectral components of the optical beat pattern separately. The beat pattern (or, more precisely, its envelope function) excites the acoustic wave by means of electrostriction; each of its several spectral components can be seen as a continuously present periodical intensity pattern. Thereby, this chapter explains the occurrence of the degrading artifacts while fully retaining the harmonic analysis of stimulated Brillouin scattering from section 2.1.2.

The analysis aims not only at the full understanding of the phenomenon that sets such a tough limitation to the performance of the sensing system: its definite goal is the proposal of an analytical method to overcome the limitation. Section 6.2 contains such a proposal, which shows clearly that the approaches in the frequency domain have to be essentially different from any method that might be applicable in the time domain. The reconstruction technique which will be presented as a result of this chapter points out a systematical advantage of the frequency domain analysis over the pulse reflectometry with respect to the potential of error correction basing on physical modeling.

6.1 Theoretical analysis of the problem

The investigations of the mechanisms that are involved in stimulated Brillouin scattering have been presented in section 2.1.2. They led to a spectral representation of the interaction: Two optical frequencies with an offset Δf superpose to a beat pattern, the envelope of which has a frequency in the range of an acoustic wave in the medium. Due to the nonlinear nature of the interaction – formulated in equation (2.15) – frequency mixing occurs, and a wide-spread spectrum (of which the beat pattern of the intensities consists) can be determined.

For the measurement of the Brillouin gain spectra, a defined single spectral line of the beat pattern within the range to excite the acoustic wave is required. This presumes the existence of only two optical frequencies with narrow linewidth. For continuous-wave measurements with laser sources of considerable spectral purity, this assumption is valid; however, no spatially resolved measurements are possible with continuous wave pump and Stokes beams. Therefore, the impact of sinusoidally modulated amplitudes of the optical waves on the nonlinear interaction has to be investigated.

6.1.1 Amplitude modulation

The amplitude modulation (AM) technique as it is employed in the BOFDA system can be described as a multiplication of an (optical) carrier wave at the frequency ω_c and amplitude E_0 with a sinusoidal signal of the amplitude u_m, an offset (or DC component) A and the frequency ω_m (with $f_m = \omega_m/2\pi$) [65].

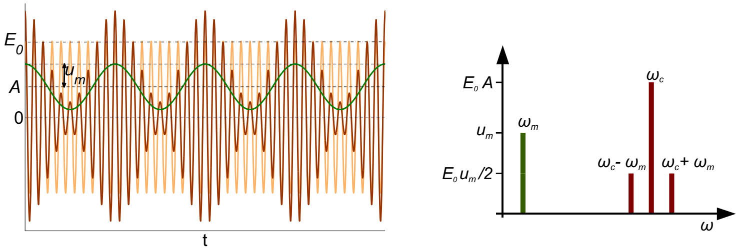

Figure 6.3: Amplitude modulation: A sinusoidal carrier signal is multiplied by a sinusoidal signal of lower frequency. *Left:* modulation in the time domain; *Right:* resulting frequency spectrum

The modulation is performed by a $LiNbO_3$ (lithium niobate) crystal Mach-Zehnder modulator, with the operating point (which, in practice, corresponds to the DC component A) set in the linear region of its cosine-shaped transfer characteristic. With the assumption of a stable operating point and a small modulating signal u_m, the multiplication can be considered to be linear, resulting in a double-sideband full-carrier amplitude modulation:

$$E_{mod}(t) = \frac{1}{2}\left(E_0 e^{j\omega_c t} + E_0^* e^{-j\omega_c t}\right) \cdot \left(A + \frac{u_m}{2}\left(e^{j\omega_m t} + e^{-j\omega_m t}\right)\right) \tag{6.1}$$

In figure 6.3, this process is depicted both in the time domain and in the frequency domain, illustrating the relation of A and u_m within the modulation process. At this point, it is convenient to introduce the modulation index (or modulation depth) $m = u_m/A$. The resulting frequency spectrum can be easily represented by expanding equation (6.1):

$$\begin{aligned} E_{mod}(t) = &\frac{E_0}{2}\left(A\, e^{j\omega_c t} + \frac{m}{2}A\, e^{j(\omega_c-\omega_m)t} + \frac{m}{2}A\, e^{j(\omega_c+\omega_m)t}\right) \\ + &\frac{E_0^*}{2}\left(A\, e^{-j\omega_c t} + \frac{m}{2}A\, e^{-j(\omega_c-\omega_m)t} + \frac{m}{2}A\, e^{-j(\omega_c+\omega_m)t}\right) \end{aligned} \tag{6.2}$$

where the spectral composition of the modulated signal becomes clearly visible, consisting of the carrier with amplitude A and the sidebands with amplitude $(m/2\ A)$ each, spaced from the carrier by ω_m. Figure 6.3 gives a schematic representation of the spectral lines.

6.1.2 SBS interaction with sinusoidally modulated intensities

In section 2.1.2, it was stated that the acoustic wave is excited by the envelope of the beat pattern, formed by the intensity of the two superposing optical fields $\vec{E}_p$ and $\vec{E}_s$. For optical signals of a single frequency, the forming of the beat pattern was formulated in equation (2.15); after expansion, a single spectral component

$$-k_0^2 E_p E_s^* e^{j(\omega_0 t - k_0 z)}$$

was found in the spectral range that is relevant for Brillouin interaction (with the complete calculation in appendix B.1).

Now, in the case of modulated signals, this analysis needs a revision. The spectral components $\vec{E}_p$ and $\vec{E}_s$ shall again enter (2.15); now, both of them being modulated, thus consisting of the three spectral lines from equation (6.2). The spectral composition according to (6.2) can be formulated in dependence of the modulation parameters: The offset (and, as a result, the weighting of the carrier amplitude) A_p for the pump and A_s for the Stokes light, and the modulation index m_p for the pump and m_s for the Stokes light. In the BOFDA configuration that has been used throughout the research, the pump beam is modulated by the intensity modulator; both A_p and m_p can be adjusted by setting u_m and the bias point of the device.

The spectral components of the Stokes beam are more complicated to determine: Since the Stokes light enters the fiber as a continuous wave, no sidebands are present in the initial state. Only if interaction with the modulated pump beam occurs, the Stokes beam will inherit the intensity modulation of the pump light. The modulation index m_s as well as the amplitude of the carrier A_s will represent the quantity of interaction – depending on the interaction length, relative states of polarization and the frequency detuning $\Delta f - f_B$. The parameters m_s and A_s are undetermined quantities within the measurement system.

With the frequency spacing from (6.2), the following denominations are introduced for each point of the sweep of the modulation frequency $\omega_m = 2\pi f_m$:

ω_{pc}	carrier of the pump wave
$\omega_{p1} = \omega_{pc} - \omega_m$	lower sideband of the pump wave
$\omega_{p2} = \omega_{pc} + \omega_m$	upper sideband of the pump wave
ω_{sc}	carrier of the Stokes wave
$\omega_{s1} = \omega_{sc} - \omega_m$	lower sideband of the Stokes wave
$\omega_{s2} = \omega_{sc} + \omega_m$	upper sideband of the Stokes wave

For the complete wave ansatz, the corresponding wave numbers for the pump carrier and sidebands k_{pc}, k_{p1} and k_{p2} and the Stokes carrier and sidebands k_{sc}, k_{s1} and k_{s2} are introduced.

The modulated fields $\vec{E}_p$ and $\vec{E}_s$, formulated according to (6.2), are introduced into equation (2.12), giving the excitation of the acoustic wave:

$$\begin{aligned}\nabla^2\left(\vec{E}^2\right) = \frac{\partial^2}{\partial z^2}\Bigg(& E_p A_p \left[e^{j(\omega_{pc}t - k_{pc}z)} + \frac{m_p}{2}\left(e^{j(\omega_{p1}t - k_{p1}z)} + e^{j(\omega_{p2}t - k_{p2}z)}\right)\right] \\ & + E_p^* A_p \left[e^{-j(\omega_{pc}t - k_{pc}z)} + \frac{m_p}{2}\left(e^{-j(\omega_{p1}t - k_{p1}z)} + e^{-j(\omega_{p2}t - k_{p2}z)}\right)\right] \\ & + E_s A_s \left[e^{j(\omega_{sc}t + k_{sc}z)} + \frac{m_s}{2}\left(e^{j(\omega_{s1}t + k_{sw}z)} + e^{j(\omega_{s2}t + k_{s2}z)}\right)\right] \\ & + E_s^* A_s \left[e^{-j(\omega_{sc}t + k_{sc}z)} + \frac{m_s}{2}\left(e^{-j(\omega_{s1}t + k_{s1}z)} + e^{-j(\omega_{s2}t + k_{s2}z)}\right)\right]\Bigg)^2\end{aligned} \tag{6.3}$$

The twelve summands contribute to a sum of 66 terms after expanding the quadratic expression. From these terms, the spectral distribution of the intensity beat pattern can be formed in analogy to B.1. All terms that contribute to the arithmetic mean – the DC terms without oscillating phases, being $\left|E_p^2\right|$ and $\left|E_s^2\right|$ – can be neglected.

The quadrature products $E_{px}^2 e^{2j(\omega_{px}t - k_{px}z)}$ and $E_{sx}^2 e^{2j(\omega_{sx}t + k_{sx}z)}$ with $x \in \{c, 1, 2\}$ have frequencies far above the optical band and do not contribute to the envelope of the beat pattern; they will be neglected in the following considerations. The same applies to all components with exponents $\pm j\left(\left(\omega_{px} + \omega_{sy}\right)t - \left(k_{px} - k_{sy}\right)z\right)$ with $[x, y] \in \{c, 1, 2\}$ which will be neglected as well.

All remaining terms bring the potential to fulfill equations (2.1) and (2.3), the conditions for the excitation of a viable acoustic wave. They are written as follows:

$$E_p E_s^* A_p A_s \cdot \left\{ \begin{array}{ll} & e^{j((\omega_{pc}-\omega_{sc})t-(k_{pc}+k_{sc})z)} \\ \frac{m_s}{2} & \cdot\, e^{j((\omega_{pc}-\omega_{s1})t-(k_{pc}+k_{s1})z)} \\ \frac{m_s}{2} & \cdot\, e^{j((\omega_{pc}-\omega_{s2})t-(k_{pc}+k_{s2})z)} \\ \frac{m_p}{2} & \cdot\, e^{j((\omega_{p1}-\omega_{sc})t-(k_{p1}+k_{sc})z)} \\ \frac{m_p m_s}{4} & \cdot\, e^{j((\omega_{p1}-\omega_{s1})t-(k_{p1}+k_{s1})z)} \\ \frac{m_p m_s}{4} & \cdot\, e^{j((\omega_{p1}-\omega_{s2})t-(k_{p1}+k_{s2})z)} \\ \frac{m_p}{2} & \cdot\, e^{j((\omega_{p2}-\omega_{sc})t-(k_{p2}+k_{sc})z)} \\ \frac{m_p m_s}{4} & \cdot\, e^{j((\omega_{p2}-\omega_{s1})t-(k_{p2}+k_{s1})z)} \\ \frac{m_p m_s}{4} & \cdot\, e^{j((\omega_{p2}-\omega_{s2})t-(k_{p2}+k_{s2})z)} \end{array} \right.$$

These are the frequency components that form the envelope of the beat pattern. By renaming the coinciding frequencies of the mixing products

$$\begin{aligned} &\omega_{pc}-\omega_{sc}=\omega_{p1}-\omega_{s1}=\omega_{p2}-\omega_{s2}=\omega_0 \\ &\omega_{pc}-\omega_{s1}=\omega_{p2}-\omega_{sc}=\omega_0+\omega_m \\ &\omega_{pc}-\omega_{s2}=\omega_{p1}-\omega_{sc}=\omega_0-\omega_m \\ &\omega_{p2}-\omega_{s1}=\omega_0+2\omega_m \\ &\omega_{p1}-\omega_{s2}=\omega_0-2\omega_m \end{aligned} \tag{6.4}$$

and by following the approximation from (2.3), so that $k_{pc} \approx k_{p1} \approx k_{p2} \approx k_{sc} \approx k_{s1} \approx k_{s2} = k_0/2$, the above terms can be combined to five spectral components of the beat pattern that have emerged from the superposition and quadrature of modulated $\vec{E}_p$ and $\vec{E}_s$.

These five components shall be expressed by the functions Φ_ξ with an enumeration index ξ for each spectral component:

$$\Phi_\xi = E_p E_s^* A_p A_s \cdot \left\{ \begin{array}{lll} \frac{m_p m_s}{4} & \cdot\, e^{j((\omega_0-2\omega_m)t-k_0 z)} & \xi=1 \\ \frac{m_p+m_s}{2} & \cdot\, e^{j((\omega_0-\omega_m)t-k_0 z)} & \xi=2 \\ \left(1+\frac{m_p m_s}{2}\right) & \cdot\, e^{j(\omega_0\cdot t)-k_0 z} & \xi=3 \\ \frac{m_p+m_s}{2} & \cdot\, e^{j((\omega_0+\omega_m)t)-k_0 z} & \xi=4 \\ \frac{m_p m_s}{4} & \cdot\, e^{j((\omega_0+2\omega_m)t)-k_0 z} & \xi=5 \end{array} \right. \tag{6.5}$$

The full expression for the envelope of the beat pattern thus becomes

$$E_{envelope} = \sum_{\xi=1}^{5} \Phi_\xi \tag{6.6}$$

For both the pump and the Stokes wave being modulated signals, the five equally spaced spectral lines of the envelope of the beat pattern are illustrated in figure 6.4 (to be compared with the single-frequency consideration from figure 2.3).

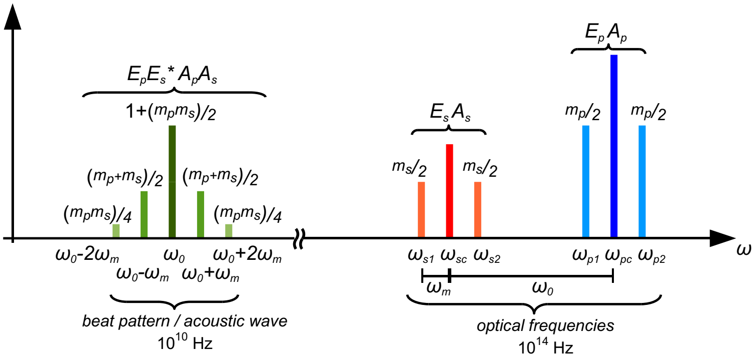

Figure 6.4: Spectral lines of SBS interaction in the case of a modulated pump beam.

As stated earlier, the modulation of the pump and the Stokes wave do not share the same physical origins: While the modulation of $\vec{E}_p$ is performed by the Mach-Zehnder modulator, with determined parameters A_p and m_p, the modulation of $\vec{E}_s$ is entirely dependent on the occurrence of Brillouin interaction. The consequence of this discrepancy for the spectral composition of the sidebands is the following: The central line $\Phi_{\xi=3}$ with frequency ω_0 and relative amplitude $1 + m_pm_s/2$ (when normalized to $E_pE_s^*A_pAs$) is little affected by changes in the modulation index of either of the two waves. The two sidebands $\Phi_{\xi=2,4}$ at $\omega_0 \pm \omega_m$ with relative amplitudes $(m_p + m_s)/2$ are governed by the defined and constant modulation index of the pump wave m_p. An increase of the uncertain Stokes modulation would have some impact on their intensity, but if $E_s \ll E_p$ and $m_s \ll m_p$ is assumed, these sidebands can be assumed to be ever-present and constant over the interaction length. In contrast, the outer sidebands $\Phi_{\xi=1,5}$ at $\omega_0 \pm 2\omega_m$ with relative amplitudes $m_pm_s/4$ depend on the presence of Brillouin interaction in their mere existence; they are expected to be very weak, even if the Stokes modulation index m_s reaches the quantity of m_p.

The splitting of the envelope of the beat pattern into five spectral lines has a considerable impact on measurements of the Brillouin gain – in fact, the artifacts shown in figure 6.2 can be traced back to exactly this phenomenon.

6.1.3 BOFDA measurements at high modulation frequencies

In the BOFDA measurement setup from chapter 4, maximum Brillouin gain is measured when the laser detuning Δf matches the specific Brillouin frequency f_B corresponding to strain, temperature and material parameters of the fiber. In terms of the relations (2.4) and (2.5), interaction will occur whenever (within the sweep of Δf)

the resonance condition $\omega_0 = \omega_a$ is fulfilled. If now several fiber sections with distinct values of f_B are present within the measured fiber, there will be several superposed spectra to be observed when a sweep of Δf is performed. Each of the maxima of Brillouin gain corresponds to a value of Δf that leads to the excitation of an acoustic wave.

Such a direct reallocation of the measured gain maximum presumes a single frequency component of the envelope for each value of Δf. However, as it just has been shown, this is not the case when the pump beam is modulated, since three (if we assume the Stokes modulation to be weak) frequency components of the beat pattern are ready to excite the acoustic wave, leading to stimulated backscattering. When sweeping Δf, the interaction will be excited by one spectral line after the other: Not only the occurrence of $\omega_0 = \omega_a$, but also $\omega_0 \pm \omega_m = \omega_a$ (in spite of $\Delta f \neq f_B$) will lead to Brillouin interaction. This undesired excitation will occur for any value of f_B that is present in the fiber.

The actually existing gain spectra in a fiber have the shape of a Lorentz curve (equation (2.20)). They correspond to a certain value of f_B that appears at an arbitrary location along the fiber. The gain function $g_B(\Delta f)$ is the superposition of all spectra that correspond to the several f_B values that are present in the fiber. The sweep of Δf is performed to measure g_B. Ideally, a single line in the frequency spectrum of the envelope scans the gain function $g_B(\Delta f)$, exciting the acoustic wave whenever the condition is fulfilled. With modulated optical signals, the excitation can no longer be considered a single peak. With the expression for the spectral components of the beat pattern's envelope (with three spectral lines that depend on f_m), the scan must be formulated as a convolution of g_B with the excitation pattern from (6.5):

$$g'(\Delta f, f_m) = g(\Delta f) * \sum \Phi_\xi \tag{6.7}$$

with $\xi = 2, 3, 4$ if the outer spectral components are neglected (which will be discussed below).

In section 3.2, the two sweeps that have to be performed to obtain the transfer function $H(j\omega, \Delta f)$ were treated separately. From the considerations above it becomes clear that this independence of the sweeps of the modulation frequency f_m and the laser frequency offset Δf is no longer valid at high modulation frequencies: When f_m becomes larger than the width of the Brillouin gain spectra δf_B, reallocation of the measured gain spectra to their origin in a physically present value for f_B might not be unambiguously possible.

In the following, two measurements on fibers of one single section of homogeneous strain, temperature and material parameters are presented. Corresponding to the principle of the frequency domain analysis, both the pump modulation frequency f_m and the laser frequency offset Δf were swept and the complex transfer function for each Δf was recorded. For such a homogeneous fiber, a single Brillouin gain spectrum around $\Delta f = 12.79$ GHz is expected, with an intensity decreasing towards higher modulation frequencies.

From the first measurement, performed on a fiber of a length of 4400 m, cross-sections of the Brillouin gain spectra are shown in figure 6.5. In opposition to the expected single central gain spectrum, figure 6.5 shows the artifacts that arise from the convolution with the three-peaked excitation from (6.7): Brillouin interaction is not only excited for $\Delta f = f_B$, but any time one of the spectral lines of the beat pattern enters the area of resonance, which occurs at $\Delta f = f_B - f_m$ as well as $\Delta f = f_B + f_m$. As a consequence, phantom gain spectra emerge at a definite spacing corresponding to the modulation frequency f_m from the actually present Brillouin gain spectra.

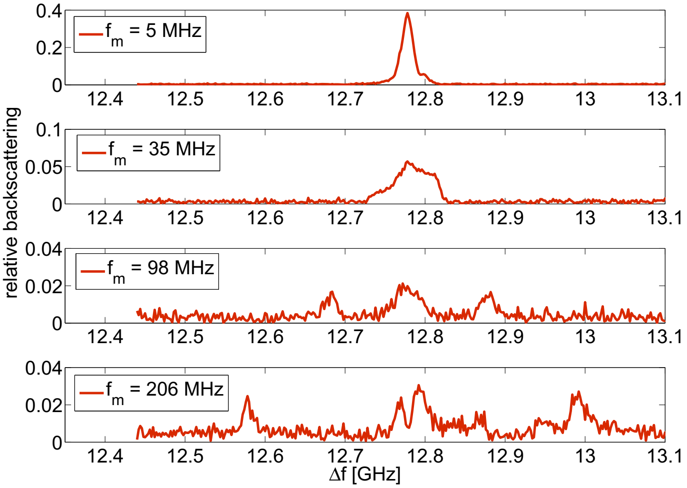

Figure 6.5: Brillouin gain spectra $g'(\Delta f, f_m)$ of a homogeneously strained fiber (4400 m) at different modulation frequencies.

In such a measurement of a homogeneously strained fiber, no interaction is detectable at the spectral locations of the outer beat components $\Phi_{\xi=1,5}$ with $f_B \pm 2f_m$. These components will only appear if any Brillouin interaction is already occurring with one of the existing spectral components $\xi = 2, 3, 4$. Consequently, measurable Brillouin scattering due to the outer sidebands requires the presence of fiber sections with values for f_B corresponding to one of the three central components – to initiate $m_s > 0$ – and, simultaneously, some fiber section with f_B corresponding to the outer sidebands. Therefore, with a sweep of f_m, even in the case of multiple fiber sections of randomly distributed values for f_B, the outer spectral lines will not contribute with continuously emerging phantom spectra at $f_B \pm 2f_m$; they will rather show sporadical appearances at low intensity levels, which will be (at this stage of the investigations) considered as noise.

Figure 6.6 shows the second of these measurements: a 2200 m long fiber of homogeneous temperature and strain, where no local changes of f_B are present. The measurement trace shows a logarithmic representation of the transfer function with a sweep range of f_m from 40 kHz to 120 MHz.

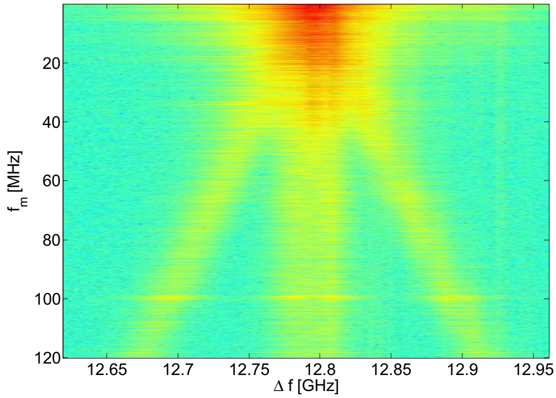

Figure 6.6: Magnitude of the transfer function $H(j\omega, \Delta f)$ of a 2200 m unstrained fiber.

A more quantitative analysis of the measurement shown in 6.6 is carried out in order to investigate the correspondence of the measured shape of the spectra with the theoretically predicted interaction. For this purpose, the parameters of the amplitude modulation of the pump beam have to be taken into account. The $LiNbO_3$ modulator was driven by the signal source of the VNA at a maximum signal power of 15 dBm, which provides a signal with a peak-to-peak voltage of 3.55 V at the electrodes of the Mach-Zehnder element. This drive voltage lies well below the modulator's V_Π and thereby provides roughly linear operation.

From the modulated signal monitored at a photodetector, the actual optical AM parameters can be derived with an oscilloscope or spectrum analyzer, yielding an offset of $A_p = 0.6$ V at an optical power that gives a signal of $u_p = 0.46$ V peak-to-peak at the output of the internal amplifier of the photodetector. The modulation index of the pump signal becomes $m_p = 0.77$.

An average value for the ratio of the intensities of central and phantom spectra can be drawn from the measurement shown in figure 6.6. Between $f_m = 50$ MHz and $f_m = 120$ MHz, the region where the phantom spectra are distinguishable from the central spectrum, an average ratio between the phantom excited by the lower sideband to the central spectrum of 0.59 is measured, for the spectrum excited by the upper sideband it is 0.61.

The ratio of the spectral intensities of the phantom spectra to the central spectrum according to equation (6.5) is

$$\frac{\Phi_{\xi=2,4}}{\Phi_{\xi=3}} = \frac{(m_p + m_s)/2}{1 + (m_p \cdot m_s)/2}$$

With the phantom spectra emerging at a defined distance from the physically relevant gain spectra, the impact of the modulated pump signal on the measured transfer function becomes analytically comprehensible and predictable. For a final result of the distributed measurement, the measured traces for $H(j\omega, \Delta f)$ are transformed back into the time domain to retrieve $h(t, \Delta f)$ and thus the spatially resolved Brillouin gain distribution $h(z, \Delta f)$. For this final measurement result, the analytical predictability of the artifacts is lost: Each spatial point is reconstructed from the entire transfer function, i.e. each sample point of f_m might contribute to any point in the spatially resolved trace. The result of this defective reconstruction, in which the phantom spectra contribute just as well as the physically relevant spectra do, has been shown in figure 6.2 at the beginning of this chapter. Higher modulation frequencies enhance spatial resolution, but they are also responsible for a certain broadening of the spatially resolved gain spectra. Naturally, artifacts become stronger at sections with rapid changes of f_B, since they correspond to a spectral representation with a larger proportion of high frequencies in the transfer function.

The spectral broadening that is inherent to measurements using high modulation frequencies forms the uncertainty relation that limits the performance of the measurement system: High spatial resolution requires high modulation frequencies, which in turn produce the artifacts that decrease the accuracy of determining f_B – and thereby strain and temperature – along the fiber.

6.1.4 Analogy in time domain measurements

The broadening of the Brillouin gain spectra at high spatial resolution has been traced back to the physical description of stimulated Brillouin scattering. The explanation given in the preceding sections are valid for sinusoidally modulated light. The expansion of the analysis to other periodic signals is done straight-forward by introducing the required spectral components of any periodic waveform into equation (2.16) and expanding the quadrature term according to (6.3).

For pulsed signals – as they are employed in time-domain distributed measurements – things do not differ fundamentally from this harmonic view, but need to be approached differently if a closed description is to be found. Like in BOFDA measurements, a naïve view on the interaction implies that the excitation of the acoustic wave corresponds to a narrow spectral line in the frequency domain, formed by the envelope of the beat pattern. This line, corresponding to the spectral purity of the

CW Stokes beam and the pulsed pump beam, would scan the Brillouin gain spectrum when sweeping Δf.

This assumption will hold true as long as the pulses of the pump signal are long (>50 ns). When they enter the dimension of the phonon lifetime (≈ 9 ns), the optical spectrum of the pump pulses can no more be considered as a narrow line. Since the spectral width of a pulse is inversely proportional to its duration, it will scan the Brillouin gain curve with its entire spectrum. Thus, the measurement of the gain spectra again corresponds to a convolution of the spectral representation of the excitation (i.e. the pulse) and the actual Lorentzian gain curve [62], [63], just as it has been formulated in equation (6.7). Several experimental studies of the dependence between Brillouin spectra and pulse width have been published [61], containing a measured width of a Brillouin loss spectrum of 100 MHz (instead of the natural linewidth in silica of $\delta f_B \approx 35$ MHz) at a pulse duration of 5 ns (the pulse duration that would correspond to a spatial resolution of 0.5 m) [66].

The main discrepancy between the two cases with respect to the convolution is that in frequency domain measurements, the excitation can be formulated by summing up three narrow lines of defined spacing; in time domain measurements, the term that enters (6.7) instead of the sum of Φ_ξ is the continuous spectrum of the narrow pulse, which is Gaussian-shaped in case of Gaussian pulses and $\frac{\sin x}{x}$-shaped in case of rectangular pulses.

Then again, the two principles meet at this point – if the continuous frequency spectrum of the optical pulse is seen as an integration over all the spectral lines of the frequency sweep, just as the Fourier transform integrates over all frequency points of the transfer function in order to reconstruct the pulse response. Within the result of a distributed measurement – the spatially resolved pulse responses for each sweep value of Δf – the emerging artifacts are similar for both time domain and frequency domain measurements: At high spatial resolutions, the bandwidth of the excitation exceeds the resonance bandwidth of the acoustic wave, being the spectral width of the pulse in the BOTDA technique and the high values of f_m for the BOFDA technique. The spectral components forming the artifacts are excited one after another in form of phantom spectra when modulating with a sinusoidal signal (to be added up in the IFFT) – and, in contrast, are excited all at once if a narrow pulse is sent along the fiber in order to interact.

6.2 Reconstruction of Brillouin gain spectra at high spatial resolution

If the artifacts degrading any distributed Brillouin measurement are similar in both time domain and frequency domain measurements, what benefit should be drawn from the analysis from section 6.1, that has been specifically developed for the case of frequency domain measurements?

The value of the the analyses from section 6.1 emerges when considerations about a way to overcome the limitations in spatial resolution are commenced. Although the impact on the measurement signal is eventually the same for both BOTDA and BOFDA measurements, the distinction in the artifacts' origin offers different approaches to correct or avoid them. Approaches in the time domain have proven to be promising and will be briefly summarized in section 6.2.3. In the next two sections, a novel approach that takes full advantage of the unique characteristics of frequency domain measurements is presented.

6.2.1 Concept of deconvolution in the frequency domain

To overcome the limitations of spatial resolution, inherent to all Brillouin measurement systems, is a task that might generally be approached in two ways: Either the artifacts that degrade the measurement might be tried to be avoided as far as possible – or their emergence has to be accepted, in which case a subsequent correction or reconstruction would have to be attempted. During the progress of the research on the BOFDA system, avoidance of the artifacts has not appeared as a promising way; as it has been shown within the analysis of the problem, their emergence is intimately connected to the mere existence of modulated light within Brillouin interaction.

In order to find an approach for a correction of the degraded measurement traces, the frequency domain technique offers a starting point which pulse reflectometry does not provide. The key is the convolution from equation (6.7): For each value of f_m, the sweep of Δf excites not one Lorentzian spectrum for each f_B value, but a characteristic pattern of three spectra spaced by f_m. With the knowledge of the spectral shape of the beat pattern envelope (formulated in equation (6.5)), the pattern that will result from the convolution of each existing gain spectrum is determined and can be predicted. Each Brillouin shift f_B that is present in the fiber will correspond to a three-peaked pattern in the measured transfer function $H(j\omega, \Delta f)$, shaped in accordance to f_m. After transforming the transfer function into the pulse response, this clear reallocation is lost – which is the situation right after data acquisition in the BOTDA technique.

Therefore, the separate measurement of the frequency components that afterwards are recombined to the pulse response by the transformation might enable separate reconstruction of the gain spectra for each sweep value of f_m. From equation (6.7), the actual gain spectrum $g\,(\Delta f)$ has to be recovered; the measured spectrum $g'\,(\Delta f)$ is readily available, and the spectral components Φ_ξ have been derived (with an uncertainty concerning the impact of modulation of the Stokes beam and the presence of the outer components $\Phi_{\xi=1,5}$). Thus, an operation corresponding to an inverse convolution will reconstruct the original Brillouin gain spectra $g\,(\Delta f)$ for each sweep value of f_m. The approach is illustrated in figure 6.7.

This approach is not so different from the fitting procedure employed in all distributed Brillouin measurements (section 4.4). Within the measurement data, a defined pattern is searched for each value of f_m along the axis of Δf; in the standard procedure, this is a Lorentz function with a FWHM of the Brillouin linewidth, because it is known that each existing Brillouin shift f_B induces one Lorentzian shaped spectrum into the measurement trace. This pattern is now extended to the more com-

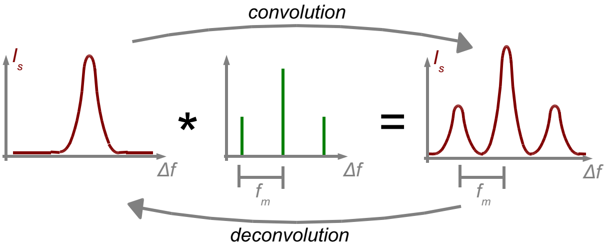

Figure 6.7: Illustration of the convolution of the Brillouin gain spectra $g\left(\Delta f\right)$ with the spectral representation of the excitation Φ_ξ, presuming the reversibility of convolution

plicated shape of the three-peaked spectrum, defined for each sweep value of f_m. For $f_m \ll 1/\tau_B$, i.e. as long as the modulation frequency remains far below the Brillouin linewidth, the three-peaked pattern merges into the single Lorentz spectrum which is searched for in the standard procedure.

The measurement shown in figure 6.6 illustrates the idea of the approach: If for each value of f_m (vertical axes) the three peaks are reallocated to the central peak, then reconstruction of $g\left(\Delta f\right)$ is achieved; the transfer function then consists of one single Lorentzian spectrum for each f_B and f_m, replacing the pattern that was degraded by phantom spectra. Naturally, the measurement from figure 6.6 does not show the real-life case of distributed sensing, as it was performed on an explicitly homogeneous fiber. In a fiber that comprises an arbitrary distribution of sections with different f_B, for each value of f_m, a superposition of several convolution patterns will be measured; their reallocation to the physical gain spectra $g\left(\Delta f\right)$ will not be manageable by visual estimation.

6.2.2 Use of algorithms from digital image processing

At this point, the processing of digital images enters the picture. Any recorded image is afflicted with both stochastic perturbations (noise) and systematical errors, the latter being caused, for instance, by physical properties of the lenses or inhomogeneities on the recording medium (the photographic film or the electronic sensor). Image degradation by such systematical errors can be formulated by the convolution

$$g'\left(x,y\right) = g\left(x,y\right) * d\left(x,y\right) + \eta\left(x,y\right) \tag{6.8}$$

where $g\left(x,y\right)$ is the undegraded image, $g'\left(x,y\right)$ is the degraded image, $d\left(x,y\right)$ is the degradation function which represents all systematical errors and $\eta\left(x,y\right)$ is additional noise [67]. In digital image processing, the degradation function $d\left(x,y\right)$ is usually referred to as the point spread function (PSF), since it represents the response of the image recording system for each recorded point in two dimensions. In the case of

Brillouin sensing, the problem is reduced to one dimension (the sweep of Δf instead of x, y).

The simplest approach

Since convolution turns into simple multiplication after Fourier transformation, the relation is transformed into the domain of a geometrical frequency ν and becomes[1]

$$G'(\nu) = G(\nu)\, D(\nu) + N(\nu) \tag{6.9}$$

with the transformation pairs $g(\Delta f) \bullet\!\!-\!\!\circ\, G(\nu)$ (original Brillouin gain spectrum), $g'(\Delta f) \bullet\!\!-\!\!\circ\, G'(\nu)$ (measured gain spectrum), $d(\Delta f) \bullet\!\!-\!\!\circ\, D(\nu)$ (degradation function or PSF) and $\eta(\Delta f) \bullet\!\!-\!\!\circ\, N(\nu)$ (additional noise). Equation (6.9) can be transposed towards $G(\nu)$ in order to obtain a restored (inversely convoluted) signal $G''(\nu)$:

$$G''(\nu) = G(\nu) + \frac{N(\nu)}{D(\nu)} = \frac{G'(\nu)}{D(\nu)} \tag{6.10}$$

Following a naïve approach, equation (6.10) forms a complete reconstruction directive for the Brillouin gain spectra degraded by phantom spectra. Since the PSF $d(\Delta f)$ is known within the uncertainties concerning the modulation of the Stokes light, inverse convolution can be performed by executing (6.10) and performing an inverse Fourier transform of $G''(\nu)$ back into the domain of Δf.

Unfortunately, there are two critical issues in this approach: First, $D(\nu)$ might contain zeros, which would induce singularities into the result of the division. The second problem is the existence of stochastic noise, which will still be present in the reconstructed spectrum $G''(\nu)$. Moreover, this noise will be amplified to an extreme extent by the unavoidable division by $D(\nu)$, which is a function decreasing towards high values of the geometrical frequency ν. If the operation in (6.8) is seen as a low-pass filtering of $g(x, y)$, then (6.10) must be considered as a high-pass, inflating η at high ν.

Deconvolution of complex data

Considering the measurement trace along the dimension of Δf, it is the magnitudes of the complex data that form the Brillouin gain spectra with their characteristic patterns of Lorentzian curves, actual and phantom spectra superposed; therefore, the degradation by convolution (and the corresponding PSF) were formulated as an analysis of the complex magnitudes. If the data along the dimension of f_m, forming the complex transfer functions $H(j\omega)|_{\Delta f}$, is considered, the question arises what impact the restoration process will have on the phase information. This component of the measurement data is crucial for reallocating the spatial information within the

---

[1] This is a transformation along the dimension Δf into a geometrical domain with the non-physical frequency variable ν, and not to be confused with the transformation along the f_m axis which converts the transfer function into the pulse response.

pulse response, whether the three-dimensional data along Δf and f_m is represented in Cartesian or polar coordinates.

If the restoration process is seen as an assignment of weights to the measurement points – i.e. the search for a weighting function $q = |g''| \,/\, |g'|$ that eliminates the phantom spectra for each f_m – it becomes clear that the phase information is not affected by the deconvolution procedure. Since the weighting by q is linear, its application has a simple impact on the real and imaginary part:

$$|g''| = q \cdot |g'| = \sqrt{\left(q \cdot \mathrm{Re}\left(g'\right)\right)^2 + \left(q \cdot \mathrm{Im}\left(g'\right)\right)^2} \tag{6.11}$$

Consequently, the weighting function q, once obtained for the magnitudes, can be applied to the real and imaginary parts of the measurement data g'. From these traces in Cartesian representation, the polar data (naturally with the magnitude $|g''|$) can be obtained with the adequate phase information to be fed into the inverse Fourier transform that will yield the spatially resolved pulse response.

Demonstration of different deconvolution procedures

In order to demonstrate effects of deconvolution, a cross-section of the measurement from figure 6.6 at 99.2 MHz is taken. The PSF is constructed according to section 6.1.3, with three Lorentzian spectra spaced by f_m; the height of the two side spectra relative to the central spectrum is set to 0.6, which is the value derived in 6.1.3. The measurement data with its central Lorentzian spectrum that corresponds to the actual value for f_B of the unstrained fiber[2] and the two phantom spectra together with the PSF are shown on the left of figure 6.8.

The result of the naïve deconvolution by simply dividing the Fourier transforms of the measured data and the PSF is shown on the right side of figure 6.8. Obviously, the Brillouin gain spectra are drowned entirely in the noise, extremely amplified as predicted from equation (6.10).

One of the oldest methods of image restauration which seeks an estimate g'' of the undegraded image g by performing the deconvolution of a point-spread function from a degraded image g' is the **Wiener deconvolution** technique [67]. It introduces an estimate of the signal-to-noise-ratio S_η / S_g of the degraded image, which is the power spectrum of the noise divided by the power spectrum of the undegraded image. For the restoration of the Brillouin gain spectra, the estimate g'' that minimizes the statistical error function

$$e^2 = E\left(\left(g\left(\Delta f\right) - g''\left(\Delta f\right)\right)^2\right) \tag{6.12}$$

---

[2] The gap in the measurement data at $\Delta f = f_B$ is a systematically occurring phenomenon in measurements of long fibers at high modulation frequencies; it can be spotted in both the measurement from figure 6.5 and the one from figure 6.6. Since it is not modeled by the analysis in this chapter, it should be subject of further research.

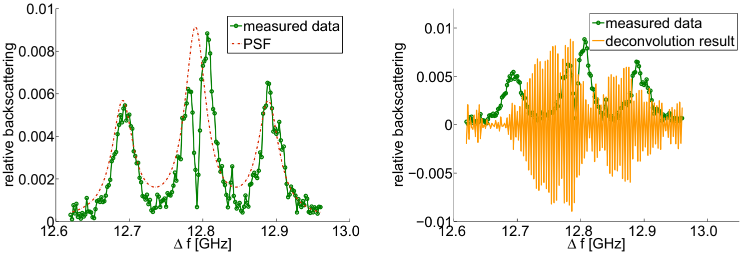

Figure 6.8: *Left:* Measured Brillouin gain spectrum of the 2200 m fiber at $f_m = 99$ MHz and the PSF. *Right:* Result from deconvolution by simply dividing the Fourier transforms of measured gain spectra and PSF.

is again obtained in the domain of the geometrical frequency ν:

$$G''(\nu) = \left(\frac{1}{D(\nu)} \cdot \frac{|D(\nu)|^2}{|D(\nu)|^2 + S_\eta(\nu)/S_g(\nu)} \right) G'(\nu) \tag{6.13}$$

An implementation of the Wiener algorithm is readily available in MATLAB. The main problem in employing this algorithm for the restoration is the lack of knowledge about the signal-to-noise-ration of the degraded image. Presuming $S_\eta(\nu)/S_g(\nu)$ to be constant over ν, the implementation can be used, interactively experimenting with scalar values for the noise impact. This will not lead to an analytically sound solution, but provides a reasonable way to estimate the method's feasibility and limitation. The result from an iterative utilization of the Wiener deconvolution is shown in the left hand graph of figure 6.9. For a start, the curve's maximum is definitely located at the center of the three-peaked pattern which was to be recognized from the data trace. Still, strong oscillations of the reconstructed trace do not let this technique appear as a promising solution to restore the Brillouin gain spectra from measurements of less accuracy and higher complexity.

In contrast to the simple division in the frequency domain and the Wiener deconvolution, which are both linear operations, a nonlinear iterative approach for image restoration was presented in the early 1970s and is known as the **Lucy-Richardson algorithm** [68], [69], [67]. As with the Wiener deconvolution, this algorithm is applied to the present problem by directly adopting its implementation in MATLAB. Details about its theoretical background can be found in the above references; the algorithm is based on iterative maximum-likelihood procedures to seek convergence of the expression

$$g''_{k+1}(\Delta f) = g''_k(\Delta f) \left(d(-\Delta f) * \frac{g'(\Delta f)}{d(\Delta f)\, g''_k(\Delta f)} \right) \tag{6.14}$$

with the presumption that the image can be modelled with Poisson statistics.

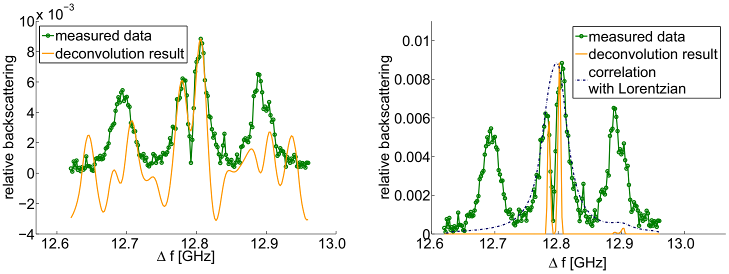

Figure 6.9: Restauration results obtained from deconvolution techniques used in digital image processing. *Left:* Wiener deconvolution. *Right:* Lucy-Richardson algorithm.

In the available implementation, input parameters to the algorithm are the degraded image, the point-spread function, the number of iterations to be performed and a threshold parameter of intensity for each data point below which damping occurs (in order to suppress noise generation in single data points). As a consequence of the introduction of such a threshold, the result is formed by narrow lines along the Δf axis, located at positions where the pattern of the PSF – the three Lorentzian spectra spaced by f_m – are recognized within the data. Such a result, obtained from the measurement of the 2200 m uniformly strained fiber, is shown in figure 6.9.

It can be seen that the three peaks of the recorded gain spectrum are recognized as one single instance of the pattern formed by the PSF (divided into two peaks due to the gap in the original measurement). When the result of the deconvolution is correlated with a Lorentzian-shaped smoothing curve, a single gain spectrum is obtained with its maximum at $\Delta f = f_B$. The result of the restoration of the complete transfer function (Lucy-Richardson algorithm applied to every data trace $g'(\Delta f)$ for each f_m) is shown in figure 6.10. Compared to the originally recorded measurement (see figure 6.6 one page 6.1.3), it can be seen that the phantom spectra are significantly suppressed; the three-peaked Lorentzian patterns have been recombined to the central spectra at $f_B = 12.79$ GHz.

Since the method for restoration of the Brillouin gain spectra was developed to permit the enhancement of spatial resolution with no constraint to strain resolution, evaluation of the method is performed with a measurement of the defined strain profile which has been presented in earlier chapters. In contrast to the measurements of homogeneously strained fibers, where the performance of the restoration can be evaluated by visually comparing plots of original and deconvoluted data, things get more complicated for real-life measurement traces. When a fiber with sections of different strain values is measured in the frequency domain, the trace $g'(\Delta f)$ for each f_m will consist of the superposition of various triplets of Lorentzian curves, with a central Brillouin spectrum and two phantom spectra, respectively. The task of any restoration algorithm is now to locate the origins of these patterns by means of

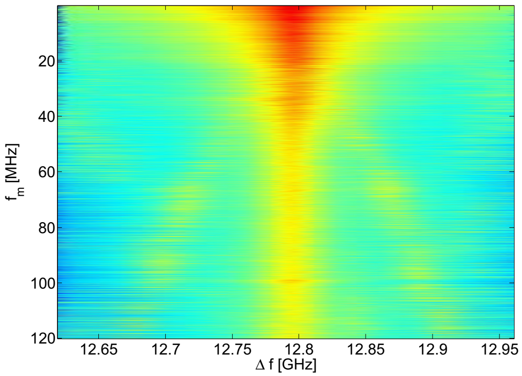

Figure 6.10: Magnitude of the transfer function of the 2200 m unstrained fiber after restoration using the Lucy-Richardson algorithm (to be compared with the original measurement from figure 6.6).

deconvolution and recombine them to one spectrum as it would have been measured with continuous-wave excitation.

In the following figures, the steps of signal processing performed to obtain the spatially resolved strain profile from frequency-domain data are performed, including the application of the Lucy-Richardson algorithm. Figure 6.11 shows the magnitude of the transfer function $|H(j\omega)|$ with the recorded gain spectra $g'(\Delta f, f_m)$. In the right hand graph, the deconvolution has been applied; visually, it can be observed in some sections of the graph that the characteristic pattern of phantom spectra, emerging at a fixed angle from the original spectra towards higher values of f_m, are eliminated by the restoration procedure. Still, this is no proof that the intricately superposed patterns are detected and reallocated correctly.

The same goes for the left hand plot in figure 6.12, which shows a cross-section of figure 6.11 at $f_m = 62.8$ MHz. More insight is to drawn from the right hand graph in figure 6.12, in which the inverse Fourier transform from the complex transfer function into the spatial pulse response for each trace along Δf has been performed.

Here, the artifacts that occur at high spatial resolutions can bee seen once more; they had been introduced at the beginning of this chapter and have been traced back to the presence of the phantom spectra. Now, with the phantom spectra supposedly being eliminated, the result of the restoration process is shown. The broadening of the Brillouin gain spectra has indeed been avoided (its spectral width is now governed by the Lorentzian function that has been used for smoothing by correlation, see the

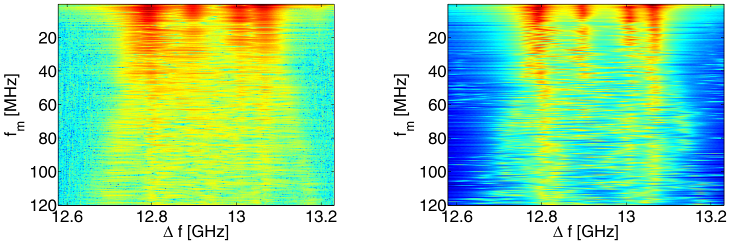

Figure 6.11: Restauration of the measurement of the defined strain profile. *Left:* Original measurement data. *Right:* Data after application of the Lucy-Richardson algorithm.

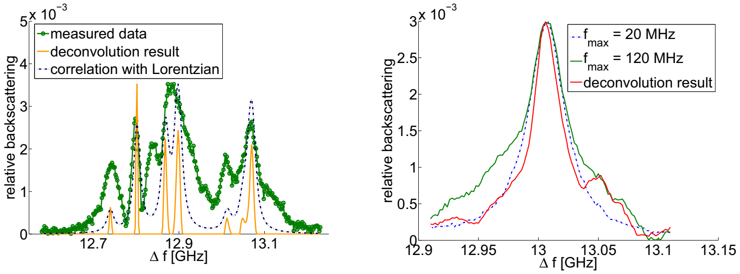

Figure 6.12: Cross-sections through the measurement data of the defined strain profile, restored using the Lucy-Richardson algorithm. *Left:* Data before transformation: $H(f_m = 62.8$ MHz, $\Delta f)$. *Right:* Data after transformation: $h(z = 157$ m, $\Delta f)$.

right hand plot in figure 6.12). The artifacts could partly be overcome – partly, as in this graph on the slope of higher Δf, remainders of the artifacts are still present.

If now the final analysis of the data is done – the transfer from the three-dimensional data of Brillouin gain spectra into the representation of strain versus fiber length – the performance of the restoration procedure at this stage of research can be evaluated.

The good news emerge from the right hand picture, which zooms into one of the fiber sections of high strain: The noisy measurement with $f_{max} = 120$ MHz is considerably smoothed by the restoration process, providing a significantly higher accuracy of the strain measurement. At the same time, spatial accuracy remains as good as it can be expected from the chosen modulation bandwidth: The edges at transitions of applied strain coincide exactly for the unrestored and restored measurement, while the edges of the $f_{max} = 20$ MHz measurement is forced to the inaccurate grid of low spatial resolution (unfortunately, the edges of strain transition, as they were estimated during application of the fiber to the coil, do not coincide with the measurements, since this estimation lacks accuracy due to mechanical reasons).

On the downside, the sections of unstrained fiber lose accuracy; it must be stated that the measured gain spectra lacked a clear Lorentzian shape at these values for Δf due to measurement failure. Still, this has to be seen as a drawback, since the original measurement was robust to these failures. Furthermore, the two spikes in the unrestored measurement at $z = 58$ m and $z = 65$ m are caused by very short sections (< 1 m) of applied strain; they are detected by the system, but are lost during restoration.

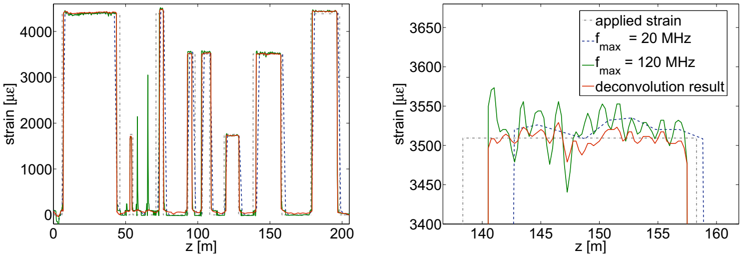

Figure 6.13: Comparison of the measurements on the defined strain profile.

As a conclusion, it must be stated that the proposed method does not eliminate the constraint of spatial resolution inherent to Brillouin sensing – at least not at this stage of research. The detection and reallocation of the characteristic patterns by means of algorithms taken from image processing within $g'(\Delta f)$ is not reliable and robust enough. However, the main purpose of this part of research was to trace back the occurring artifacts to their physical origin in Brillouin interaction of modulated light waves; basing on this solid ground, the proposed method should be further developed by refining the formulation for the PSF and enhance the deconvolution approach, for instance, by making it more sensitive to the characteristic traces of real and imaginary parts of $g'(\Delta f)$ instead of accounting for the magnitude only. By means of such further investigations, a signal restoration technique should be found that advances the promising results given here into a robust sensing system reliably measuring far into the centimeter range.

6.2.3 Approaches in the time domain

Ever since distributed Brillouin sensing has become an established sensing tool in practical applications, effort has been made to free the technique from the limitation of its spatial resolution to about 1 m. First promising perspectives have been reported with measurements of Brillouin gain spectra recorded using pulses of very few nanoseconds [66], [63]: Here, the broadening of the gain spectra that was expected to increase even further with pulses ever shorter and shorter was observed to decrease sharply when pulses shorter than 5 ns were employed. The presence of a so-called *pre-pump pulse* (a broad and weak pulse entering the fiber, to be followed by the actual, very short pump pulse) was used to reproduce such measurements.

Physical interpretations of these observations have been proposed and disputed controversially in recent years. The most recent interpretation was given by Thevenaz *et al.* [70], which is underlined by an experimental configuration which employs the new insight to perform high-resolution Brillouin measurements. Here, the decay time of the acoustic wave is shortened by cutting off the interaction between the pump pulse and the CW Stokes. This is achieved by performing a phase shift of π within the pump pulse, which flips around the phase of the excitation of the acoustic wave, rapidly attenuating the previously present interaction. This promising and theoretically sound approach has been presented as *Brillouin Echo Distributed Sensing*.

This chapter proposed a straight-forward approach extracted from the theoretical analysis of the artifacts occurring in frequency domain measurements; it takes advantage of the special nature of the BOFDA system and is distinguished from the time domain approaches by being performed in post-processing only, which means that no measurement hardware of higher complexity is necessary in order to overcome the uncertainty relation of spatial and strain resolution.

CHAPTER 7

Dike monitoring using the BOFDA system

When it comes to the development of a complete solution for a sensing problem in structural health monitoring, the measuring unit itself – the setup containing all electrical and optical hardware components as well as the signal processing software – can only be seen as one piece within a larger concept. Despite the numerous applications for distributed Brillouin sensing in the field of structural health monitoring, the stated goal of this work (and of the research project, forming its framework) was the development of a system for dike monitoring. Such a specialized, yet complex application requires simultaneous and iterative development of the different components that contribute to a final sensing solution. These components, interacting at each state of the development, are: first, a precise characterization of the geotechnical processes that are to be detected, allowing an exact definition of the system requirements; second, all issues regarding the integration of silica optical fibers into the soil (mainly, assuring a defined transfer from soil activity into longitudinal strain of the fiber while reliably protecting the fiber from destructive mechanical stress); third, the adjustment of the free parameters of the measurement unit to fit the requirements stated by the experts of dike construction and maintenance.

After summarizing the geotechnical requirements and introducing geotextiles as a central element of modern dike construction, this chapter presents the contribution of the author's research to the overall dike monitoring system: Each development stage, even the production of geotextiles with integrated optical fibers and the special sensing cable, had to be validated and adapted to fit the requirements of the measurement technology. Thus, a conceptional analysis of the interaction between the elements of the sensing system is a central part of this work and is presented in this chapter. The analysis allows the carefully directed validation of the stages of interaction with specially designed laboratory and field tests. In all tests described throughout this section – even if the setup on the out-door test sites was contributed by the project partners – the concept, realization and interpretation of the optical measurements, as well as the transfer of results and insights into specifications for the development of geotextiles and optical cables, was the author's responsibility and forms the contribution of this work to the successful development of a dike monitoring system with geotextiles as the carrier material for optical fiber sensors.

7.1 Requirements on a dike monitoring system

In the following, the specifications required from a system for dike monitoring from a geotechnical point of view are listed. The final system shall be designed to introduce a significant benefit into the maintenance of river dikes under normal long-term conditions as well as in the case of an extreme flood event. Therefore, the adjustment of all technical parameters that have been discussed throughout the preceding sections is to be done with the strict goal to fulfill these specifications.

1. For the determination of the required **spatial resolution**, there are two criteria to be considered: First, the resolution of the detection of soil displacement must be small compared to the expected geometrical dimensions of the geotechnical activities that have to be detected. According to the typical failure mechanisms of river dikes (see figure 1.2), a critical settlement, crack or breach will not be smaller than several meters. Second, the initiation of counter measures in case of an alarm has to be taken into account. Spatial information provided by the system will be used as a base for the dike operator to exactly localize the fault in the dike. If, for instance, a team entrusted with emergency management is supposed to reinforce the dike at the indicated spot using sandbags or alike, the indication of the failure more precise than several meters will not be necessary. It has been agreed that a spatial resolution of 5 m is an adequate goal for this monitoring task.

2. River embankments typically have lengths in the range from a few hundred meters to several kilometers (in contrast to coastal dikes, running along the shore for several hundred kilometers). This defines the required **measurement range** for the BOFDA system. A sensing length of 5 km has been considered to be a reasonable dimension by dike experts.

3. **Data acquisition time** has to be reasonably short to detect fast changes in the integrity of the dike. While seepage effects need days to result in measurable damage, the consequences of wave overtopping (erosion, slope breaks) might lead to a breach of the dike within less than one hour. Therefore, an acquisition time that allows quasi-real-time monitoring must not be longer than 30 minutes.

4. There is no analytical way to quantify the required **strain resolution** for the sensing system that defines a reliable detection of soil displacement. Because

of the complex relationship between soil activities and the longitudinal strain which is finally experienced by the optical fiber, the maximum resolution in $\mu\varepsilon$ is only relevant for the technical implementation of the measuring unit; regarding real-world applications, the system's performance in the detection of typical failure mechanisms has to be evaluated empirically. Several tests performing this type of evaluation are presented in this chapter.

5. Distributed sensing systems using SBS are sensitive to longitudinal strain as well as **temperature changes** in the optical fiber. The separation of these two quantities is a critical issue for many sensing applications. However, since the sensing task for the application in dike monitoring is the detection of soil displacement, the temperature is not to be measured. It has been shown in section 2.2.2, that the impact of temperature on the measured quantity (the Brillouin frequency shift f_B) is small compared to the impact of strain. The legitimacy of neglecting the error in the strain measurement induced by temperature changes requires a slowly varying temperature over time and length of the fiber. In the description of the experiments and field tests regarding the construction methods, it will be shown that this requirement is fulfilled by burying the optical fibers into the dike with a soil layer of at least 20 cm on top.

6. **Reliability and long-term stability** of the overall monitoring system are crucial issues in the final design. The measurement setup is in the state of a laboratory demonstrator at the time this thesis is written, so ruggedness and reliability of the device can not be evaluated yet. For the optical fibers, in contrast, these criteria have to be considered from the very beginning: Environmental issues such as chemical persistence of the coating materials and resistivity to animal activities must be taken into account when the integration methods of optical fibers into the soil are investigated.

7.2 Integration of fiber optic sensors into the soil

While all investigations on the Brillouin measurement unit is subject of the author's research, the method for integrating the optical fibers into the soil body of the dike is the point where all competences within the project – geotechnics, structural health monitoring, fiber optics and geotextiles – merge to achieve a single goal: The integration of fiber optic sensors into geotextiles as they are commonly used in dike construction. Experiences with such an integration had been reported previously [10]; however, these reports concern fiber bragg gratings, which are point-wise sensors that can only cover a sensing length of a few hundred meters. In contrast, distributed Brillouin and Raman sensing inside the soil body of structures for flood protection was performed only by burying the bare cable as a one-dimensional sensor [18], [71]. The potential of the entirely novel approach of bringing truly distributed sensors into soil structures together with geotextiles will be discussed in this section.

7.2.1 Geosynthetics

The use of various types of geosynthetics has become an essential instrument for the solution of a large number of geotechnical problems. In dike construction, they have become indispensable during the past 20 years [72]. The most relevant forms of geosynthetics are woven and non-woven textiles, geogrids, geomembranes and geocomposites. They perform several geotechnical functions: Filtration (allowing water to pass through while retaining particles of the filtered soil), drainage, separation of soil layers with different particle sizes, and reinforcement (prevention from slope erosion and increase of the overall stability of the earth structure).

Figure 7.1: Typical application of geosynthetics: geomembranes in a composite liner system for a municipal waste landfill

Preliminary investigations at the Saxon Textile Research Institute (STFI) on geotextiles have shown that non-woven fleece mats, as they are used as drainage and filter materials in geotechnical engineering, are well suitable to apply coated optical fibers by means of a warp-knitting technique on their surface. The idea of manufacturing geotextiles with integrated optical fibers for sensing purposes yields two main advantages:

1. The geotextile mats act as a **carrier for the optical fibers**. Silica fibers, even if coated, are fragile and run the risk of losing their optical properties under the rough conditions of a construction site. Significant effort is needed to integrate the embedding process of the fibers into the construction procedure. In contrast, the processing of geotextiles during dike construction is an established procedure; all infrastructure for delivery and integration of the textile mats in large scale are readily available at the construction sites. It will be shown later, that little extra effort is needed to process the geotextiles with integrated optical fibers. In this concept, a central requirement on the method for integrating the optical fibers into the textiles is the preservation of the original functions of the textiles as drainage or filter materials.

2. The optical fiber with its sensitivity to longitudinal strain has to be seen as a one-dimensional deformation sensor. Its ability to **detect soil activities of arbitrary geometrical orientation** is significantly enhanced by the integration into geotextiles: Any movement of the soil will induce stress in the two-dimensional geotextile, which is mechanically connected to the earth by frictional forces. Any deformation of the textile mat will be partially transferred into longitudinal strain of the optical fiber.

As a consequence of the second characteristic of the geotextile – the conversion of the one-dimensional fiber into a two-dimensional sensing element – a spot in the dike profile for optimum placement of the sensors could be found. Applying the distributed sensors to the land-side berm (the narrow horizontal bench on the dike foot) allows to detect soil movements resulting from a large number of common failure mechanisms for river dikes. This position for optimum reliability of the displacement detection has been illustrated in figure 1.2 on page 3. The arrangement of the geotextiles equipped with fiber optic sensors is illustrated in figure 7.2.

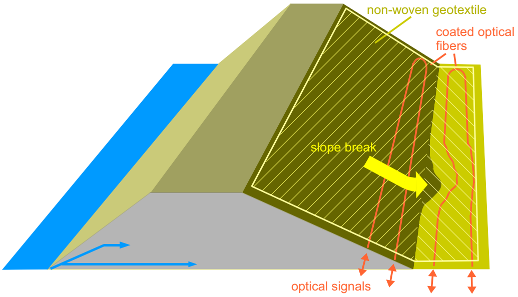

Figure 7.2: Schematic illustration of the arrangement of the geotextiles equipped with fiber optic sensors at the land-side foot of the dike.

The most critical issue during the development of a technique for integrating the optical fibers into the geotextiles was the generation of a fixed connection between the coating of the fiber and the fabric without losing the optical properties of the fibers. In first studies, silica optical fibers with acrylate primary coating, but no secondary coating or strain relief were integrated at STFI. Using an OTDR instrument for measuring the optical attenuation, it could be observed that the optical fibers had been severely damaged during the warp-knitting process. After few meters, attenuation of the optical signal increased within a few stitches of the knitting structure. At closer inspection, bendings of small diameter could be seen.

These experiences laid out a road-map for the further research on the integration technique: On the one hand, the warp-knitting process had to be optimized in order to provide a safe integration of the fiber into the textile without any damage done to the fiber; bendings with diameters smaller than 10 mm had to be avoided by all means [31]. On the other hand, an adequate coating material had to be found in order to provide protection of the optical properties of the fibers during processing.

For the first task, the free parameters for optimization were the stitching length as well as several other tunable variables of the warp-knitting machine [73] which shall not be subject of this thesis. As will be discussed in the next section, the use of coating materials of a diameter of approximately 3 mm had soon been agreed on. The final technique of integrating such cables is shown in figure 7.3.

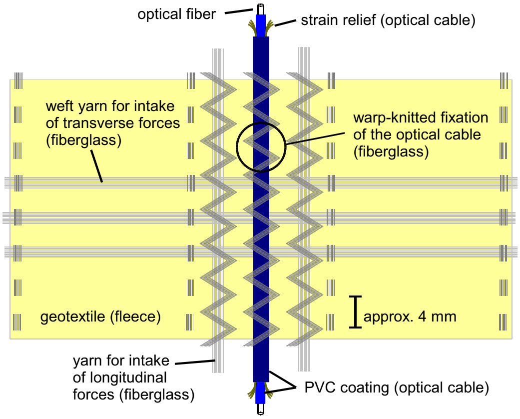

Figure 7.3: Result of the development of a method for integrating a fiber optic cable into a non-woven geotextile using a warp knitting technique. Research and fabrication have been carried out at STFI, Chemnitz.

Successive monitoring of the optical attenuation of the fiber by OTDR measurements parallel to the optimization procedure of the textile process led the way to the final structure and displayed the requirements on the coating material of the optical fibers. The next section describes the most relevant cabling variants that have been employed throughout the investigations.

7.2.2 The sensing cable

The design of a fiber optic cable for telecommunications follows a number of straightforward parameters: Optimum protection of the fiber must be provided by means of rugged coating materials, strain relief and gel buffers; furthermore, the cost per meter for the material and its installation as well as the handling and assembly of connections are of leading significance.

In contrast, the design of a cable suitable for distributed strain measurement must obey more contradictory parameters. If the coating and all strain relief and buffering prevents the fiber from any stress it might experience due to outside mechanical activities, all sensing properties will be eliminated. On the other hand, if all stress and bending applied to the coating were directly transferred into the fiber, irreversible damage of the optical fibers would occur – if not during integration into the textiles, then certainly during the construction process on the building site of the dike. Extensive tests of the behavior of various cable configurations in both phases have been performed and will be presented in section 7.3. Already after early tests, experience showed that a trade-off is needed between protection of the fiber from the rough forces during the integration process, and the preservation of the sensibility of the fiber to displacement of the surrounding soil.

After the first experiences made with uncoated fibers, standard indoor cables were integrated into the textiles. From a number of configurations, differing in thickness and number of layers of the polymer coating, tightness of the buffering, and realization of strain relief, feasible compromises could be separated from hardly suitable solutions of extreme parameters. A loose fiber running inside a gel buffer in a polymer tube, manufactured by Fiberware, could be reliably integrated into geotextiles and into the soil without suffering from any extra attenuation, but had no potential for acting as a strain sensor, since slipping inside the tube prevented the fiber from experiencing any lateral strain. The contrast to this loose fiber was manufactured by Leoni: A fiber with two tightly applied layers of polymer coating, lacking any strain relief, gel buffer and even a reserve in length of the fiber compared to the coating material. In various attempts, no successful integration into the textile could be achieved: Any small transverse stress or bending would add a significant value of optical attenuation; even storage of a rolled-up textile mat led to damage of the fiber due to pressure by the textile's own weight.

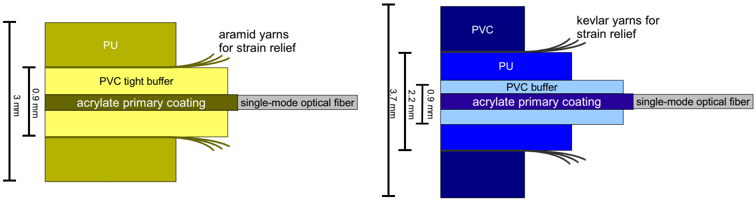

Figure 7.4: *Left*: the standard indoor cable SC LSZH by Nexans. *Right*: the specially devoloped „Dike cable“ by Fiberware.

A cable variant with an adequate protection as well as promising properties regarding the transfer of mechanical stress into the optical fiber was found with the indoor patch cable SC LSZH from Nexans. The design of this cable is shown in figure 7.4 on the left side. A tight buffer of 900 μm is assembled around the primary acrylate coating of the optical fiber. Separated by aramid yarns for strain relief, the 3 mm outer sheath is applied. As will be shown in the following sections, this cable came reasonably close to the desired trade-off between a protective and a sensitive coating concept. Still, the loose buffering with aramid yarns drastically decreases friction between the two layers of polymer coating. This leads to noticeable slipping of the fiber in case of stress applied to the outside sheath and results in a blur in the longitudinal measurement signal, i.e. a decrease in spatial as well as strain resolution.

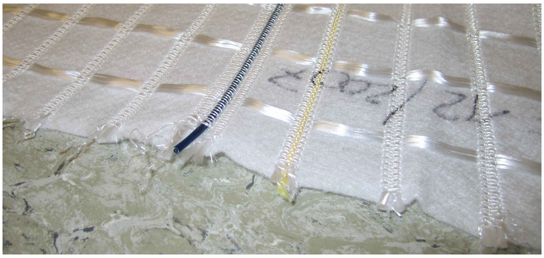

Figure 7.5: Photograph of a non-woven fleece mat, equipped with the FIBERWARE special sensing cable (*blue*) and the NEXANS standard indoor cable (*yellow*)

The first cable solution especially developed for distributed measurement of soil displacement is shown in figure 7.4 on the right side. This development has been commissioned to FIBERWARE GMBH, Mittweida/Sachsen, with the gathered experience from laboratory and field tests of all available standard cables [74]. The first two polymer layers on the primary coating of the optical fiber are applied tightly upon each other. The main task of these two layers is the compensation of transversal forces without diminishing the impact of longitudinal stress on the optical fiber. Kevlar yarns are added for strain relief. The outer coating is again tightly applied to the inner ones; all in all, the transfer from outside forces to the fiber occurs much more directly than in the standard NEXANS SC LSZH cable.

7.3 Evaluation of the system components

The problem of transferring the physical quantity that is to be measured (geotechnical activities leading to soil displacement) into the quantity that is actually measured by the Brillouin system (the Brillouin frequency shift, induced by longitudinal strain of the optical fiber) has already been introduced in section 1.2. Figure 7.6 illustrates this long chain of transfer from one physical quantity to the next.

With geotechnical activities inside the dike, possibly being an early stage of a fatal mechanism leading to dike failure, soil displacement of any dimension or orientation may occur.

The first stage of force transfer is the deformation of the geotextile by soil displacement. As laid out in section 7.2.1, a geotextile positioned at the land side berm will experience mechanical stress: its tight mechanical connection to the surrounding soil by frictional forces and the weight of the soil layer on top of it provide a direct transfer from the three-dimensional movement of the particles into a two-dimensional deformation of the textile mat. For simple soil activities, such as a settlement cavity of a defined shape, this transfer can be numerically modeled, predicting the geometrical deformation of the textile. Still, for complex failure mechanisms, such modeling is hardly feasible. Within this work, empirical studies of the mechanical connectivity have been considered far more valuable.

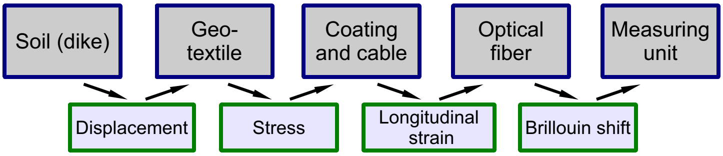

Figure 7.6: Transfer chain of physical quantities from soil deformation in the dike to the measured signal containing the Brillouin frequency shift f_B

The second stage describes the transfer from the two-dimensional deformation of the textile structure into the one-dimensional sensor which is the optical cable. Even from this geometrical consideration, a large factor of uncertainty for a quantitative analysis of the soil activities can be seen. The orientation of the cables inside the textile and the distance of the fiber to the center of the activity will determine the stress that the cable will experience (illustrated in figure 7.2, where two parallel sensors are unequally stressed). A second element of uncertainty is the fixation of the outer coating material of the cable on the textile, drawn in figure 7.3. Here, experiments have shown that due to the tight application using the warp-knitting technique (in which even slight constriction of the cable by the fiberglass yarns occurs) and the frictional forces of the soil particles, no significant slipping of the cable inside the textile has to be feared.

The third stage concerns all parameters of the sensing cable listed in section 7.2.2. Experiments using a tightly fixed coating on the optical fiber had shown that such a direct transfer of any stress applied to the cable into strain of the fiber is not desirable. With the two favored cable solutions that have been described, a certain amount of slipping of the fiber inside the coating can be expected and is intended. Also the use of a length reserve for the fiber buffers the forces of direct stress transfer. While the slipping of the fiber adds an irreparable uncertainty in spatial resolution to the measurement, the length reserve will lead to elimination of the first small amount of applied strain in the measurement. After passing the point of elongation of the cable at which the fiber tightens, the fiber will be able to sense all additionally applied strain. Taking advantage of this effect, the length reserve can be used for adjustment of the operating point of the sensing system by producing the cable with more or less length reserve.

The fourth stage is determined by the impact of longitudinal strain applied to the silica fiber on the Brillouin shift f_B. The linear dependence of the quantities has been discussed in section 2.2.2. The main critical issue at his stage is the – in our application undesired – influence of the temperature on f_B. The considerations showing that this factor may be neglected in the application of dike monitoring have been laid out in section 7.1.

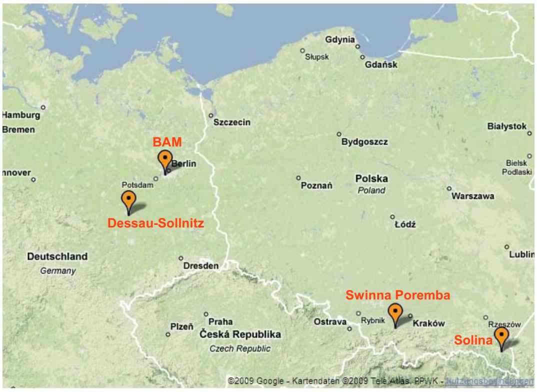

Figure 7.7: Locations of the construction sites where the tests that will be described throughout the following sections were performed (*Source: Google Maps*).

All tests of the distributed sensing system that will be described throughout the following sections refer to one or more of the stages of force transfer described above. However, tests have not been performed in an order that would strictly correspond to the transfer chain of figure 7.6. Due to the cooperation of several partners in each of the tests and the complex meshing of the optimization parameters for each component of the overall system, the experimental evaluation has rather been approached from opposite ends of the chain. In order to focus on the stepwise improvement of the overall system, the next sections will present the experiments in the chronological order in which they have been carried out, rather than in a systematical order corresponding to the stages of force transfer.

7.3.1 The optical cables and geotextiles in the field

The Mulde dike in Dessau-Sollnitz

The first attempt to integrate sensor-equipped geotextiles into the soil was performed to evaluate the feasibility of the combination of standard cable solutions off the shelf and non-woven fleece mats for the rough conditions on real construction sites.

Nine different fiber optic cables – the most relevant of which have been described in section 7.2.2 – were applied on a fleece mat of 4 x 50 m at STFI, using a Karl Mayer Malimo raschel machine. During this process, the optical properties of all fibers were monitored by means of OTDR measurements. On a construction site of a dike in the catchment area of the river Mulde in the community of Dessau-Sollnitz, Sachsen-Anhalt, the mat was rolled out along the land-side berm of the dike. A layer of soil was then poured out over the textile mat and compacted. In both these work-steps, heavy machinery was employed.

Figure 7.8: Photographs from the construction site in Dessau-Sollnitz during the first attempt to integrate sensor-equipped geosynthetics into the soil body of a river dike.

OTDR measurements of all optical fibers have been performed after unloading, after unrolling and finally after the application of the soil layer. Measurement traces corresponding to two different cable solutions are shown in figure 7.9.

On the left, the tightly coated cable with no length reserve, manufactured by Leoni, is shown. It can be seen, that significant optical losses appear due to rolling up the mat after the integration of the fibers, since all bending of the cable is directly transferred into stress of the fiber via the tight coating. These losses decrease after rolling out the textile mat on the site. The fiber broke during the application or compaction of the soil, as can be seen in the third trace at $z = 5$ m.

On the right, measurements of the standard indoor cable SC LSZH by Nexans are shown. No losses can be detected by the OTDR measurement over the whole length of 50 m after the textile integration process; at 55 m, there is a fusion splice, which was squeezed together by rolling up the mat, but returns to its original function after rolling it out on the dike. Anyway, like all other fiber samples in the textile mat, this fiber broke ($z = 5$ m) during the application or compaction of the soil.

The most probable explanation for the loss of all fibers due to breakage at $z = 5$ m is the mechanical overload by the dump truck, which was observed to fold the textile in front of its wheels while bringing the soil to the rolled-out mat. The fold finally collapsed, and the truck weighed on the fold with its entire weight. Most probably, none of the fibers survived this crucial moment.

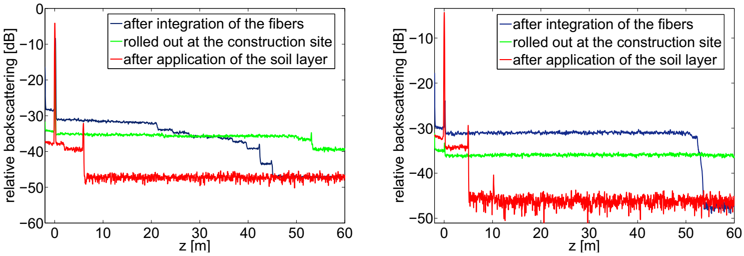

Figure 7.9: OTDR measurements from the installation tests of geotextiles equipped with optical fibers in Dessau-Sollnitz. *Left*: the cable with tightly applied coatings by LEONI. *Right*: the cable SC LSZH by NEXANS.

As a conclusion from this first test it can be stated, that the general feasibility of certain optical cables – especially the NEXANS indoor cable – for integration into textiles was shown. A very valuable result was the insight into real-world circumstances on a construction site – and the understanding that the use of heavy machinery puts high demands on the mechanical ruggedness of the optical cables.

Dam construction sites in Solina and Swinna Poremba, Poland

The next stage of field tests for the integration of geotextiles with integrated optical fibers was performed with a matured technology for textile integration of the optical cables. Furthermore – as a consequence from the experiences made in Sollnitz – the application of the first soil layer had to be performed manually. This demand proved to be accomplishable on well-organized construction sites. The tests were carried out at two construction sites in Poland: The first of the two construction sites was part of a gravity dam located in Solina in the south-east of Poland, a few kilometers from the border with Slovakia and the Ukraine, while the second was the construction site of a large earth dam in Swinna Poremba, some 50 km south west of Krakow [1].

At the site in Solina, a fleece mat of 17.5 x 4 m, equipped with samples of the standard NEXANS cable, the tightly buffered LEONI cable and the loosely swimming version from FIBERWARE was embedded into the soil. Of each variant, two parallel

---

[1] Both construction sites were provided to the project by GLÖTZL GMBH.

samples had been integrated into the mat and had been connected at one end by means of a fusion splice, thereby providing sensing lengths of 35 m, not counting the pigtail cables at the outer ends. On site, the textile mats were rolled out and covered with soil manually, using spades. The optical performance of the fibers was measured with the OTDR unit after rolling out the mat and after applying the soil layer. These measurements could be compared to measurements that had been taken after fabrication, serving as a reference.

Figure 7.10: The geotextiles with applied optical cables in Solina (*left*) and Swinna Poremba (*right*).

Results from the OTDR measurements on a NEXANS SC LSZH cable embedded in Solina are shown in figure 7.11. The reference curve from the rolled-up textile mat stored in the laboratory, ready for transportation, shows practically no losses except for the fusion splices at 5 m (end of the first pigtail), 22 m (connection point of the two cable samples) and 42 m (start of the second pigtail). No damage was experienced by the optical fiber during the embedding procedure on the construction site: The curve that was recorded after the soil layer had been applied can be considered as almost identical to the reference measurement.

For the other cable variants, embedding without damaging the fibers could not be achieved. It has been agreed after these measurements, that the NEXANS SC LSZH cable represents the optimum solution among the fiber optic cables available off the shelf.

Fourteen months after the embedding of the textile mats in Solina, the optical characteristics of the fibers were measured again. The result for the NEXANS cable is shown in figure 7.11. The peaks at the locations of the fusion splices, being much larger than the corresponding peaks in the traces from the installation measurements, are due to the usage of a different OTDR unit having a lower spatial resolution and considerably larger event dead zones. In spite of these constraints of the measurement accuracy, it can be seen that optical losses have increased at the locations of the fusion splices, but attenuation in the fiber sections along the textile mats has largely remained constant over the 14-month period (the increase of losses lies within 1 dB along each 17 m section), including one winter (continental climate, 482 m above sea level).

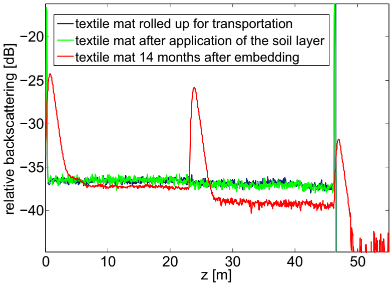

Figure 7.11: OTDR traces from the installation tests in Solina, Poland. The fibers had been integrated into fleece mats at STFI and were manually embedded into the soil on the foot of a gravity dam.

With the experiments and measurements carried out in Solina, the feasibility of the integration technique for standard optical indoor cables into geotextiles as well as the embedding method of the mats into the soil was shown.

The second test in Swinna Poremba was performed using textile mats that were produced at a much less mature stage of the integration process at STFI. A new technique of using weft yarns for intake of transverse forces was employed, leading to heavy microbendings of the optical fibers. OTDR measurements before the embedding procedure had already shown significant optical losses; these losses even worsened during the application of the soil layer (which was manually performed in a professional manner). The measurements provided no exploitable results and are therefore not given here.

The measurement campaign in Poland can be seen as a success due to the very good results achieved in Solina. The difficulties experienced in Swinna Poremba meanwhile showed the need for further optimization of the textile integration process. For later textile samples, the technique including transversal weft yarns was then matured and proved feasible, as will be shown in the following sections.

7.3.2 Detection of soil displacement with the BOFDA system

Detection of soil movement at the laboratory dike of the university of Hannover

The field tests to evaluate and optimize the technique of integration of optical fibers into geotextiles led to a deeper understanding of the sensitivity and handling of the fibers, the textiles and real life on the construction sites. The next stage of evaluation incorporated the entire laboratory setup for the Brillouin optical frequency domain analysis. The task was to prove the system's feasibility to detect and locate soil displacement by means of distributed strain measurement. At this stage of development (as it is described in chapter 4 (figure 4.1)), the system could repeatedly perform reliable measurements of Brillouin gain spectra along several hundreds of meters of an optical fiber. It had been calibrated to longitudinal strain, as it has been described in section 4.4. The setup at this stage consisted of the two-laser configuration described in section 4.1.1 and the analog vector network analyzer.

On the test area of Franzius Institute at the University of Hannover, a 15 m segment of river dike – true to scale in its dimensions – was available for measurements. A cross-section of the basic setup for the tests is shown in figure 7.12. As it had been proposed by the geotechnical experts from the University of Hannover (see figure 1.2), the fleece mats were brought into the soil near the surface of the land side berm, covered by a sand layer of approximately 20 cm. The water in the basin on the opposite side of the dike was headed up in order to induce slight seeping through the dike body, providing more mobility of the sand for emulation of the geotechnical activities.

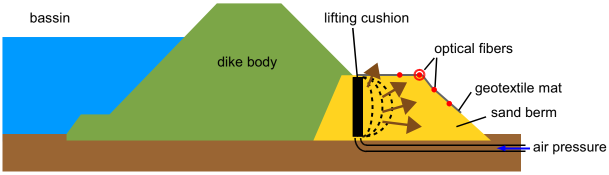

Figure 7.12: Cross-section through the laboratory dike at Franzius Institute, University of Hannover. The basic setup for the emulation of a slope break on the land side berm, using an upright lifting cushion, can be seen. The highlighted fiber at the edge of the berm was selected for the measurements.

Two inflatable cushions of 70 by 70 cm were buried into the sand body of the berm. One of them was filled with water and placed horizontally about 1.5 m beneath the surface. The purpose of this cushion was the emulation of a cavity inside the soil – as it might be caused by washout or piping – that would lead to settlement. Unfortunately, deflating of the cushion by letting out the water did not have the desired result: The humid sand did not collapse and no movement could be observed, neither visually nor by the sensing system.[2] The second cushion was deflated and buried in an upright position (see figure 7.12). With its inflating range of approximately 40 cm, it was

---

[2] Looking at the aim of the test campaign – the emulation of different types of geotechnical mechanisms inside the dike – the horizontal cushion has to be seen as a disappointment. However, from a more distant point of view, it serves very well as an illustration of the complexity of the dynamic behavior of sand and soil, where even geotechnical experts fail to predict the movement of the sand, whether by means of experience or analytical computation. This insight underlines

able to significantly deform the sand body of the berm within a radius of at least 1 m, thereby becoming detectable by the sensing system's spatial resolution of 2.5 m.

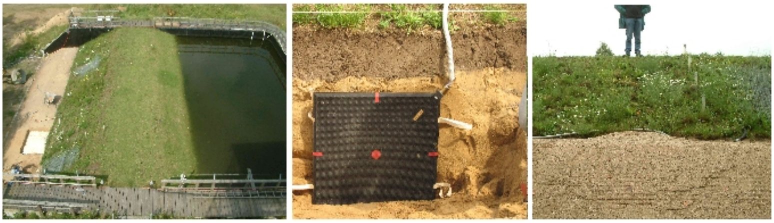

Figure 7.13: The photographs show, from left to right, the laboratory dike at the University of Hannover, the lifting bag before embedding into the soil, and the soil displacement induced by the lifting bag, visible on the surface of the dike foot.

The fiber section which was in best condition in terms of optical attenuation was selected for the measurements: The NEXANS standard indoor cable at the edge of the berm, indicated by an extra ring in figure 7.12. A reference measurement was taken, then the inflation of the cushion was started. Measurements were taken at values of air pressure of 1.0 bar, 1.4 bar, 1.8 bar, 2.2 bar, 3.0 bar, 4.2 bar and 6 bar. Lifting up and cracking of the surface of the sand berm could be observed visually from 1.8 bar; movement of the slope was observed from 3 bar of air pressure.

In figure 7.14, the recorded Brillouin gain spectra from the measurements in the region of the upright cushion are shown (the spot is located after 205 m of connection cable and 5 m from the beginning of the sensing section inside the dike). First movement of a section of Brillouin gain spectra towards higher values of the Brillouin frequency shift f_B was observed at 4.2 bar of air pressure.

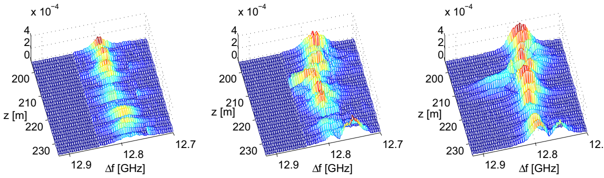

Figure 7.14: Measurement of the Brillouin gain spectra at the stressed section of the sensor-based geotextile mat in the laboratory dike at University of Hannover. At 210 m from the beginning of the optical fiber, a lifting cushion was inflated by air pressure. The figures show measurements taken at 3 bar, 4.2 bar and 6 bar of air pressure.

---

the need for distributed sensing systems in order to capture soil activities empirically rather than analytically.

Compared to the results from laboratory measurements that have been presented in section 4.4, these gain spectra appear blurry and fragmentary, lacking precision to conclude the absolute strain values from the maxima of the gain spectra. In fact, after Lorentzian fitting of the recorded spectra, the section of geotechnical activity could be qualitatively located, as it can be expected from the raw data shown in figure 7.14, but due to the noisy environment of the critical section within the trace, a quantitative analysis could not be performed.

This lack in signal quality can be traced back to two main issues: The problem of fluctuating Brillouin gain due to alternating states of polarization, as it is described in section 4.3, had not been solved at this stage of development, which accounts for the large gaps along the spatial axis in the supposedly continuous gain spectra. Furthermore, the technique of integrating the optical cables into the fleece together with transversal weft yarns had not been optimized yet; the fibers had suffered from the additional transversal stress that occurred during the integration procedure at STFI, which led to significant optical attenuation along the fibers (approximately 4 dB loss on a 20 m section) and limited the dynamic range of the measuring unit.

In spite of these drawbacks, the reliable detection (in the sense of an alarm system) of soil displacement in the test dike makes the overall test campaign at Franzius Institute a success. While the Brillouin frequency domain analysis was applied for geotechnical monitoring for the first time, the results clearly show both the potential of the system and the difficulties that have to be overcome to convert the setup into a mature solution.

Emulation of soil settlement using a polystyrene model

The test campaign in Hannover had been designed to cover a wide area of the chain of force transfer that has been illustrated in figure 7.6: A rather undefined complex of geotechnical activities, manually induced by inflating the cushion, was to be detected and located by the system. While this experiment was very revealing regarding the system's capability of qualitative monitoring, all elements of the transfer chain that are responsible for inaccuracy of spatial and quantitative information remained hidden. These elements are mainly the fiber slipping inside the cable and the uncertainty of the mechanical deformation of the geotextile, linking the displacement of the surrounding soil to the stress applied to the cable.

For the laboratory test that was designed to quantify these remaining stages of interaction, several advancements in different parts of the overall concept (compared to the state of the system that was employed in Hannover) were available: First, a solution for the problem of gain fluctuations due to alternating states of polarization had been found (see section 4.3). Second, two different types of optical cables were now available: Apart from the approved standard solution from Nexans, the special development from Fiberware, as it is described in section 7.2.2, was ready for testing in the lab. Finally, the problem of increased optical losses in the fibers due to the integration of transversal weft yarns into the geotextile had been overcome at STFI. Together with several more marginal issues that had been solved concerning the measurement hardware and signal processing, the system was now ready for an analytically designed experiment showing the connection between a defined deformation of the geotextile and the final measurement signal, i.e. the distributed strain profile of the fiber.

For the emulation of a soil activity (the cause of deformation of the textile) as realistic as possible, a cavity as it might appear due to settlement was chosen. A cross-section of such a cavity with a diameter of 2 m was modeled into a block of polystyrene, providing the cavity-shaped substrate and its counterpart. Between these two profiled polystyrene blocks, the sensor-equipped textile mat could be placed and forced into the profile, thereby being deformed and transferring the mechanical stress into the fiber cables. Figure 7.15 shows the setup with the wooden frame in which the polystyrene blocks and the textile are fixed.

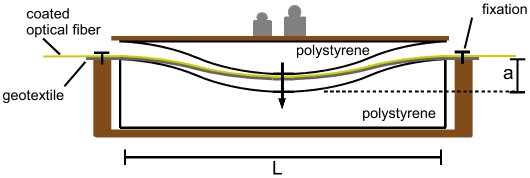

Figure 7.15: Setup for the settlement emulation using a polystyrene model of a cavity. The textile mat equipped with two different cables is fixed on the wooden frame.

With the cosine function, forming the shape of the cavity, the elongation of the textile mat when forced into the cavity can be calculated, thereby giving the average strain along the geotextile. If no slipping of the cable and the fiber should occur – which is not to be expected – this strain value would be detected by the Brillouin sensing system. With the cavity's diameter L and depth a (twice the amplitude of the cosine) of the cavity, the average strain ε is determined by the path integral of the cosine:

$$\varepsilon = \frac{1}{L}\int_0^L \sqrt{1+\left(\frac{\pi a}{L}\right)^2 \cdot \sin^2\left(\frac{2\pi}{L}x\right)}dx - 1 \tag{7.1}$$

With $L = 2$ m, two different profiles were assembled: The first one resulting in an average strain of 1 % (10000 $\mu\varepsilon$), formed by a cavity with $a = 12.8$ cm; the second one resulting in 1.6 % strain (16000 $\mu\varepsilon$) with $a = 16.2$ cm.

Samples of the two optical cables under test had been integrated into a fleece textile at STFI with parallel and transversal weft yarns (see figure 7.3). Within a textile sample of 2.50 m × 0.22 m, the two cables (NEXANS standard cable and FIBERWARE special cable) were running along parallel lines, spaced by 10 cm. They were interconnected with a fiber of 10 m length; together with 165 m of advancing fiber and another 10 m at the end of the setup, they formed one single sensing section of 190 m.

In order to fix the textile sample on the wooden frame, the fleece was reinforced with epoxy on both ends and screwed tightly on the frame; with this configuration, slipping of the cable inside the textile binding was inhibited.

Three measurements were taken using the BOFDA lab setup: The first one served as a reference measurement and was taken after fixing the mat on the frame. A second measurement was performed after the mat was forced into the first cavity profile. Then the textile mat was relaxed, the polystyrene blocks were substituted by the second cavity profile, and a third measurement was taken of the textile mat, now forced into the second profile.

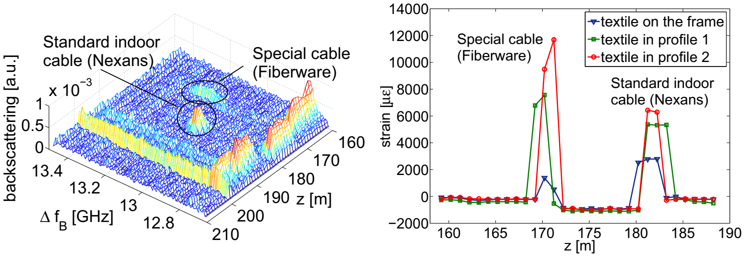

Figure 7.16: Measurement results from the emulation of soil settlement in the polystyrene profile. *Left*: Brillouin gain spectra of the optical fibers after forcing the mat into profile 1. *Right*: Strain of the optical fibers at different stages of the experiment.

Figure 7.16 shows the results from the measurements of the polystyrene model, and with a careful look, the relevance of the cable development by FIBERWARE becomes clear. In the left-hand image, showing the Brillouin gain spectra of the textile forced into the first profile, both strained fiber sections are clearly visible as regions moved towards higher values of the Brillouin frequency shift f_B. Three aspects of dissimilarity of these two sections shall be pointed out: First, the spectra of the FIBERWARE cable are shifted significantly further to higher values of f_B, indicating that the fiber inside the special cable experienced a higher amount of strain than the fiber inside the standard NEXANS cable. Second, the FIBERWARE spectra are lower and, third, noticeably broader than the spectra of the NEXANS cable. A fourth important distinction becomes visible after the fitting procedure, which leads to the two-dimensional plot of strain versus fiber length in the right-hand image of figure 7.16: The length of the strained fiber section is significantly shorter for the FIBERWARE cable than for the NEXANS cable.

Table 7.1 shows the values of measured longitudinal strain of the two fiber sections, as well as the relation of the measured strain to the elongation of the textile. The discrepancy between these values can be traced back unambiguously to the effect of slipping of the silica fiber inside the coating material of the two cable variants. As it had been expected, this effect is much stronger in the NEXANS standard indoor cable than in the cable from Fiberware. Aside from the lower strain value experienced by the fiber inside the Nexans cable, also the other aspects of dissimilarity that have been pointed out can be explained with this interpretation: The effect of slipping leads to a stronger blur in spatial resolution in the Nexans cable, which accounts for the broader peak in the right-hand image in figure 7.16.

	Δl [‰]	ε_{Nex} [$\mu\varepsilon$]	$\varepsilon_{Nex}/\Delta l$	ε_{FW} [$\mu\varepsilon$]	$\varepsilon_{FW}/\Delta l$
Fixation	0	$2.78 \cdot 10^3$		$1.39 \cdot 10^3$	
Profile 1	10.0	$5.34 \cdot 10^3$	0.26	$7.57 \cdot 10^3$	0.62
Profile 2	16.0	$6.43 \cdot 10^3$	0.23	$11.69 \cdot 10^3$	0.64

Table 7.1: Measured strain values for the standard indoor cable from Nexans (ε_{Nex}) and the special development from Fiberware (ε_{FW}), set in relation to the elongation experienced by the textile mat Δl.

Finally, the shape of the gain spectra in the strained sections – the spectra of the Fiberware special cable being broader and flatter – can also be explained by the slipping of the fiber: While the loose buffering of the fiber inside the Nexans cable allows the fiber to settle at an average strain value over the whole section experiencing mechanical stress (limited by the two points where friction becomes high enough to keep the fiber from slipping), the force transfer of the mechanical stress from the Fiberware cable to its fiber is much more direct. The inhomogeneous longitudinal strain, caused by the cosine profile, is transferred to the fiber, resulting in a continuously changing Brillouin shift and therefore broad and flat gain spectra.

In order to evaluate the capabilities of the sensing system to detect critical soil activities, this test has proven to be very valuable. Despite the obvious restrictions – laboratory conditions instead of a field test, polystyrene instead of moving soil – the experiment gave insight into the interaction of the textile, the cable, the fiber and the BOFDA setup. In the end, it showed that without an exact definition of the application, a decision concerning the best cable solution is not appropriate. Better protection of the fiber comes at the cost of a blur in spatial resolution – conversely, taking the two evaluated cable solutions as cornerstones, the sensitivity has to be traded off against the fiber protection for each application, using the buffering of the fiber as the tuning parameter.

Strain measurements at the net test bench at STFI

The Saxon textile research institute (STFI) in Chemnitz owns a test bench for the evaluation of net structures for logistics, safety and security applications (luggage nets, safety nets in sport stadiums etc.). The setup of the test bench consists of a rectangular steel frame of adjustable dimensions (for our experiments, it was fixed to a square of approximately four by four meters) around a pit, from which a hydraulic indenter with a mushroom shaped head can be risen. The indenter will apply mechanical stress to a textile (net, geogrid, fleece mat etc.) that is fixed on the frame, allowing to determine the maximal mechanical load that the textile under test is able to withstand. A basic drawing of the test bench is given in the left-hand image in figure 7.17.

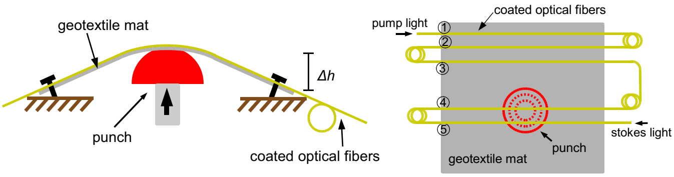

Figure 7.17: *Left*: The net test bench with the mushroom-shaped hydraulic indenter at STFI. *Right*: Configuration of the sensing cables in the fleece mat under test. In the sensing cable, sections (1), (3) and (4) are formed by the Fiberware special sensing cable; sections (2) and (5) are standard Nexans indoor cables.

Textile mats with integrated fiber optic cables for strain measurement (the Nexans standard cable and the Fiberware special cable) were evaluated on the net test bench, using a configuration similar to the polystyrene model test: Various cables parallely integrated into the geotextile (fleece) mat were fixed at the edges with epoxy. In total, five sections of sensing fibers where included in the mat under test, each with a length of 2.5 m, and all interconnected so that they form one segment (see figure 7.17 and its caption for the exact configuration). With the mat fixed on the bench, the indenter was raised from its pit, stretching the textile in its two geometrical dimensions. Distributed strain measurements using the BOFDA setup were performed at several steps of elevation of the indenter. Figure 7.19 shows the results of the distributed measurements after the curve-fitting procedure of the Brillouin gain spectra. For the reference measurement taken after fixing the textile mat on the frame as well as for three steps of elevation of the indenter, the five sections of strained fiber are clearly visible. A flaw in the experiment must be pointed out: In the trace corresponding to 300 mm of elevation, the gain spectra of the strongly strained section (4) ($z = 25$ m) are outside the sweep range of the laser frequency detuning Δf due to insufficient adaptation of the measurement parameters to the expected strain values.

Figure 7.18: Photograph of the fleece mat stressed by the mushroom-shaped indenter at STFI.

These experiments gave a valuable confirmation of the results obtained in the tests using the polystyrene model, but hardly delivered new insights into the sensor's performance. From a textile research point of view, the insight into the relation between applied force and elongation of the reinforced fleece mat was rewarding.

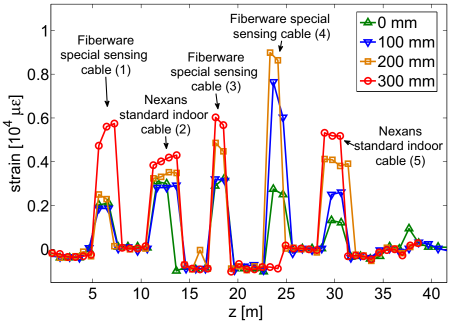

Figure 7.19: Results from the distributed strain measurement on the net test bench at STFI. See figure 7.17 for the fiber configuration with the corresponding enumeration.

The sensor system itself showed a reliable performance; the relation of the longitudinal strain experienced by the fibers in the two different cable solutions to the real elongation of the textile corresponds to the results from the polystyrene model (mainly, the effect of slipping of the fiber inside the coating leading to a smaller strain value over a longer spatial extent for the NEXANS cable, as can be clearly seen in figure 7.19).

The indenter was elevated until the epoxy fixation (being weaker than the optical cables) failed to withstand the applied force. Thus, no conclusion about the maximum measurable strain and the break point of the sensors is permitted.

The most relevant conclusion to be drawn from the measurements on the net test bench is the feasibility of the concept to integrate one-dimensional sensors (optical fibers) into two-dimensional structures (geotextiles) in order to achieve higher sensitivity to displacement of arbitrary orientation, as it already has been discussed in section 7.2.1. In figure 7.19, it becomes visible that even the fiber sections that were not placed directly above the indenter head, but rather remotely from it (namely sections (1), (2) and (3)) were able to reliably detect the mechanical stress that the textile experienced. Even deformation of the textile in an orthogonal orientation to the sensing fiber leads to deformation of the cable which applies detectable longitudinal strain to the optical fiber. From the traces in figure 7.19, with the maximum of measured strain in section (4) (which is located right above the indenter's center) and less strain detected in the adjacent sections, the location of maximum activity can be estimated from the traces.

CHAPTER 8

Synopsis

It is time to compare: What had been the perspectives for the assignment of Brillouin sensing to the monitoring of river embankments three years ago – and what are they now? The feasibility of the Brillouin frequency domain analysis had been proven years prior to the start of this work [34], and so had the idea to embed optical fibers into geotextiles [10]; distributed Brillouin sensing has been an established technique in structural health monitoring for several years [14]; even in flood protection, the technique has increased in popularity [71].

Summary and conclusions

Daring a general overview, two major steps that have been tackled within this work can be pointed out: First, the great potential of the Brillouin frequency domain analysis with its number of advantages over pulse-reflectometry systems (which have been explicitly pointed out on page 42) had been prevented from being unrolled in praxis due to its complexity that required sophisticated laboratory instruments so far; also, the time domain analysis systems had made a large step ahead in terms of sensing accuracy and spatial resolution. Second, the task of monitoring arbitrary events of soil displacement over the length of several kilometers required a new concept for integration of real distributed sensors (not FBG sensors, as it had been presented previously [10]) into the soil.

Into these two general bins, the major achievements of the work presented in this thesis can be categorized: A deeper understanding of **the physical background of stimulated Brillouin scattering under the conditions of a frequency domain analysis system** helped to advance the system setup in terms of measurement accuracy and efficiency: Signal detection using one photoreceiver, polarization control, accurate and fast control of the laser offset and an analysis of system linearity and the impact of system-inherent inaccuracies on the measurement trace add up to a largely matured measurement setup that has even been transported to remote sites for complex measurement procedures (chapters 2, 3 and 4).

The implementation of a demonstrator setup for an **all-digital acquisition of the complex transfer function** of SBS inside an optical fiber finally opens up the way for assignment of the BOFDA system to rel-life tasks. This proof of a cost-efficient replacement for the bulky network analyzer underlines the potential of the idea to measure the pulse response by measuring all frequency components of the optical pulse one after another (chapter 5).

The proposal of a **signal correction method to restore the Brillouin gain spectra** from their artifacts at high spatial resolutions closes up to the state-of-the-art of BOTDA systems: The limitation of the spectral widths of the optical signals to the Brillouin linewidth, which had the limitation of the spatial resolution to about 1 m as a consequence, can be overcome by the proposed technique [75] (chapter 6).

Finally, the problem of **embedding the optical fibers into the soil** was handled by the concept of sensor-equipped geotextiles [76]. With a synergy of experts in technical textiles, geomechanics, structural health monitoring and fiber optic sensing, a robust method for integrating coated optical fibers into geotextiles was developed; furthermore, the requirements on a sensing cable for dike monitoring were formulated and a special cabling technology was developed [77]. With this powerful new tool at hand, the interaction between geotechnical activities and the sensing technology could be investigated component by component, and finally, valuable real-life experiences regarding the application of fiber optic sensors on construction sites in the field were made (chapter 7).

The benchmarks at which the performance of the overall system have to be judged had been presented at the beginning of this thesis: Spatial resolution, resolution of the measurands, measurement length and time for data acquisition. The first three parameters have been directly handled by the above issues of achievements [78]; with a recorded strain profile of an accuracy of a few ten $\mu\varepsilon$ over a range of 5 km at a spatial resolution of 2 m, the requirements on a dike monitoring system stated by the experts of flood protection are met [79]. Moreover, the latter two of the parameters could be improved beyond these marks (measurements up to 10 km have been performed; a spatial resolution of 0.8 m has been shown).

Regarding the measuring speed, the time of 30 minutes required for the above measurement is still long compared to the BOTDA systems that represent the state-of-the-art [12]. On the other hand, the demonstrator setup for the digital acquisition of the transfer function opens up a whole new field with adjusting screws to speed up measurement. Once the system is integrated into a single embedded hardware which performs both signal generation and processing, the BOFDA system can unfold its potential for competitively fast measurements. The proof of feasibility for this approach has been given within this work.

Outlook

Research on the Brillouin frequency domain analysis for structural health monitoring has arrived at a state which displays its potential and its benefits, but certainly implies to be pursued further into the direction of efficient implementation and practical application. The following issues are the next to be approached if the work is to be carried on towards the protoype of a mature monitoring system:

The decision whether **the two-laser configuration** that has been used throughout this work, or **the one-laser configuration** briefly presented in section 4.1.2 should be used for an efficient implementation of the overall system can not be taken easily. If the two-laser configuration should be used, the Nd:YAG sources would have to be replaced by DFB lasers; their tuning to a fixed frequency offset brings up further issues to be investigated (such as the dependency between the laser diode injection current and the optical frequency), as well as the need for an efficient circuitry as a control loop (which, in effect, can be considered as an electro-optical PLL) to replace the spectrum analyzer. In the one-laser setup, considerations about combining the two amplitude modulations – the RF modulation for creation of the sidebands and the modulation for acquisition of the transfer function – should be made.

For the issue of **polarization handling**, two approaches have been proposed: Either scrambling the polarization while measuring the complex transfer function, or measuring each point for f_m and Δf at a defined number of different states of polarization for averaging. With the focus on implementation efficiency and robustness, the scrambling variant looks like the more promising path at the current state of the investigations; still, the control of a piezo-fiber-optic polarization scrambler deserves a re-design for the special tasks within the BOFDA system. Commercially available devices employ a random signal on all piezo channels that introduces broad-band noise on the received signal and degrades the narrow-band measurement of amplitude and phase. With a customized control that excites the piezo actuator only at scrambling frequencies that do not overlap with the sweep values of f_m, this problem could be overcome.

Integrating the digital acquisition of the transfer function into a single embedded hardware such as an FPGA, the robustness and measurement speed could be designed to match the requirements of real-life applications. While the current demonstrator setup is designed to perform frequency sweeps from 20 kHz to 20 MHz, the next implementation should cover all the range from 5 kHz to 100 MHz (fiber length of 10 km at a spatial resolution of 1 m). All high-speed digital and analog electronics would increase in complexity at such an expansion, but there is no systematical problem that would inhibit the step.

The integration of optical fibers into the soil by producing sensor-equipped geotextiles has been proven to be feasible. Now it has to be verified under the tough conditions of a real soil environment: Field tests have to be performed that reveal the sensors' behavior if really several kilometers are measured over years and years; the cable has to prove its robustness in moisture and chemically aggressive environment, not to forget about the rodents (squirrels, martens, moles and alike) that enjoy chewing on attractively-colored cables once in a while.

With all the experiences on monitoring of river embankments, the expansion of the field of applications to other large structures is a logical step. The list of monitoring objects that would benefit from the special capabilities of Brillouin sensing is long: Bridges, tunnels, dams, railway embankments, hangs, slopes, streets, landfills, power lines, pipelines… Even if for each of these structures all the cabling and integration technology would have to be reconsidered, the experiences made are a valuable starting point for the development of customized solutions in any field of structural health monitoring.

Distributed Brillouin sensing for structural health monitoring is a technology with a market that has just begun to open up. Fundamental research is still the main issue, if entering this market should be aimed at; with any new development in the fields of fiber optics, lasers and high-speed electronics, the Brillouin frequency domain analysis will get its chance to make the next step from infancy to maturity. Once the tasks on the way to the prototype are accomplished, the experiences gathered in this work will get further opportunities to contribute to such technological advancements.

APPENDIX A

Tables

A.1 Measurement parameters

Table A.1 summarizes the parameters of the measurements performed with the BOFDA system that have been described throughout the text. The parameters shown are the minimum modulation frequency f_{min}, the maximum modulation frequency f_{max}, the spatial resolution δz, the measurement length z_{max}, the total range of laser detuning Δf_B, the step width of laser detuning df_B, the frequency of the polarization scrambler f_{scr} (in which (*) means, no scrambling was performed) and the page where graphs and interpretations of the results are given.

	f_{min} [MHz]	f_{max} [MHz]	δz [m]	z_{max} [m]	Δf_B [MHz]	df_B [MHz]	f_{scr} [kHz]	
Strain profile	0.1	30	3.4	1021	450	2.5	0.3	p. 61
Test dike	0.1	25	4	2550	220	2	(*)	p. 118
Polystyrene model	0.4	50	2	255	820	2	0.3	p. 121
Net test bench	0.4	50	2	255	1000	4	0.3	p. 123
Digital setup	0.2	20	5	510	450	2	(*)	p. 76

Table A.1: Parameters of the BOFDA measurements described thorughout the text

A.2 List of acronyms, abbrevations and symbols

Table A.2: abbreviations and symbols used throughout the text

acronym	*meaning*
ADC	analog-to-digital converter
BOFDA	Brillouin frequency domain analysis
BOTDA	Brillouin time domain analysis
CW	continuous wave light
DAC	digital-to-analog converter
dBc	dB from carrier
dBfs	dB full scale
DDS	direct data synthesis
DFT	discrete Fourier transform
EOM	electro-optical modulator
FC/PC	fiber connector, physical contact
FC/APC	fiber connector, angled physical contact
FFT	fast Fourier transform
FIFO	first in, first out: data buffer design (queuing behavior)
FPGA	Field Programmable Gate Array
FUT	fiber under test
FWHM	full width at half maximum
IFFT	inverse fast Fourier transform
PCB	printed circuit board
PMD	polarization mode dispersion
POF	polymer optical fiber
PSF	point-spread function (term taken from image processing)
SBS	stimulated Brillouin scattering
SOP	state of polarization
TEC	thermo-electric cooler (peltier element)
THD	total harmonic distortion
VNA	vector network analyzer
A, A_p, A_s	AM DC offset (general, pump and stokes signal)
A_{eff}	effective core area of an optical fiber
c_0	vacuum speed of light
d	degradation function in the signal correction procedure
df	frequency increment in BOFDA measurements
E_p	amplitude of the electrical field of the pump wave
E_s	amplitude of the electrical field of the Stokes wave
f_B	Brillouin frequency shift

f_m	modulation frequency for BOFDA measurements
f_{min}	lowest sweep value for modulation frequency f_m
f_{max}	highest sweep value for modulation frequency f_m
f_s	sampling rate of a digital system for signal processing
$g_B(\Delta f)$	Brillouin gain spectrum
g'	degraded Brillouin gain spectrum
g''	reconstructed Brillouin gain spectrum
$h(t)$	pulse response of a linear, time-invariant system
$H(j\omega)$	a system's complex transfer function
$\vec{k}$	wave vector of the acoustic wave
$\vec{k}_p$	wave vector of the pump wave
$\vec{k}_s$	wave vector of the Stokes wave
L	fiber length
L_{eff}	effective fiber length
L_B	polarization beat length
m	modulation index for AM
m_p	modulation index for AM: pump wave
m_s	modulation index for AM: Stokes wave
n	refractive index (for dispersive media: refractive group index)
N	total number of sampling points of a discrete time domain sequence
$\vec{P}$, $\vec{P}_L$, $\vec{P}_{NL}$	electrical polarization (total, linear, nonlinear)
P_p	optical power of the pump wave
P_s	optical power of the Stokes wave
$\text{Re}(z)$, $\text{Im}(z)$	real and imaginary parts of a complex number z
T	temperature
T	temporal periodicity of the result of a discrete IFFT (chapter 3)
U_T	control voltage at the Nd:YAG lasers' temperature elements
U_P	control voltage at the Nd:YAG lasers' piezo actuators
v	propagation speed of the beat pattern
v_a	speed of sound (acoustic velocity)
$\vec{V}$	velocity of a mass element
W	core radius of an optical fiber
z	longitudinal dimension of an optical fiber
z_{max}	maximum measurement length
α	optical loss coefficient
β	modulus of elasticity
Γ	damping rate of the acoustic wave (material constant)
γ^e	coefficient of electrostriction (material constant)
Δf	frequency offset between pump and Stokes wave
δf_B	linewidth (full width at half maximum) of the Brillouin gain spectra
δz	spatial resolution of the distributed measurement
δ	Dirac delta function

ε, ε_0, ε_r	Chapter 2: total, vacuum, relative permittivity
ε	longitudinal strain of an optical fiber
η	noise / defective measurement impact
λ	periodic length of the beat pattern; acoustic wavelength
λ_p	optical wavelength of the pump wave (and approx. the Stokes wave)
$\mu\varepsilon$	microstrain (quantity of longitudinal strain: 10^{-4} %)
ρ_0	average value of the scattering medium's density
ρ	amplitude of the density fluctuations (acoustic wave amplitude)
τ_B	phonon lifetime ($1/\Gamma_B$)
φ	phase angle
Φ_ξ	intensities of the spectral components of the beat pattern
ω_p, ω_s, ω_a	angular frequency of the pump wave, Stokes wave, acoustic wave
ω_0	angular frequency difference between pump and Stokes wave
∇	Nabla operator

A.3 List of instruments and laboratory components

The following table gives a summary of the laboratory equipment that was employed throughout the laboratory and field tests that have been described in this thesis. It contains the most important bench-top and portable instruments as well as some smaller electrical, optical and mechanical components.

Table A.3: Instruments and components

description	*manufacturer and designation*	*referenced in sections*
spectrum analyzer	ROHDE & SCHWARZ FSP	2.2.1
temperature chamber	VÖTSCH VTL 4003	2.2.2
vector network analyzer	AGILENT 4395A	4.2
photon counting OTDR	SUNRISE TECHNOLOGIES ν-OTDR	7.3.1
OTDR	EXFO FTB-200B	7.3.1
fusion splicer	ERICSSON	7.3.1
Nd:YAG lasers	LIGHTWAVE ELECTRONICS Series 125	2.1.4, 4.1.1
polarization controller	GENERAL PHOTONICS	4.3
polarization scrambler	GENERAL PHOTONICS	4.3
optical power meter	EXFO FPM-600	2.2.1
electro-optical modulator	AVANEX PowerBit SD10	4.2
oscilloscope	TEKTRONIX TDS-220	5.1.2
photodetector (1 GHz)	NEW FOCUS Model 1611	4.2
photodetector (25 GHz)	NEW FOCUS Model 1414	2.2.2
ADC	ANALOG DEVICES AD 9640	5.2.2
DDS	ANALOG DEVICES AD 9850	5.2.1

APPENDIX B

Addendum to preceeding chapters

B.1 The excitation of the acoustic wave

In equation (2.16), a harmonic ansatz for the beat pattern was formulated, twice spatially derived to enter the equation for the excitation of the acoustic wave (2.12). The complete analysis starts with the expansion of the quadrature term:

$$\left(\underbrace{E_p e^{j(\omega_p t-k_p z)}}_{a}+\underbrace{E_p^* e^{-j(\omega_p t-k_p z)}}_{b}+\underbrace{E_s e^{j(\omega_s t+k_s z)}}_{c}+\underbrace{E_s^* e^{-j(\omega_s t+k_s z)}}_{d}\right)^2$$

is expanded according to

$$(a+b+c+d)^2 = a^2+b^2+c^2+d^2+2ab+2ac+2ad+2bc+2bd+2cd$$

The expansion is performed in detail for the case of two unmodulated light waves of a single frequency, as required from section 2.1.2. In section 6.1.2, the analysis was done in complete analogy, but with considerably more summands entering the quadrature expression, to describe the beat pattern for modulated pump and Stokes light. The following considerations regarding the relevance of the frequency components for the envelope of the beat pattern can be directly transferred section 6.1.2, where the expression (6.5) for Φ_ξ is derived from equation (6.3).

The ten summands of the expansion are the following:

$$\begin{aligned}
a^2 &= E_p^2 e^{2j(\omega_p t - k_p z)} \\
b^2 &= E_p^{*2} e^{-2j(\omega_p t - k_p z)} \\
c^2 &= E_s^2 e^{2j(\omega_s t + k_s z)} \\
d^2 &= E_s^{*2} e^{-2j(\omega_s t + k_s z)} \\
ab &= E_p E_p^* = |E_p|^2 \\
ac &= E_p E_s e^{j((\omega_p + \omega_s)t - (k_p - k_s)z)} \\
ad &= E_p^* E_s e^{j((\omega_p - \omega_s)t - (k_p + k_s)z)} \\
bc &= E_p E_s^* e^{-j((\omega_p - \omega_s)t - (k_p + k_s)z)} \\
bd &= E_p^* E_s^* e^{-j((\omega_p + \omega_s)t - (k_p - k_s)z)} \\
cd &= E_s E_s^* = |E_s|^2
\end{aligned}$$

These are the frequency components of the beat pattern for the case of two counter-propagating single-frequency light waves. In accordance to equations (2.1) and (2.3), only the terms *ad* and *bc* contribute to the envelope of the beat pattern, because

$$\Delta f = \frac{\omega_p - \omega_s}{2\pi} = \frac{\omega_0}{2\pi}$$

can be tuned to fulfill the resonant condition $\Delta f = f_B$. Then, the frequency and velocity of the acoustic wave match the frequency and velocity of the beat pattern ($\omega_a = \omega_0$). All remaining summands are neglected: The summands a^2, b^2, c^2 and d^2 as well as *ac* and *bd* are frequency components well above the optical band and do not affect the beat pattern's envelope. The summands *ab* and *cd* are DC terms with no oscillating phases and do not describe propagating waves.

The envelope of the beat pattern is derived in its z dimension to enter (2.12), by introducing the two remaining summands of the expansion into equation (2.16):

$$\begin{aligned}
\nabla^2 \left(\vec{E}^2\right) &= \frac{\partial^2}{\partial z^2}\left(\frac{1}{2}\left(E_p^* E_s e^{j(\omega_0 t - k_0 z)} + E_p E_s^* e^{-j(\omega_0 t - k_0 z)}\right)\right) \\
&= \frac{1}{2}\frac{\partial}{\partial z}\left(\frac{\partial E_p}{\partial z} E_s^* e^{j(\omega_0 t - k_0 z)} + E_p \frac{\partial E_s^*}{\partial z} e^{j(\omega_0 t - k_0 z)} - jk_0 E_p E_s^* e^{j(\omega_0 t - k_0 z)}\right. \\
&\quad \left. + \frac{\partial E_p^*}{\partial z} E_s e^{-j(\omega_0 t - k_0 z)} + E_p^* \frac{\partial E_s}{\partial z} e^{-j(\omega_0 t - k_0 z)} + jk_0 E_p^* E_s e^{-j(\omega_0 t - k_0 z)}\right)
\end{aligned}$$

$$
\begin{aligned}
&= \frac{1}{2}\left(\frac{\partial^2 E_p}{\partial z^2}E_s^* e^{j(\omega_0 t - k_0 z)} + 2\frac{\partial E_p}{\partial z}\frac{\partial E_s^*}{\partial z}e^{j(\omega_0 t - k_0 z)} - 2jk_0\frac{\partial E_p}{\partial z}E_s^* e^{j(\omega_0 t - k_0 z)}\right.\\
&+ E_p\frac{\partial^2 E_s^*}{\partial z^2}e^{j(\omega_0 t - k_0 z)} - 2jk_0 E_p\frac{\partial E_s^*}{\partial z}e^{j(\omega_0 t - k_0 z)} - k_0^2 E_p E_s^* e^{j(\omega_0 t - k_0 z)}\\
&+ \frac{\partial^2 E_p^*}{\partial z^2}E_s e^{-j(\omega_0 t - k_0 z)} + 2\frac{\partial E_p^*}{\partial z}\frac{\partial E_s}{\partial z}e^{-j(\omega_0 t - k_0 z)} + 2jk_0\frac{\partial E_p^*}{\partial z}E_s e^{-j(\omega_0 t - k_0 z)}\\
&\left.+ E_p^*\frac{\partial^2 E_s}{\partial z^2}e^{-j(\omega_0 t - k_0 z)} + 2jk_0 E_p^*\frac{\partial E_s}{\partial z}e^{-j(\omega_0 t - k_0 z)} - k_0^2 E_p^* E_s e^{-j(\omega_0 t - k_0 z)}\right)
\end{aligned}
$$

From these summands, all remaining derivatives can be neglected due to the assumption of slowly varying amplitudes that was made in section 2.1.2. Consequently, only the term

$$-k_0^2 E_p E_s^* e^{j(\omega_0 t - k_0 z)}$$

and its complex conjugate enter the excitation of the acoustic wave in equation (2.12).

B.2 Time-domain behavior of the DDS board

In order to illustrate the performance on the digital data synthesis for generation of the modulation frequency f_m, the implementation of which has been described in section 5.2.1, figure B.1 shows the reaction of the DDS board to the request for a change in output frequency from the controlling computer. It can be seen that the change in output frequency is performed within 3 ms after the start of serial communication that transmits the request.

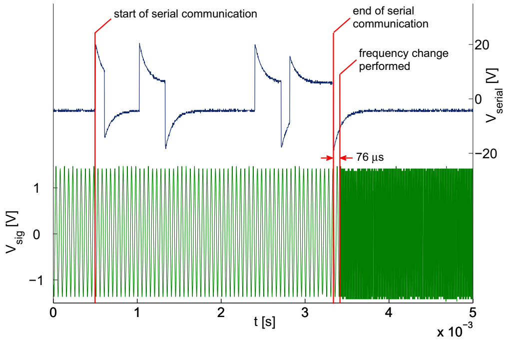

Figure B.1: Response of the DDS board to a change in output frequency requested by an external computer.

Bibliography

[1] J. Zschau and A. N. Küppers, *Early Warning Systems for Natural Disaster Reduction.* Springer, 2003.

[2] A. Kortenhaus, “Breaching of flood defences and resulting failure probability,” IOER, 2007.

[3] A. Möllmann, P. A. Vermeer, and B. Westrich, “Reliability analysis of river embankments using analytical methods and finite elements,” ICLR, 2008.

[4] A. Bieberstein, R. Zesch, T. Riegger, U. Saucke, A. Scheuermann, and T. Triantafyllidis, “Hochwasserschutzdeiche – aktuelle Entwicklungen zur Verbesserung der Hochwassersicherheit,” *Bautechnik*, vol. 84, pp. 829 – 837, 2007.

[5] M. Schallert, D. Hofmann, W. R. Habel, and J. Stahlmann, “Structure-integrated fiber-optic sensors for reliable static and dynamic analysis of concrete foundation piles,” vol. 6530, p. 65300D, SPIE, 2007.

[6] K. Krebber, W. R. Habel, T. Gutmann, and C. Schram, “Fiber Bragg grating sensors for monitoring of wind turbine blades,” vol. 5855, pp. 1036–1039, SPIE, 2005.

[7] U. Glombitza and H. Hoff, “Fibre optic radar system for fire detection in cable trays,” AUBE, 2004.

[8] P. Lenke, S. Liehr, K. Krebber, F. Weigand, and E. Thiele, “Distributed strain measurement with polymer optical fiber integrated in technical textiles using the optical time domain reflectometry technique,” pp. 21–24, POF Conference, 2007.

[9] S. Liehr, P. Lenke, K. Krebber, M. Seeger, E. Thiele, H. Metschies, B. Gebreselassie, J. C. Munich, and L. Stempniewski, “Distributed strain measurement

with polymer optical fibers integrated into multifunctional geotextiles," vol. 7003, p. 700302, SPIE, 2008.

[10] M. R. Voet, A. Nancey, and J. Vlekken, "Geodetect: a new step for the use of fibre Bragg grating technology in soil engineering," vol. 5855, pp. 214–217, SPIE, 2005.

[11] M. Aufleger, *Verteilte faseroptische Temperaturmessungen im Wasserbau.* Berichte des Lehrstuhls und der Versuchsanstalt für Wasserbau und Wasserwirtschaft der TU München 89 (Habilitation), 2000.

[12] Omnisens SA, *DITEST STA-R Series: Fiber Optic Distributed Temperature & Strain Monitoring System*, 2008.

[13] K. K. Yoshiaki Yamauchi, Artur Guzik and L. Che-Hsien, "A study on the stability, reliability, and accuracy of Neubrescope-based pipe thinning detection system," November 2007.

[14] D. Inaudi and B. Glisic, "Integration of distributed strain and temperature sensors in composite coiled tubing," vol. 6167, pp. 616–717, SPIE, 2006.

[15] F. Bastianini, M. Cargnelutti, A. D. Tommaso, and M. Toffanin, "Distributed Brillouin fiber optic strain monitoring applications in advanced composite materials," vol. 5057, pp. 478–485, SPIE, 2003.

[16] J. Nakamura, M. Sakanishi, A. Kitazawa, K. Kumagai, K. Fujihashi, and T. Ogasawara, "Deformation measurement technology of geomembrane at controlled landfills using optical fiber sensors," Millpress Science Publishers, 2006.

[17] D. Inaudi and B. Glisic, "Fiber optic sensing for innovative oil and gas production and transport systems," in *Optical Fiber Sensors*, p. FB3, Optical Society of America, 2006.

[18] S. Johannson and D. Watley, "Distributed sensing of seepage and movements using optical fibres-Results from some embankment dams in Sweden," *International Water Power and Dam Construction*, 2005.

[19] D. Moser, M. Aufleger, R. Hoepffner, V. Neisch, M. Soares, and J. Filho, "Temperature and strain measurements in RCC dams using fibre optic instrumentation," February 2007.

[20] L. Brillouin, "Diffusion de la lumière et des rayons X par un corps transparent homogène. influence de l'agitation thermique," *Annales de Physique*, vol. 17, no. 88, 1922.

[21] W. Kaiser and M. Maier, *Laser Handbook.* North-Holland publications, 1973.

[22] G. P. Agrawal, *Nonlinear Fiber Optics.* San Diego: Academic Press, 2001 (third edition).

[23] Guang S. He and Song H. Liu, *Physics of Nonlinear Optics.* World Scientific publishing, 1999.

[24] V. Lecoeuche, S. Randoux, B. Ségard, and J. Zemmouri, "Dynamics of a Brillouin fiber ring laser: Off-resonant case," *Phys. Rev. A*, vol. 53, pp. 2822–2828, Apr 1996.

[25] E. Voges and K. Petermann, *Optische Kommunikationstechnik.* Berlin: Springer, 2002.

[26] Y. Guo, C. K. Kao, E. H. Li, and K. S. Chiang, *Nonlinear Photonics.* Springer and The Chinese University Press, 2002.

[27] C. C. Chow and A. Bers, "Chaotic stimulated Brillouin scattering in a finite-length medium," *Phys. Rev. A*, vol. 47, pp. 5144–5150, Jun 1993.

[28] M. van Deventer and A. Boot, "Polarization properties of stimulated Brillouin scattering in single-mode fibers," *Lightwave Technology, Journal of*, vol. 12, no. 4, pp. 585–590, Apr 1994.

[29] M. Van Deventer, "Preservation of polarisation orthogonality of counterpropagating waves through dichroic birefringent optical media: proof and application," *Electronics Letters*, vol. 27, pp. 1538–1540, Aug. 1991.

[30] T. Gogolla and K. Krebber, "Distributed beat length measurement in single-mode optical fibers using stimulated Brillouin-scattering and frequency-domain analysis," *Journal of Lightwave Technology*, vol. 18, pp. 320–328, Mar 2000.

[31] Corning Incorporated, *Corning SMF-28e Optical Fiber Product Information*, 2004.

[32] P. Lenke and N. Nöther, "Stimulated Brillouin scattering in graded index multimode optical fiber by excitation of the fundamental mode only," vol. 6582, p. 658213, SPIE, 2007.

[33] Y. T. Cho, G. P. Lees, G. Hilton, X. Shu, K. Sudgen, A. Strong, A. Hartog, and T. P. Newson, "100km distributed fiber optic sensor based on the coherent detection of Brillouin backscatter, with a spatial resolution of 10 m, enhanced using two stages of remotely pumped erbium-doped fiber combined with raman amplification," in *Optical Fiber Sensors*, p. ThC4, Optical Society of America, 2006.

[34] K. Krebber, *Ortsauflösende Lichtleitfaser-Sensorik für die Temperatur und Dehnung unter Nutzung der stimulierten Brillouin-Streuung basierend auf der Frequenzbereichsanalyse.* Hochschulschrift Ruhr-Universität Bochum (Dissertation), 2001.

[35] Lightwave Electronics, *Lightwave Electronics 125/126 Series: Fiber-coupled Nd:YAG lasers, Manual: D-0864 REV. B 6/22/02*, 2005.

[36] M. Nikles, L. Thevenaz, and P. Robert, “Brillouin gain spectrum characterization in single-mode optical fibers,” *Lightwave Technology, Journal of*, vol. 15, no. 10, pp. 1842–1851, Oct 1997.

[37] T. Kurashima, T. Horiguchi, and M. Tateda, “Thermal effects of Brillouin gain spectra in single-mode fibers,” *IEEE Photonics Technology Letters*, vol. 2, no. 10, pp. 718–720, 1990.

[38] T. Kurashima, T. Horiguchi, and M. Tateda, “Tensile strain dependence of Brillouin frequency shift in silica optical fibers,” *IEEE Photonics Technology Letters*, vol. 1, no. 5, pp. 107–108, 1989.

[39] X. Bao, D. J. Webb, and D. A. Jackson, “Combined distributed temperature and strain sensor based on Brillouin loss in an optical fiber,” *Opt. Lett.*, vol. 19, no. 2, p. 141, 1994.

[40] M. Nikles, L. Thevenaz, and P. A. Robert, “Simple distributed fiber sensor based on Brillouin gain spectrum analysis,” *Opt. Lett.*, vol. 21, no. 10, p. 758, 1996.

[41] T. Parker, M. Farhadiroushan, V. Handerek, and A. Roger, “A fully distributed simultaneous strain and temperature sensor using spontaneous Brillouin backscatter,” *Photonics Technology Letters, IEEE*, vol. 9, pp. 979–981, July 1997.

[42] P. Lenke, S. Liehr, and K. Krebber, “Improvements of the distributed strain sensor based on optical time domain reflectometry measurement in polymer optical fibers,” 2008.

[43] R. Stolle, H. Heuermann, and B. Schiek, “Novel algorithms for FMCW range finding with microwaves,” pp. 129–132, May 1995.

[44] H. Ghafoori-Shiraz and T. Okoshi, “Fault location in optical fibers using optical frequency domain reflectometry,” *Lightwave Technology, Journal of*, vol. 4, pp. 316–322, Mar 1986.

[45] B. Schiek, *Grundlagen der Hochfrequenz-Messtechnik*. Berlin: Springer, 1999.

[46] S. Liehr, N. Nöther, and K. Krebber, “Incoherent optical frequency domain reflectometry and distributed strain detection in polymer optical fibers,” *Measurement Science and Technology*, vol. 21, no. 1, p. 017001 (4pp), 2010.

[47] D. Garus, T. Gogolla, K. Krebber, and F. Schliep, “Brillouin optical-fiber frequency-domain analysis for distributed temperature and strain measurements,” *Lightwave Technology, Journal of*, vol. 15, no. 4, pp. 654–662, Apr 1997.

[48] T. Gogolla, *Theoretische Untersuchung der Brillouin-Wechselwirkung in Lichtleitfasern zur kontinuierlich verteilten Teperatur- und Dehnungsmessung auf Basis der Frequenzbereichsanalyse.* Hochschulschrift Ruhr-Universität Bochum (Dissertation), 2000.

[49] R. Bernini, L. Crocco, A. Minardo, F. Soldovieri, and L. Zeni, "All frequency domain distributed fiber-optic Brillouin sensing," *Sensors Journal, IEEE*, vol. 3, no. 1, pp. 36–43, Feb. 2003.

[50] A. Zornoza, D. Olier, M. Sagues, and A. Loayssa, "Distortion-free Brillouin distributed sensor using RF shaping of pump pulses," vol. 7503, p. 75036D, SPIE, 2009.

[51] L. Thevenaz and J.-C. Beugnot, "General analytical model for distributed Brillouin sensors with sub-meter spatial resolution," vol. 7503, p. 75036A, SPIE, 2009.

[52] J. Kaiser, "Nonrecursive digital filter design using the I0- sinh window function," pp. 20–23, April 1974.

[53] B. Schlemmer and A. Winter, "Real part determination OFDR with digital spatial filtering," *Photonics Technology Letters, IEEE*, vol. 6, pp. 1011–1013, Aug 1994.

[54] R. Bernini, A. Minardo, and L. Zeni, "An accurate high-resolution technique for distributed sensing based on frequency-domain Brillouin scattering," *Photonics Technology Letters, IEEE*, vol. 18, no. 1, pp. 280–282, Jan. 1, 2006.

[55] S. Diaz, S. Mafang, M. Lopez-Amo, and L. Thevenaz, "A high-performance optical time-domain Brillouin distributed fiber sensor," *Sensors Journal, IEEE*, vol. 8, pp. 1268–1272, July 2008.

[56] M. Facchini, L. Thevenaz, J. Troger, and P. Robert, "2-laser injection-locking configuration for Brillouin fibre sensors," pp. 313–316 vol.1, 2002.

[57] S. Jetschke, U. Roepke, and E. Geinitz, "Averaging of polarization modulations in a distributed Brillouin fiber sensor system," vol. 16, pp. 528–531, OSA, 1997.

[58] Analog Devices, *AD9640 is a dual 14-bit, 125 MSPS analog-to-digital converter*, 2009.

[59] R. G. Lyons, *Understanding Digital Signal Processing.* Upper Saddle River: Prentice Hall PTR, 2004 (second edition).

[60] A. W. Brown, M. D. DeMerchant, X. Bao, and T. W. Bremner, "Spatial resolution enhancement of a Brillouin-distributed sensor using a novel signal processing method," *Lightwave Technology, Journal of*, vol. 17, pp. 1179–1183, July 1999.

[61] J. Smith, A. Brown, M. DeMerchant, and X. Bao, "Pulse width dependance of the Brillouin loss spectrum," *Optics Communications*, vol. 168, no. 5-6, pp. 393 – 398, 1999.

[62] A. Fellay, L. Thévenaz, M. Facchini, M. Niklès, and P. Robert, "Distributed sensing using stimulated Brillouin scattering : Towards ultimate resolution.," in *Optical Fiber Sensors*, p. OWD3, Optical Society of America, 1997.

[63] V. Lecoeuche, D. J. Webb, C. N. Pannell, and D. A. Jackson, "Transient response in high-resolution Brillouin-based distributed sensing using probe pulses shorter than the acoustic relaxation time," *Opt. Lett.*, vol. 25, no. 3, pp. 156–158, 2000.

[64] R. Bernini, A. Minardo, and L. Zeni, "Frequency-domain analysis of stimulated Brillouin scattering in single-mode optical fibers," *Fibres and Optical Passive Components, 2005. Proceedings of 2005 IEEE/LEOS Workshop on*, pp. 382–388, June 2005.

[65] F. G. Stremler, *Introduction to Communication Systems.* Addison-Wesley, 1982.

[66] X. Bao, A. Brown, M. DeMerchant, and J. Smith, "Characterization of the Brillouin-loss spectrum of single-mode fibers by use of very short (<10-ns) pulses," *Opt. Lett.*, vol. 24, no. 8, pp. 510–512, 1999.

[67] R. C. Gonzalez, R. E. Woods, and S. L. Eddins, *Digital Image Processing Using MATLAB.* Prentice Hall, 2003.

[68] W. H. Richardson, "Bayesian-based iterative method of image restoration," *J. Opt. Soc. Am.*, vol. 62, no. 1, pp. 55–59, 1972.

[69] L. B. Lucy, "An iterative technique for the rectification of observed distributions," *Astronomical Journal*, vol. 79, p. 745, 1974.

[70] L. Thevenaz and S. F. Mafang, "Distributed fiber sensing using Brillouin echoes," vol. 7004, p. 70043N, SPIE, 2008.

[71] R. Hoepffner, *Distributed fiber optic strain sensing in hydraulic concrete and earth structures.* Berichte des Lehrstuhls und der Versuchsanstalt für Wasserbau und Wasserwirtschaft (Dissertation), 2008.

[72] G. Heerten, "Geotextiles in coastal engineering," *Materials and Structures*, vol. 14, no. 4, pp. 273–281, Juli 1981.

[73] E. Thiele, H. Erth, R. Helbig, K. Werth, R. Glötzl, J. Schneider-Glötzl, N. Nöther, A. Wosniok, K. Krebber, T. Schlurmann, and F. Saathoff, "Sensitive Textilstrukturen zur Deichüberwachung," pp. 1–5, STFI, 2008.

[74] G. Kuka, M. Steinbach, A. Knorr, and N. Nöther, "Optisches Sensorkabel," pp. 35–38, IWKM, 2008.

[75] N. Nöther, P. Lenke, and K. Krebber, "A novel signal restoration method in the frequency domain to enhance spatial resolution in distributed Brillouin sensing," vol. 7503, p. 75032F, SPIE, 2009.

[76] N. Nöther, A. Wosniok, K. Krebber, and E. Thiele, “Dike monitoring using fiber sensor-based geosynthetics,” ECCOMAS, Jul 2007.

[77] N. Nöther, A. Wosniok, K. Krebber, and E. Thiele, “A distributed fiber-optic sensing system for monitoring of large geotechnical structures,” ISHMII, 2009.

[78] N. Nöther, A. Wosniok, and K. Krebber, “A distributed fiber optic sensor system for dike monitoring using Brillouin frequency domain analysis,” vol. 7003, p. 700303, SPIE, 2008.

[79] N. Nöther, A. Wosniok, K. Krebber, and E. Thiele, “A distributed fiber optic sensor system for dike monitoring using Brillouin optical frequency domain analysis,” vol. 6933, p. 69330T, SPIE, 2008.